Spatial and temporal correlations in cold Rydberg gases

Dissertation

der Mathematisch-Naturwissenschaftlichen Fakultät
der Eberhard Karls Universität Tübingen
zur Erlangung des Grades eines
Doktors der Naturwissenschaften
(Dr. rer. nat.)

vorgelegt von
Markus Stecker
aus Singen (Hohentwiel)

Tübingen
2018

Gedruckt mit Genehmigung der Mathematisch-Naturwissenschaftlichen Fakultät der Eberhard Karls Universität Tübingen.

Tag der mündlichen Qualifikation:	16.05.2018
Dekan:	Prof. Dr. Wolfgang Rosenstiel
1. Berichterstatter:	Prof. Dr. József Fortágh
2. Berichterstatter:	Prof. Dr. Claus Zimmermann

Contents

Abstract

Rydberg atoms, i.e. atoms with one or more highly excited electrons, show exaggerated properties compared to ground state atoms. For example, their energy levels are very sensitive to external electric fields (Stark effect) and they exhibit strong interatomic interactions, which can lead to a suppression of excitation known as the Rydberg blockade. The latter property makes Rydberg atoms promising candidates for quantum simulation and quantum computing. This work describes the direct observation of the excitation blockade for highly Stark-shifted Rydberg atoms induced by controllable dipole-dipole interactions. We investigate the electric field region around and above the classical ionization threshold, which is typically not considered suitable for blockade experiments. We excite Rydberg atoms in the energy region corresponding to the unperturbed $43S_{1/2}$ state at electric fields around 127 V/cm out of a magneto-optically trapped cloud of ^{87}Rb atoms with a temperature of 150 µK. We tune the dipole-dipole interaction by the applied electric field thus changing the electric dipole moment of the excited state. The position of the Rydberg atoms is detected by ionization and subsequent ion imaging; the controlled ionization of the atoms is achieved by adiabatic transfer of the Rydberg state to an ionizing state. For the spatially resolved detection of the atoms, a high resolution ion microscope for cold atoms has been developed and experimentally characterized. It features a maximum magnification of 1000 and sub-micrometer spatial resolution. A theoretical treatment of highly Stark-shifted Rydberg states is developed introducing a complex absorbing potential. It is capable of predicting the ionization rates of the Rydberg states for a wide range of electric fields and energies with only one free parameter. Together with the numerical calculations, measurements of the ionization spectra for different Rydberg states are presented. The $43S_{1/2}$ state is measured in an electric-field range from 125 V/cm to 165 V/cm (classical ionization limit 127 V/cm), the $70S_{1/2}$ state in an electric-field range from 15 V/cm to 35 V/cm (classical ionization limit 16.1 V/cm) and the $100S_{1/2}$ state in an electric-field range from 7 V/cm to 19 V/cm (classical ionization limit 3.7 V/cm). Our results show an intricate energy level struc-

ture with broad, strongly ionizing states as well as sharp, nearly non-ionizing states. The numerical calculations are also used for the prediction of selective field ionization spectra and the results are used to identify Förster resonances in the Stark spectrum of the $45D_{5/2}$ state. Complementary to the spatially resolved measurements in high electric fields, the Rydberg blockade effect is also observed via the excitation number statistics at Förster resonances.

Zusammenfassung

Rydbergatome, d.h. Atome mit einem oder mehreren hochangeregten Elektronen, weisen überhöhte Eigenschaften im Vergleich zu Grundzustandsatomen auf. So sind zum Beispiel ihre Energieniveaus sehr empfindlich auf externe elektrische Felder (Stark-Effekt) und sie zeigen starke interatomare Wechselwirkungen, was zu einer Anregungsunterdrückung führen kann, die als Rydberg-Blockade bekannt ist. Letztere Eigenschaft macht Rydbergatome zu vielversprechenden Kandidaten für Quantensimulation und Quantencomputing. Die vorliegende Arbeit beschreibt die direkte Beobachtung der Anregungsblockade für hochgradig Stark-verschobene Rydbergatome induziert durch eine kontrollierbare Dipol-Dipol Wechselwirkung. Dabei wird der elektrischen Feldbereich um und über der klassischen Ionisierungsgrenze untersucht, welcher typischerweise nicht für Blockadeexperimente in Betracht gezogen wird. Rydbergatome werden im Energiebereich zugehörig zum unverschobenen $43S_{1/2}$-Zustand in elektrischen Feldern um 127 V/cm aus einer magneto-optisch gefangenen Wolke bestehend aus ^{87}Rb Atomen mit einer Temperatur von 150 µK angeregt. Die Stärke der Dipol-Dipol Wechselwirkung wird durch das angelegte elektrische Feld eingestellt, welches das elektrische Dipolmoment des angeregten Zustands verändert. Die Position der Rydbergatome wird nachgewiesen, indem sie ionisiert und durch eine Ionenoptik abgebildet werden. Eine kontrollierte Ionisation der Atome wird dabei durch einen adiabatischen Transfer des Rydbergzustands zu einem ionisierenden Zustand gewährleistet. Für den räumlich aufgelösten Nachweis der Atome wurde ein hochaufgelöstes Ionenmikroskop für kalte Atome entwickelt und experimentell charakterisiert. Es besitzt einen maximalen Vergrößerungsfaktor von 1000 und eine sub-mikrometer Auflösung. Eine theoretische Beschreibung von hochgradig Stark-verschobenen Rydbergzuständen wird durch die Einführung eines komplexen, absorbierenden Potentials ermöglicht. Die Theorie erlaubt die Vorhersage der Ionisationsraten der Rydbergzustände für einen großen Feld- und Energiebereich mit nur einem freien Parameter. Zusätzlich zu den numerischen Berechnungen werden die Ionisationsspektren verschiedener Rydbergzustände vorgestellt. Der $43S_{1/2}$-Zustand

wird in einem elektrischen Feldbereich von 125 V/cm bis 165 V/cm gemessen (klassisches Ionisierungslimit von 127 V/cm), der $70S_{1/2}$-Zustand in einem Feldbereich von 15 V/cm bis 35 V/cm (klassisches Ionisierungslimit 16.1 V/cm) und der $100S_{1/2}$-Zustand in einem Feldbereich von 7 V/cm bis 19 V/cm (klassisches Ionisierungslimit 3.7 V/cm). Unsere Ergebnisse zeigen eine komplizierte Energieniveaustruktur sowohl mit breiten, stark ionisierenden Zuständen als auch mit scharfen, nahezu nichtionisierenden Zuständen. Die numerischen Berechnungen werden zudem verwendet, um selektive Feldionisationsspektren vorherzusagen. Die daraus resultierenden Ergebnisse erlauben die Identifikation von Försterresonanzen im Stark-Spektrum des $45D_{5/2}$-Zustands. Ergänzend zu den räumlich aufgelösten Messungen im hohen elektrischen Feld wird der Rydberg-Blockadeeffekt auch in der Statistik der Anzahl der nachgewiesenen Rydbergatome an Försterresonanzen beobachtet.

List of publications

Accepted papers

- Publication [1]:
  "A high resolution ion microscope for cold atoms",
  M. Stecker, H. Schefzyk, J. Fortágh and A. Günther,
  New Journal of Physiscs 19, 043020 (2017).

- Publication [2]:
  "Ionization spectra of highly Stark shifted rubidium Rydberg states",
  J. Grimmel, M. Stecker, M. Kaiser, F. Karlewski, L. Torralbo-Campo, A. Günther, and J. Fortágh,
  Physical Review A 96, 013427 (2017).

Manuscript ready for submission

- Manuscript [3]:
  "Controlling the dipole blockade of highly Stark-shifted rubidium Rydberg states",
  M. Stecker, J. Grimmel, R. Nold, M. Reinschmidt, J. Fortágh, and A. Günther,
  to be submitted (2018).

Personal contribution

- Publication [1]:
  I contributed to the setup of the experimental system including the ion microscope, the laser system and the vacuum system. I had the main responsibility for the characterization measurements of the ion-optical system and the

data analysis. I performed parts of the simulations and wrote major parts of the manuscript.

- Publication [2]:
  I had the main responsibility for developing the concept for the experiment, performing the measurements and analyzing the data. I was involved in the development of the numerical methods and wrote parts of the manuscript.

- Manuscript [3]:
  I had the main responsibility in developing the measurement concept, setting up the experiment and performing the measurements. I analyzed the data and wrote major parts of the manuscript.

1. Introduction

One of the main goals of modern physics for the past decades has been the realization of a controllable, coherent many-body quantum system. Such a universal quantum simulator represents a versatile tool for reproducing the dynamics of an arbitrary interacting quantum system - a task that even with a simplified model is often beyond the reach of classical computers for systems with more than a few tens of particles [4]. Quantum simulators promise to give new insights for example into strongly correlated quantum systems [5] and highly entangled quantum states [6, 7]. They are expected to shed light onto unresolved questions like high-temperature superconductivity [8] and can lead to the realization of new non-equilibrium states of matter [9].

Basic quantum simulators have been realized with ions [10–12], superconducting qubits [13, 14] and arrays of atoms [15, 16]. The latter makes use of the recently developed quantum gas microscope, where single atoms are trapped in an optical lattice and single site resolved detection is achieved by fluorescence imaging [17, 18]. The atoms can hereby be arranged in arbitrary two-dimensional configurations with the most recent development allowing a defect-free atom-by-atom assembly [19, 20]. These methods can be combined with quantum simulators based on Rydberg atoms [21]. Quantum Ising models have been realized with two-dimensional arrays of single Rydberg atoms [22, 23] and studying the many-body dynamics in a 51-atom quantum simulator [24] and the coherent dynamics in a long-range interacting Ising chain [25] became possible.

A large scale quantum simulator can also be a key ingredient for quantum information processing [26]. While classical computers store information in bits, which have either the state 0 or 1, quantum computers use qubits, which are quantum states that can be in a superposition between 0 and 1. Computational operations on qubits can be realized by quantum gates [27]. Quantum computers are interesting beyond the scope of fundamental research because they promise a dramatic speedup of certain computational routines like factoring integers [28]. Several systems have been investigated with regard to the realization of quantum information processing for example

trapped ions [29], superconducting circuits [30], quantum dots [31], linear optics [32] and neutral atoms [33]. Ions with their strong Coulomb interaction allow for high-fidelity gate operations [34] but as the interaction is always present, this also poses a challenge in terms of scalability. In contrast to that, neutral atoms in the ground state are weakly interacting and can be arranged in large optical lattice structures [33]. For the efficient performance of quantum gate operations the interaction can be enhanced by many orders of magnitude when exciting the atoms to a Rydberg state as proposed in [35, 36] and realized in [37, 38]. Hybrid approaches combine superconducting circuits and neutral atoms by coupling superconducting microwave resonators to Rydberg atoms [39, 40]. While superconducting circuits are capable of performing fast gate operations, ultracold atoms are superior in terms of coherence times [41].

Rydberg atoms are atoms with high principal quantum number n and show in many ways exaggerated properties in comparison to atoms in low quantum states [42]. For alkali atoms, the spectrum is similar to that of hydrogen and the energy levels can be quantified by

$$E_{nlj} = -\frac{hc \cdot R_M}{(n - \delta_{nlj})^2}, \tag{1.1}$$

with the isotope-dependant Rydberg constant R_M[1] and the quantum defect δ_{nlj}, which depends on the principal quantum number n as well as the orbital angular momentum l and the total angular momentum j. The quantum defect characterizes the deviation of the energy levels of the alkali atom compared to the levels of the hydrogen atom. With increasing l, the quantum defect δ_{nlj} approaches zero and the energy levels become more and more hydrogen-like. As we can see in Eq. 1.1, the energy levels scale with the principal quantum number as n^{-2}. Similar power laws apply for many other properties of Rydberg atoms, for example the size of the electron orbit scales as n^2, the radiative lifetime as n^3, the polarizability as n^7 and the van der Waals interaction as n^{11} [42]. The high polarizability makes the energy levels of Rydberg atoms very sensitive to external electric fields (Stark effect) which results in a rich Stark spectrum. For an electric field around and above the classical ionization limit, the spectrum is strongly affected by ionization due to tunneling through the potential barrier as well as direct coupling to the continuum. The classical ionization

[1] $R_M = R_\infty/(1 + m_e/M)$, with electron mass m_e, core mass M and Rydberg constant for infinite core mass R_∞.

limit describes the electric field at which the electron is classically allowed to leave the potential of the core.

The dipole-dipole interaction that makes Rydberg atoms interesting for quantum gate operations generally scales with the interatomic separation r as r^{-3}. At zero electric field, Rydberg states do not exhibit a permanent electric dipole moment. Thus, their interatomic interaction is of second order [43] and is referred to as van der Waals interaction with the interaction potential

$$V_{vdW} = -\frac{C_6}{r^6}. \tag{1.2}$$

As mentioned above, the C_6 coefficient scales as n^{11}, so the van der Waals interaction of Rydberg atoms can get extremely strong on mesoscopic length scales of a few micrometers. In contrast to that, the interaction between ground-state atoms is negligibly small at these distances.

In the presence of an external electric field, the Rydberg atoms can carry a permanent electric dipole moment and the interaction type changes from van der Waals to dipole-dipole. The interaction potential can be expressed as

$$V_{dd} = -\frac{C_3}{r^3}, \tag{1.3}$$

with C_3 generally scaling as n^4 [43].

The strong interaction between Rydberg atoms leads to a phenomenon known as the Rydberg blockade [44]. When a Rydberg atom is excited, the interaction potential shifts the energy of a second excitation. If the shift is larger than the excitation bandwidth, the excitation of a second Rydberg atom is suppressed in the vicinity of the first one (see Fig. 1.1). A blockade radius can be defined as the distance, where the shift by the interaction potential equals the excitation bandwidth. If we look at the problem in a many-body picture, the blockade effect gives even more important implications. Within one blockade sphere, the excitation is distributed over all N ground state atoms. The coupling to this collective state is then enhanced by $\sqrt{N}$. This fact is important for the usage of Rydberg atoms in quantum information protocols that store the quantum information in collective states of mesoscopic ensembles [36].

The direct observation of the Rydberg blockade requires spatially resolved detection of Rydberg atoms. The most common technique for the detection of ultracold atoms is absorption imaging with a laser beam resonant to an atomic transition [45].

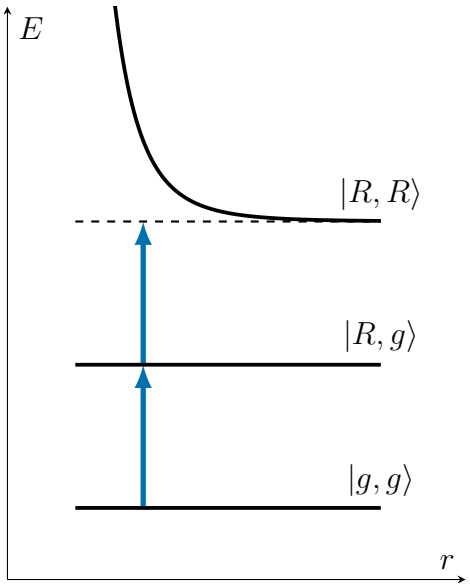

Figure 1.1.: Illustration of the blockade effect. Depicted is the energy E with respect to the interatomic separation r of a two-atom state with both atoms in the ground state $|g, g\rangle$, one atom excited to a Rydberg state $|R, g\rangle$ and both atoms excited to a Rydberg state $|R, R\rangle$. The state $|R, R\rangle$ is shifted out of resonance by the interaction potential for small separations.

By quantifying the absorption, the atomic density of the sample can be determined and with that also the overall number of particles. After the imaging process, the atoms are lost out of the trap, so a new cloud has to be prepared for the next experimental cycle. The destruction can be circumvented for example by phase contrast imaging [46] or fluorescence imaging [47] as for example used in the quantum gas microscopes for single atom detection [17, 18]. Rydberg atoms can be detected either by pumping the Rydberg states back to the ground state or by detecting losses in the ground state population. An alternative approach to achieve single atom resolution is ionization of the neutral atoms and detection of the resulting ions or electrons. This can also be used for spatially resolved imaging, for example by accelerating the ions in a divergent electric field [48] and detecting them by a microchannel plate detector (MCP). Another detection method uses the electron beam of a scanning electron microscope to ionize the sample sequentially [49].

In this work, a new approach is presented for in-situ and real-time imaging of ultracold atomic gases [1]. An ion-optical system with four consecutive lenses has been developed, realized and experimentally characterized by ionization out of a continuously operated magneto-optical trap (MOT) of rubidium atoms. For spatially resolved single ion detection, an MCP with delay-line detector is placed in the image

plane of the ion-optical system. The microscope features a theoretical resolution of 100 nm and a variable magnification up to 1000. Besides detecting ground state atoms via direct photoionization, the microscope can also be used to detect Rydberg atoms. State selective detection is achieved by field ionization and subsequent ion imaging. The system constitutes a new tool for measuring Rydberg atoms in external electric fields as well as their interaction with each other.

With our experimental setup, the ionization spectra of ^{87}Rb were measured and theoretically modelled by a complex absorbing potential (CAP) for different Rydberg states in electric fields up to far above the classical ionization threshold [2]. The very good agreement between theory and experiment showed that our numerical calculations can be used to accurately predict energy, ionization rate and electric dipole moment of highly Stark-shifted Rydberg states. Therefore, the CAP theory was used to predict selective field ionization spectra and the numerically calculated spectra were compared to spectra obtained when exciting Rydberg atoms to so-called Förster resonances.

Despite the fact that the high-field region is generally governed by ionization, our work showed that there are still sharp resonances with Rydberg states that have a very small ionization rate and are therefore relatively long lived. These results led to the direct oberservation of the Rydberg blockade in high electric fields in the vicinity of the classical ionization limit with our ion microscope. Up to now, the blockade effect has been observed in a zero electric field environment [44, 50] and in small electric fields [51, 52]. The rich level structure of the the high-field Stark spectrum gives us the opportunity to find states with very different dipole moments and by that with different interaction strengths. Furthermore, we developed a novel ionization scheme for subsequent spatially resolved detection by our ion microscope. By adiabatic transfer of the Rydberg population from the initial non-ionizing state to an ionizing state, which only requires a small changes in the electric field, we gain precise control over the detection process [3].

2. An ion microscope for cold atoms

The foundation of all the measurements presented in this work is an ion microscope for cold atoms. In this chapter, the ion-optical system as well as the laser system that is used to cool, trap and excite the atoms will be discussed. The microscope is used to image ions out of a cold atomic sample with high temporal and spatial resolution and single particle sensitivity. Therefore, it enables us to directly measure spatial and temporal Rydberg-Rydberg correlations. The system is also suitable to perform high precision spectroscopy on Rydberg states with or without an external electric field applied. It is worth noting that despite the fact that, throughout this work, the ion microscope is mainly used to detect Rydberg excitations ionized by field ionization, it can also be used to detect ground state atoms with a suitable ionization scheme for example by photoionization as demonstrated in Sec. 2.3. The microscope has been designed by Hannah Schefzyk in the framework of her PhD thesis [53] and put into operation in collaboration with her.

2.1. Laser system

In order to cool and trap ^{87}Rb atoms, a standard six-beam magneto-optical trap (MOT) is used (see Fig. 2.1). A cooling laser at around 780.246 nm wavelength drives the cooling transition $|5S_{1/2}, F = 2\rangle \rightarrow |5P_{3/2}, F = 3\rangle$ [54] with about 12 MHz red detuning (25 mm beam diameter). The cooling laser is a grating stabilized diode laser in Littrow configuration [55] with the frequency stabilized via a beat lock to a reference laser, which itself is stabilized with a Rb saturation spectroscopy to the crossover resonance between $|5P_{3/2}, F = 3\rangle$ and $|5P_{3/2}, F = 2\rangle$. A second laser (repumper) drives the transition $|5S_{1/2}, F = 1\rangle \rightarrow |5P_{3/2}, F = 2\rangle$ in order to pump back atoms into the cooling cycle, which they may have left due to off-resonant scattering of the cooling light. The repumper is injection locked to another laser, which itself is beat locked to the reference laser at the frequency of the ground-state hyperfine splitting (around 6.8 GHz). By shifting the frequency of the blue laser

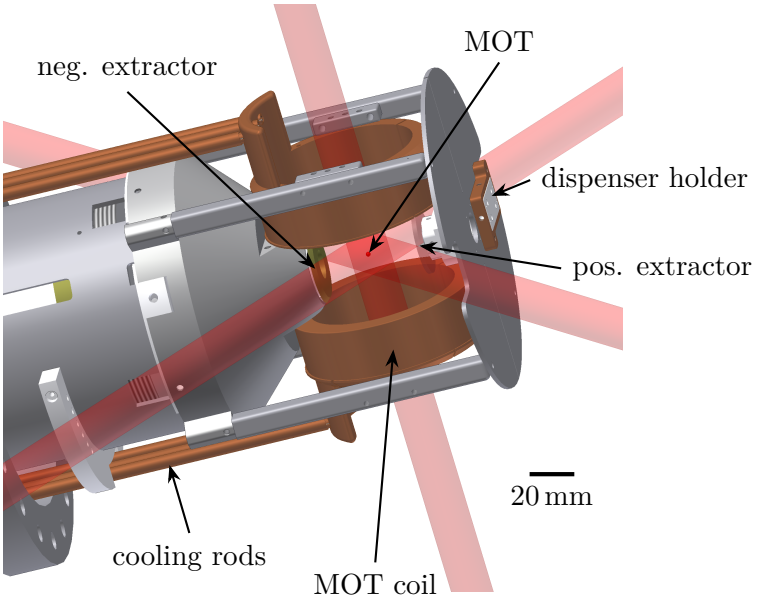

Figure 2.1.: Part of the setup where the magneto-optical trap (MOT) is formed by six intersecting laser beams and a magnetic field formed by two coils. The MOT is located in the center between the two extractor electrodes. The positive extractor consists of transparent glass coated with indium tin oxide (ITO) to allow for optical access from this direction. The MOT is loaded with ^{87}Rb atoms provided by current-heated dispensers. Figure and caption taken from [1] and adapted.

with acousto-optic modulators (AOMs), a beam resonant to the $|5S_{1/2}, F = 2\rangle \rightarrow |5P_{3/2}, F = 3\rangle$ transition and another beam that is 133 MHz blue detuned to this transition are provided. This enables us to choose between three different excitation paths for Rydberg S or D states via the intermediate $|5P_{3/2}\rangle$ state:

$$|5S_{1/2}, F = 2\rangle \rightarrow |5P_{3/2}, F = 3\rangle \rightarrow |nS, nD\rangle\,, \tag{2.1}$$

with the first transition either resonant or off-resonant with 12 MHz red or 133 MHz blue detuning (cf. Fig. 2.2). When a far off-resonant path like the latter is chosen, it is convenient to use a blue detuning in order to avoid population of the lower lying hyperfine substates of the $5P_{3/2}$ level.

The upper transition to a Rydberg state or for direct ionization above threshold is provided by a second laser (Toptica DL SHG) running at a wavelength of around 480 nm. For direct ionization from the $|5P_{3/2}, F = 3\rangle$ state, the zero field ionization threshold has to be exceeded, which corresponds to a wavelength of the laser of ≤ 479.06 nm. Below threshold, Rydberg states can be excited down to $n \approx 32$, which corresponds to about 482 nm. The Rydberg laser consists of a grating stabilized

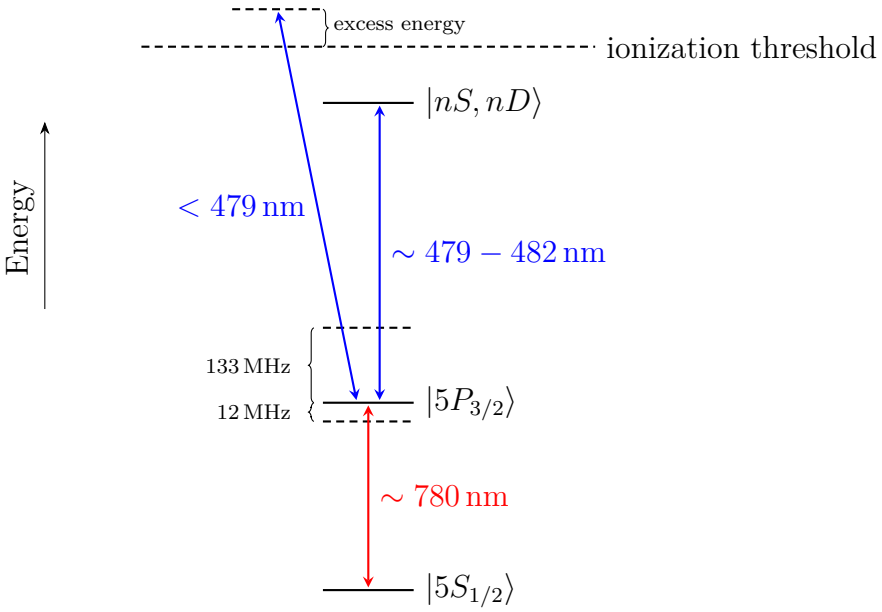

Figure 2.2.: Laser excitation scheme for rubidium Rydberg states or direct photoionization. For the lower transition, laser light tuned on resonance can be used as well as the cooling laser from the MOT with a red detuning of 12 MHz or an off-resonant beam with a blue detuning of 133 MHz. The upper transition can be used to excite Rydberg S and D states or can be tuned above threshold for direct photoionization.

diode laser running at about 960 nm and a frequency doubling unit with a PPLN[1] doubling crystal in a bow-tie cavity. The laser is frequency stabilized to a HighFinesse Wavelength Meter WS-U[2]. With the help of a fast AOM[3], the light can be switched with a rise time of around 10 ns for short excitation pulses.

2.2. Ion-optical system

The ion-optical system of the microscope consists of a pair of extractor electrodes, a set of four consecutive einzel lenses and a micro channel plate (MCP) in conjunction with a delay line detector. The complete setup is depicted in Fig. 2.3. The MOT is placed in the center between the extractor electrodes (cf. Fig. 2.1), which form the electric field to extract ions out of the cold atomic cloud. The magnified imaging is done with the einzel lenses, each one forming a magnified, intermediate image. An einzel lens is a type of lens for charged particles that consists of three axially

[1] Periodically Poled Lithium Niobate.
[2] A WS-U30 with 30 MHz absolute accuracy and 5 MHz measurement resolution and later a WS-U2 with 2 MHz absolute accuracy and 0.5 MHz measurement resolution was used.
[3] AA Opto Electronic MT200-A0.5-VIS (200 MHz, $0.5 \times 2\,\mathrm{mm}^2$ aperture).

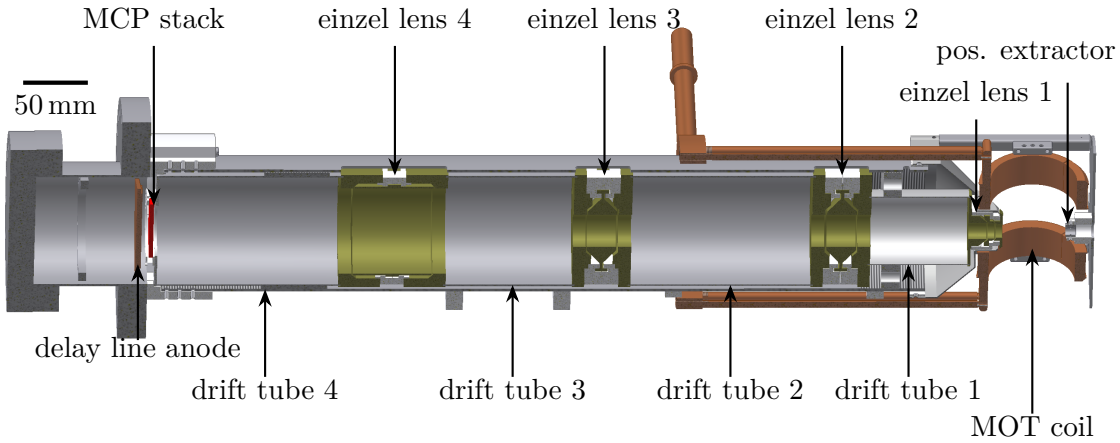

Figure 2.3.: Cross-section of the full ion optics setup inside the vacuum chamber. Each einzel lens consists of three electrodes. Usually, the two outer electrodes are held at the same electric potential; the focal length of the lens can be varied by the potential of the inner electrode. The outer electrode of einzel lens 1 that faces towards the MOT also acts as the negative extractor electrode. Figure and caption taken from [1] and adapted.

symmetric electrodes with apertures. The outer electrodes are typically held at the same potential, such that the particle's energy remains unchanged after exiting the lens. With the voltage at the center electrode, the focal length of the lens can be tuned. The MCP together with the delay line detector is used to achieve a spatially resolved ion image. The MCP has a pore distance of 17 µm, so with the Nyquist Shannon sampling theorem [56] $M \times 2 \times 17\,\mu\text{m}$ poses the fundamental limit of the resolution of the microscope. Here, M denotes the magnification of the system.

The design of the ion-optical system was done by means of the charged particle trajectory simulation program SIMION. To optimize the resolution of the imaging system, the relevant aberrations were considered and minimized as far as possible. Spherical aberration was limited by the use of several einzel lenses instead of a single one. Aperture size and length of the electrodes were optimized to get an acceptable compromise between smallest possible spherical aberration on the one hand and the geometrical dimensions and magnitude of the applied voltages on the other. Other aberrations that were considered are astigmatism and distortion, which are inherent features of einzel lenses, and chromatic aberration. The latter arises due to the fact that the ions typically have a starting energy distribution. This energy is dominated by the kinetic energy of the atoms in the MOT and the excess energy from the photoionization process. The temperature of the MOT is typically around 150 µK, which corresponds to a kinetic energy of 12.9 neV. The excess energy (see Fig. 2.2)

is distributed on electron and ion correspondingly to their mass ratio. With the blue laser tuned to 479.04 nm (excess energy of 104 µeV), the energy transferred to the ion is 0.65 neV. The simulations show that the resolution limit of the imaging systems is not affected by chromatic aberration for an upper limit of the starting energy of 2.5 µeV. Furthermore, the microscope was designed to have a depth of field of 50 µm in order to be able to image thee-dimensional samples. The overall resolution of the system depends on the distance to the optical axis. Close to the optical axis, it is better than 10 nm, but further away the resolution limit lies at around 50 nm. This result is nicely visualized in Fig. 2.4, where the imaging of several test patterns of different sizes has been simulated.

2.3. Experimental characterization of the microscope

For the experimental characterization of the microscope, cold atoms from the MOT were photoionized in a two-step process. The first step from the $|5S_{1/2}, F = 2\rangle$ to the $|5P_{3/2}, F = 3\rangle$ state is provided by the cooling laser, the second step from the 5P state to the continuum by the blue laser tuned to a wavelength of 479.04 nm. Relatively big structures with a structure size down to 20 µm were imprinted onto the MOT with the blue laser via light-optical imaging of a USAF 1951 resolution test target (see Fig. 2.5a). The structures are mapped onto the ion image as the photoionization rate is proportional to the light intensity. These structures could be imaged with a contrast near 1 and were used to characterize the behavior of each lens individually. The results are in accordance to the simulations.

For smaller structures, a variable standing wave pattern was overlapped with the MOT by superimposing two blue beams under a variable angle. In this way, structures down to 2.7 µm could be realized and imaged (see Fig. 2.5b). The fringe contrast in this measurement was 0.32. It is not possible to calculate a resolution limit out of this contrast as the large depth of field of our microscope adds an offset to the ion signal coming from areas with low overlap of the interfering beams. Even so, the 2.7 µm is clearly resolvable, so the results imply that the actual resolution limit lies lower.

The ultimate resolution limit could be tested with smaller structures for example by the standing wave pattern of a retro-reflected ionization laser. As this fringe spacing with 240 nm would be more than one order of magnitude smaller than the smallest structure demonstrated in this work, a variable fringe distance similar to the

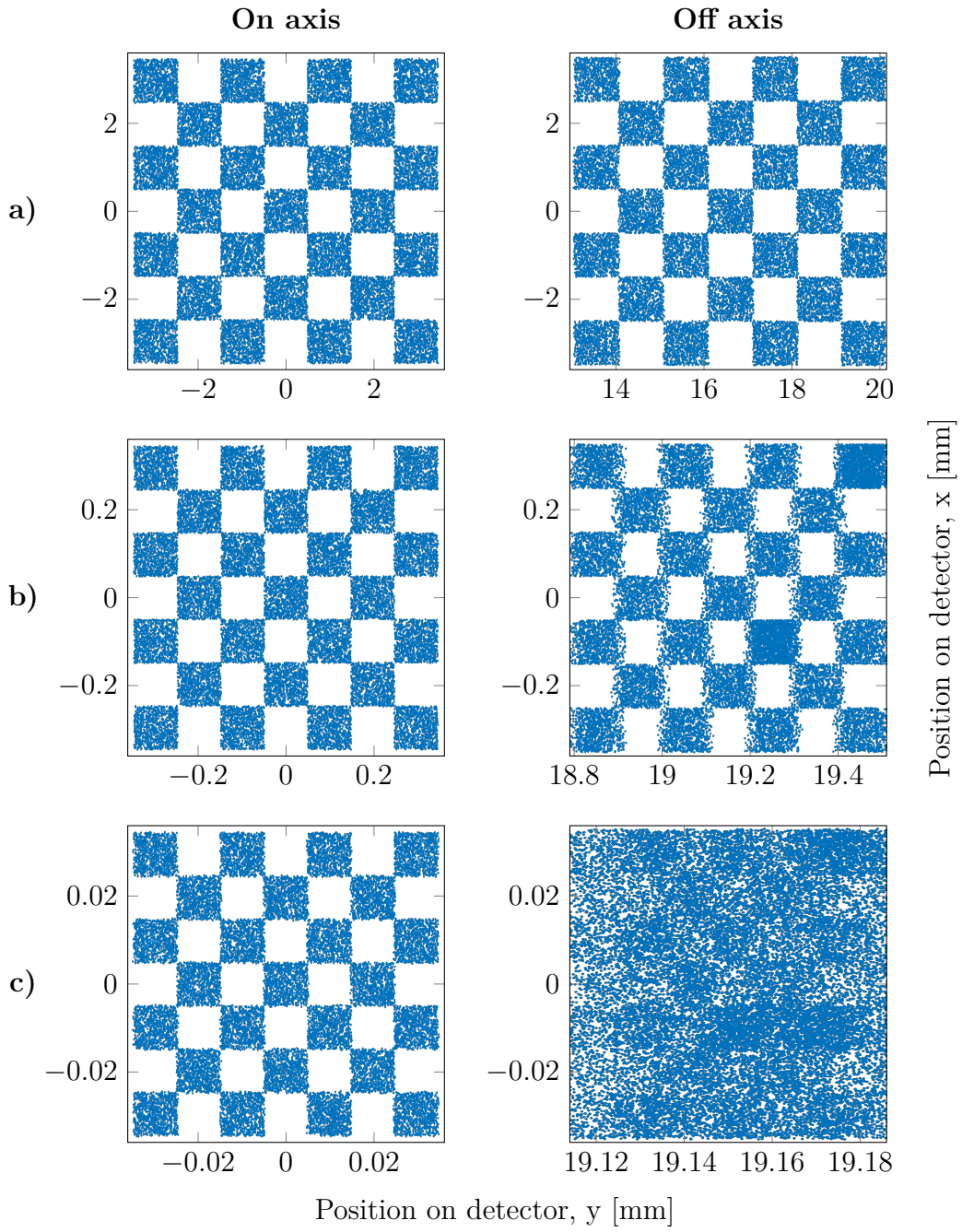

Figure 2.4.: Simulated imaging of several test patterns near (top row) and 19 µm away (bottom row) from the optical axis (ion optics set to a magnification of 1000). The test structures consist of cuboids of different sizes filled with ions: a) 1 µm × 1 µm, b) 100 nm × 100 nm, c) 10 nm × 10 nm. The extent along the optical axis is always 50 µm, the starting energy 9.3 neV. Figure and caption taken from [1] and adapted.

technique implemented for this work is advisable. Besides the aberrations mentioned above, the resolution of the system also depends on the stability of the voltage sources of the electrodes. Simulations suggest a stability of $\pm 0.05\%$ in order to not limit the resolution; a requirement that should be met by our voltage supplies as measurements indicate a short term stability of $\pm 0.02\%$. Further limiting factors for the resolution of the system are deviations from rotational symmetry, the signal characteristics of the delay line and the detector electronics.

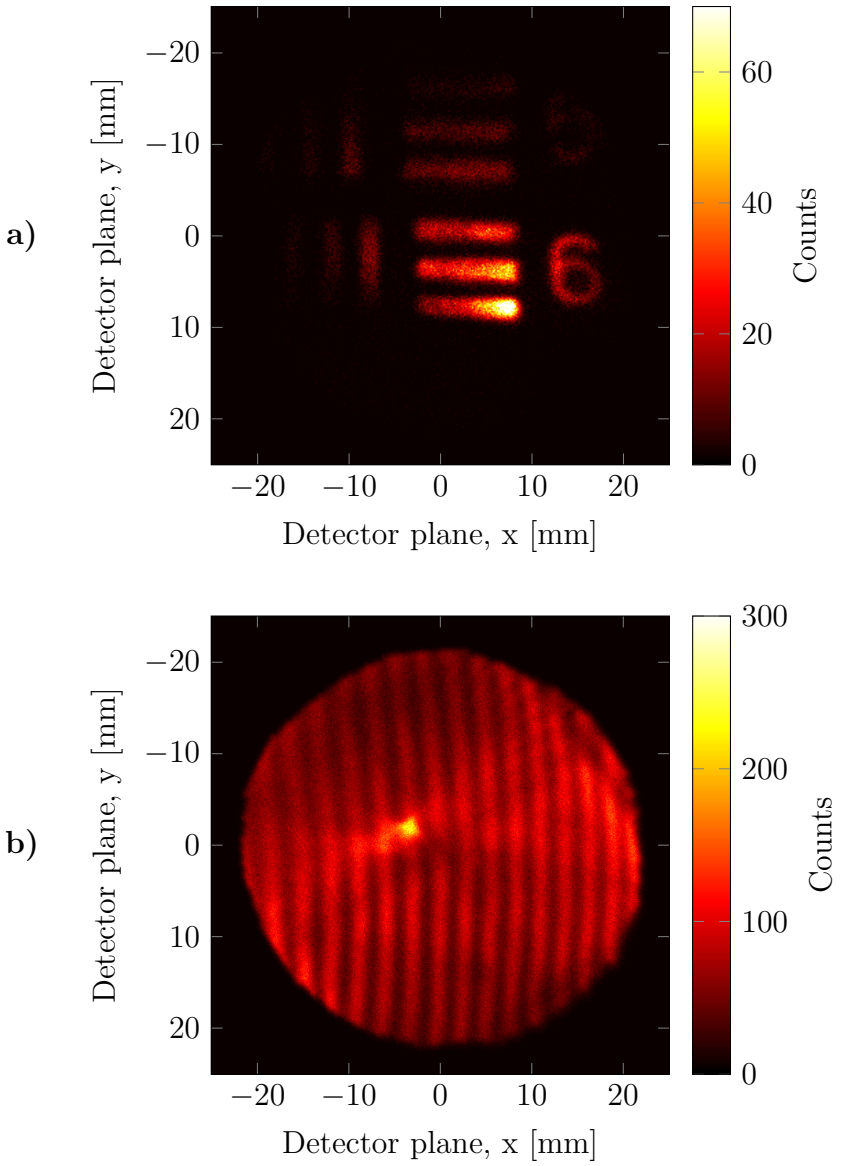

Figure 2.5.: Ion-optical imaging of a MOT onto the MCP with the ionization laser intensity spatially modulated. a) Modulation by projection of a USAF1951 test structure onto the MOT. The visible bar structure (next to the number six) has a center to center distance of 80 µm at the position of the MOT. The magnication is about 50. b) Modulation by an interference structure with fringe spacing of 2.7 µm. The magnification is 1050. The bright spot in the middle is produced by ions from outside of the detection region whose trajectories are diverted back into the image plane. Figures taken from [1].

3. Rydberg Stark spectroscopy

The Stark effect describes the shifting and splitting of atomic energy levels in the presence of an external electric field. While this effect is negligible for ground state atoms at electric field strengths that we can produce in our experimental setup (up to around 300 V/cm), Rydberg atoms with their high polarizability experience strong Stark shifts. Furthermore, at sufficiently high field strengths, the Stark spectrum is altered by varying ionization rates of the different Stark-shifted states. Both theoretical calculations and experimental observation of Stark spectra in different electric field regimes are presented in this chapter. With a profound understanding of the Stark spectra, the calculations can be used for calibrating the electric field in the experiment and predicting selective field ionization signals (Chap. 4). They are also the basis for making use of the Stark shift in order to control Rydberg-Rydberg interactions and the ionization behavior of highly Stark-shifted Rydberg states (Chap. 5).

3.1. Stark effect

The Hamiltonian $\hat{H}$ for an atom in an external electric field F in z-direction can be written in atomic units as

$$\hat{H} = \hat{H}_0 + F\hat{z}, \tag{3.1}$$

with $\hat{H}_0$ representing the unperturbed Hamiltonian. The hyperfine splitting is omitted as it is below the frequency resolution of our measurements. It is on the order of 100 kHz for Rydberg S-states with principal quantum numbers $n > 40$ used in this work (for D-states, it is completely negligible) [57–59]. While, for hydrogen, the problem is separable in parabolic coordinates, for alkali atoms this is not the case anymore due to the finite sized ionic core. From the field-free eigenstates $|n, l, j, m_j\rangle$ only m_j remains a good quantum number. States that are independent in the hydro-

genic case are now coupled and do not cross like in hydrogen but exhibit anticrossings. Solutions with the same $|m_j|$ are degenerate; the solutions of different $|m_j|$-values are independent. In the $|n, l, j, m_j\rangle$ basis, the Stark-shifted states in an electric field are mixtures of different zero-field eigenstates. In order to numerically solve the problem for alkali atoms, a matrix representation of $\hat{H}$ in a subset of the basis given by $\hat{H}_0$ is used [60, 61]. $\hat{H}_0$ is diagonal and contains the unperturbed atomic energy levels determined with experimentally obtained values for the corresponding quantum defects (Eq. 1.1) [57, 62–64]. The matrix representation of $F\hat{z}$

$$\langle n, l, j, m_j | F\hat{z} | n', l', j', m_j' \rangle = F \cdot \langle n, l, j, m_j | r \cos\Theta | n', l', j', m_j' \rangle \tag{3.2}$$

is essentially calculated by evaluating the radial overlap integral

$$\langle n, l, j, m_j | r | n', l', j', m_j' \rangle \tag{3.3}$$

and the angular matrix elements

$$\langle l, m_l | \cos\theta | l', m_l' \rangle \,. \tag{3.4}$$

For the radial part, the knowledge of the radial wavefunctions of the states is necessary. They can be obtained by numerically solving the radial Schrödinger equation with a parametric model potential [65]. The resulting matrix representation of $\hat{H}$ is then diagonalized for every value of F and by that, the Stark-shifted energy levels are obtained. The results for the $41S_{1/2}$ Rydberg state of Rb can be seen in Figs. 3.1b and d. A measure for the transition strength can be introduced by calculating the transition dipole matrix elements for the transition between the 5P and the Rydberg state [61]:

$$D = \sum_{m_F} \eta_{m_F} \left| \left\langle \mathrm{Ryd} \left| \, \vec{\epsilon}_R \vec{r} \, \right| 5P_{3/2}, F = 3, m_F \right\rangle \right|^2 . \tag{3.5}$$

The matrix elements are weighed by a factor η_{m_F}, which accounts for the transition between the 5S and 5P state and is calculated by evaluating the transition dipole matrix elements between those states. $\langle \mathrm{Ryd}|$ denotes the Stark-shifted Rydberg state, $\vec{\epsilon}_R$ is the polarization of the Rydberg laser.

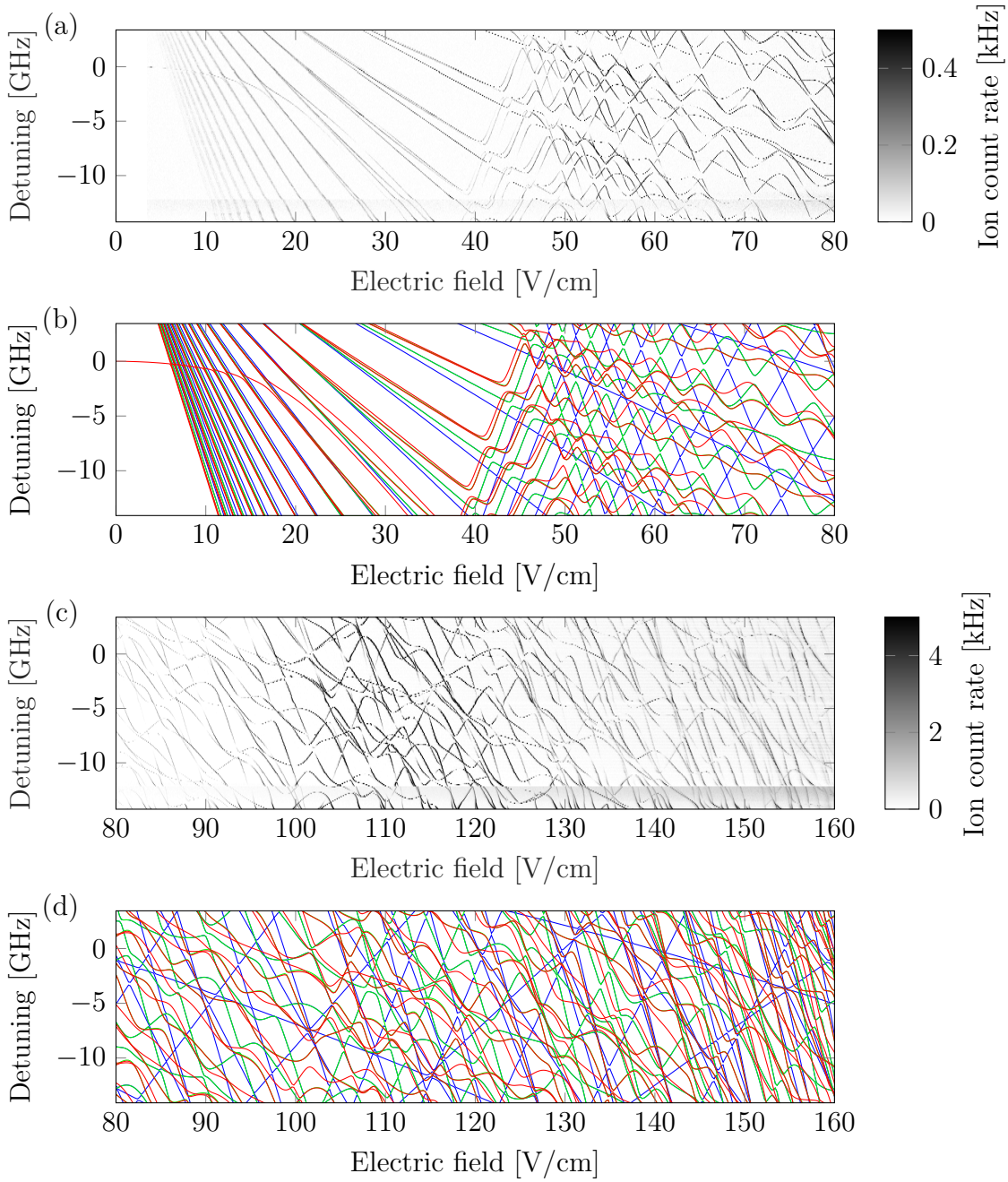

Figure 3.1.: Stark spectrum near $41S_{1/2}$. The detuning is given relative to the unperturbed state. (a) and (c) show the detected ion signal from the experiment. The measurement does not start at 0 V/cm as there is a small residual field when the extractors are at 0 V. The decrease of the count rate for fields > 125 V/cm is due to a decrease in detection efficiency. (b) and (d) show the results from the numerical calculations following the method described in Sec. 3.1 with $m_j = 0.5$ (red), 1.5 (green) and 2.5 (blue). We applied a linear scaling to match the electric field from the experiment to the theoretical results. The transition strength D is omitted in this plot. The classical ionization threshold is located at ≈156 V/cm.

3.2. Ionization spectra and complex absorbing potential

While the method presented in Sec. 3.1 can accurately predict the energy levels of Stark-shifted Rydberg states even in high electric fields above the classical ionization threshold, it cannot correctly reproduce the spectra obtained at high fields as the shape of the resonances is dominated by ionization. For hydrogen, the ionization rate (and with that the width of the resonance) grows exponentially with the electric field [66]. Alkali-metal Rydberg states, however, have a more interesting spectrum with strongly varying ionization rates where even in high fields states with nearly suppressed ionization can be found [42].

To include this coupling to the continuum in the existing numerical calculations, we extended the Hamiltonian of Eq. 3.1 by introducing a complex absorbing potential (CAP). This artificial potential absorbs the asymptotic part wavefunction and makes all eigenfunction L^2. The CAP method was first introduced for the time-dependent wavepacket propagation in order to avoid reflections at the end of the numerical grid [67]. It was later shown, that the method can also be used in a time-independent context to calculate resonance energies and widths [68] and has been applied to study the Stark effect [69].

In our case, we chose a complex absorbing potential of the form

$$V_{\mathrm{CAP}} = -i\eta W(\hat{r}, F) \tag{3.6}$$

$$W(\hat{r}, F) = \Theta(r - r_c(F)) \times (r - r_c(F))^6 \,, \tag{3.7}$$

with the cut-off radius r_c, a free parameter η and the Heaviside step function Θ. The cut-off is represented by the saddle point of a Coulomb potential in the electric field F with $r_c(F) = F^{-1/2}$. This point also defines the classical ionization threshold (in atomic units):

$$E_{\mathrm{Ion}} = -2\sqrt{F}. \tag{3.8}$$

Using this field dependent choice of the potential, the free parameter η only has to be determined once for a large span of both energy and electric field of the spectrum. This is done by variation of η at different electric field values and identifying a region, where a change in η leaves the resulting eigenvalues mostly unchanged. Conventio-

nally, the free parameter of the CAP would have to be adapted for every point in the spectrum.

When diagonalizing the matrix representation of this new Hamiltonian, we obtain complex eigenvalues of the form

$$E_C = E_r - i\frac{\Gamma}{2}, \tag{3.9}$$

with the real part E_r representing the energy level of the resonance and Γ its ionization rate. A plot of the expected spectrum can then be created by summing up Lorentzian peaks scaled with the transition strength D at the specific positions of the resonances E_r and with the corresponding widths Γ.

3.3. Measurement of Stark spectra

For the measurement of Stark spectra, the experimental setup described in Chap. 2 is used. Rydberg atoms are excited by continuously shining in the blue laser tuned to a certain frequency around the transition to the corresponding Rydberg state. The lower transition from the 5S to the 5P state is provided by the cooling beams (total power of 20 mW). The voltages applied to the extractor electrodes are ramped linearly with a slew rate of 1 V/s in order to cover the desired electric field region. The ions that are produced during the ramp are simultaneously detected by our ion-optical system. This time resolved ion signal can then be converted to a field dependent ionization spectrum by calculating a histogram. To obtain a full Stark spectrum, the field ramp is repeated for several frequency steps of the blue laser.

The Stark spectrum in the energy region around the unperturbed $41S_{1/2}$ state was measured up to the classical ionization limit of 156 V/cm. For the Rydberg excitation, the blue laser was shone in perpendicular to the ion-optical axis with a power of 2 mW and focused to a $1/e^2$ beam diameter of 15 µm at the position of the MOT (cf. Fig. 3.2). The beam had linear polarization oriented perpendicular to the ion-optical axis and with that also perpendicular to the electric field. The numerical calculations shown in Figs. 3.1b and d are in very good agreement with the measurements shown in 3.1a and c, which implies that the theory can be used to determine the electric field at the position of the atoms by measuring the Stark shift. The ion signal is weak for low electric fields because of low ionization rates. For this region, the measurement scheme of Sec. 4.2 has to be applied.

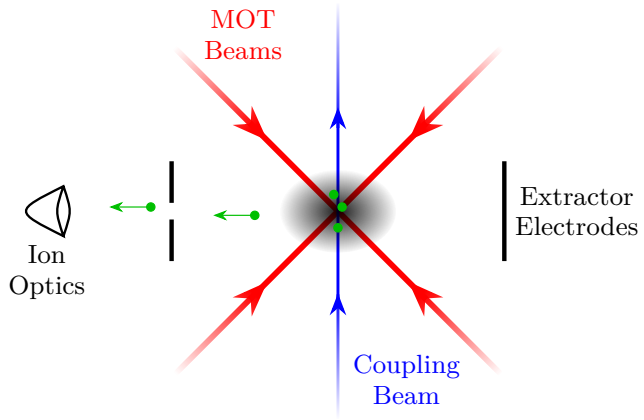

Figure 3.2.: Schematic diagram of the experimental setup. Rubidium atoms are trapped at the intersection of the MOT beams (red). Atoms from the MOT are continuously excited to Rydberg states by the Rydberg laser (blue) at various electric fields, which are applied via the extractor electrodes. The field is also used to guide the ions (green) to the ion optics. Figure and caption taken from [2] and adapted.

The region from around the classical ionization limit up to far above it was measured with the same experimental setup with the difference that the Rydberg laser had a power of 7 mW and was focused to a light sheet with $1/e^2$ beam diameters of 9 µm along the ion-optical axis and 80 µm perpendicular to it. Ionization spectra were obtained for states in the energy region of the unperturbed $43S_{1/2}$ (Fig. 3.3), $70S_{1/2}$ (Figs. 3.4 and 3.5) and $100S_{1/2}$ (Fig. 3.6). For these states, the classical ionization thresholds lie at 127 V/cm, 16.1 V/cm and 3.65 V/cm, respectively. For the first two, numerical calculations with a complex absorbing potential as described in Sec. 3.2 were performed with a basis size of 4000 and 10000 states, respectively. We find very good agreement between calculations and measurements, the resonance shapes are reproduced correctly even in the very high field region. This proves that our method is suitable for predicting the ionization rates and spectra of highly Stark-shifted Rydberg states. Theory and experiment show the expected broadening of the resonances with increasing electric field but also sharp resonances with low ionization rate even in high electric fields.

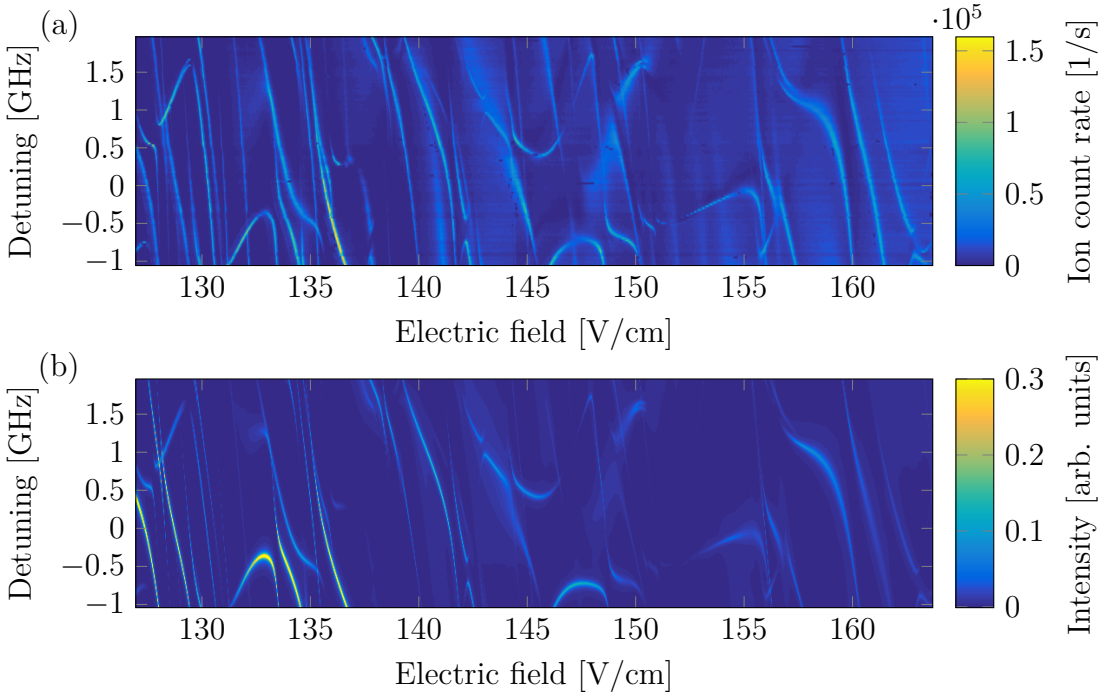

Figure 3.3.: Ionization Stark spectrum near $43S_{1/2}$. (a) Detected ion signal from the experiment. (b) Results from the numerical calculations for $\eta = 1 \cdot 10^6$. The detuning is given relative to the unperturbed state. We have applied a linear scaling to match the electric field from the experiment to the theoretical results. The classical ionization threshold is located at $\approx$127 V/cm. Figure and caption taken from [2].

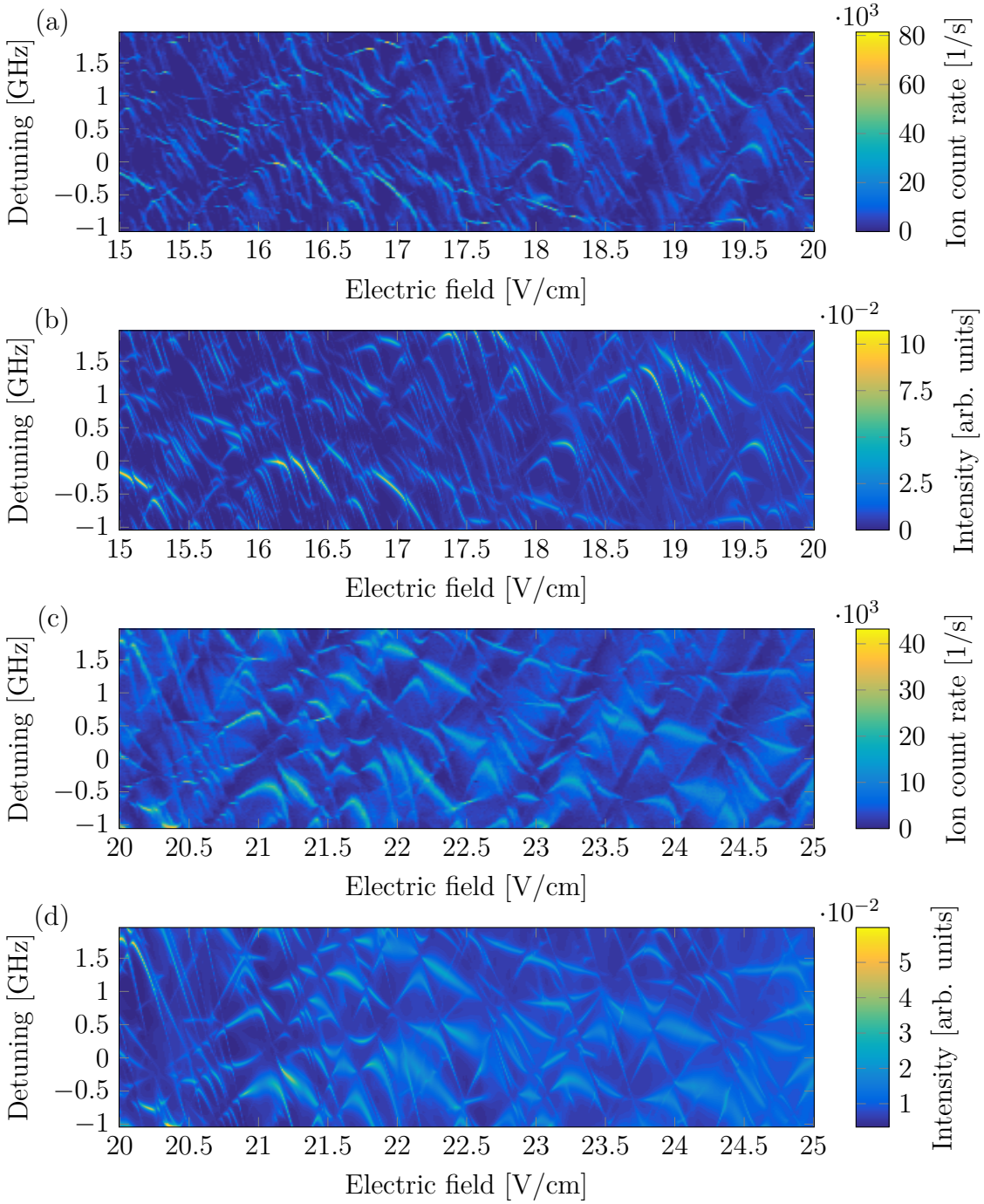

Figure 3.4.: Ionization Stark spectrum near $70S_{1/2}$. (a) and (c) show the detected ion signal from the experiment. (b) and (d) show the results from the numerical calculations for $\eta = 2 \cdot 10^5$. The detuning is given relative to the unperturbed state. We have applied a linear scaling to match the electric field from the experiment to the theoretical results. The classical ionization threshold is located at ≈16.1 V/cm. Figure and caption taken from [2] and adapted.

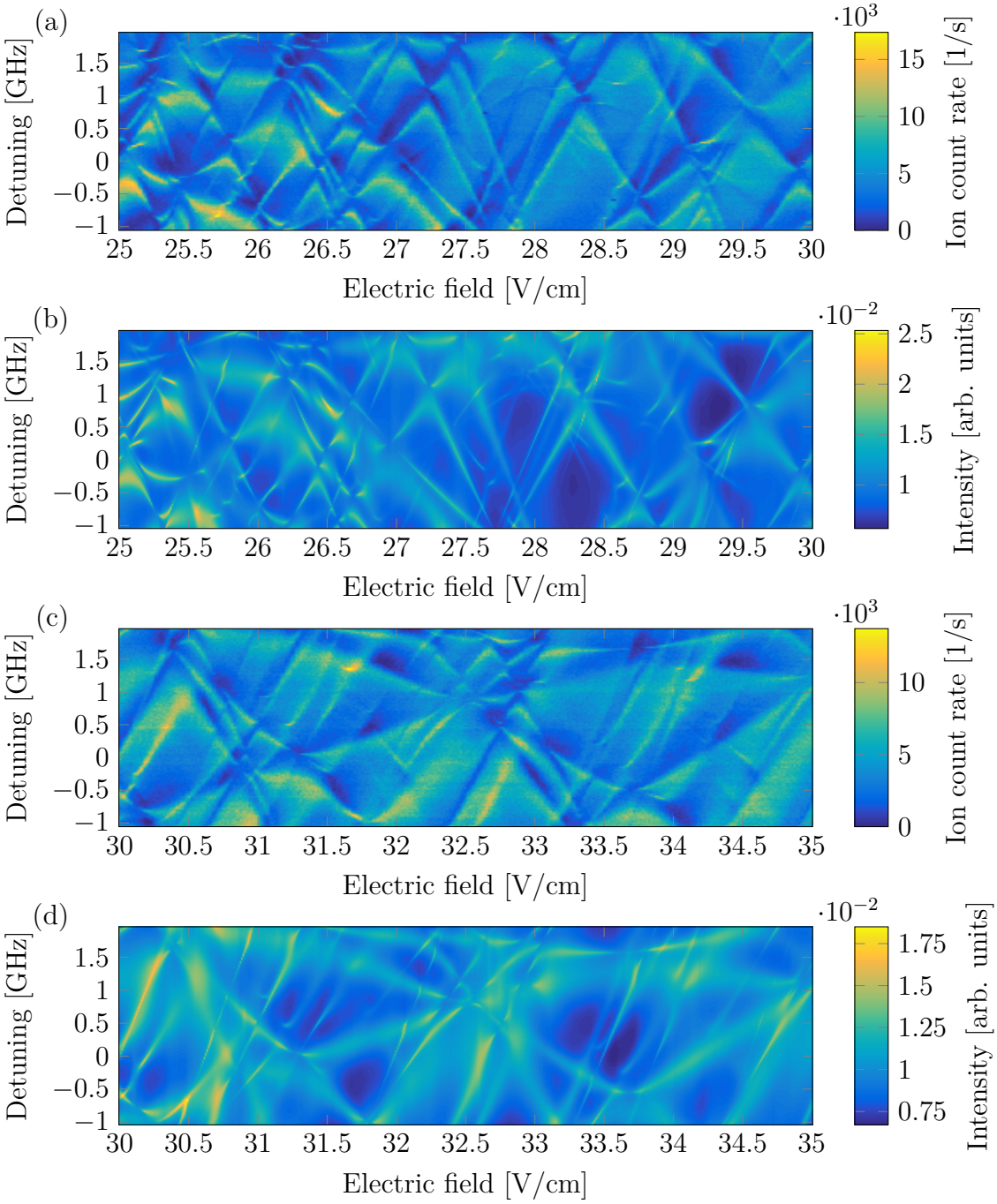

Figure 3.5.: Ionization Stark spectrum near $70S_{1/2}$. (a) and (c): Experiment, (b) and (d): Numerical calculation. Continuation from Fig. 3.4. Figure and caption taken from [2] and adapted.

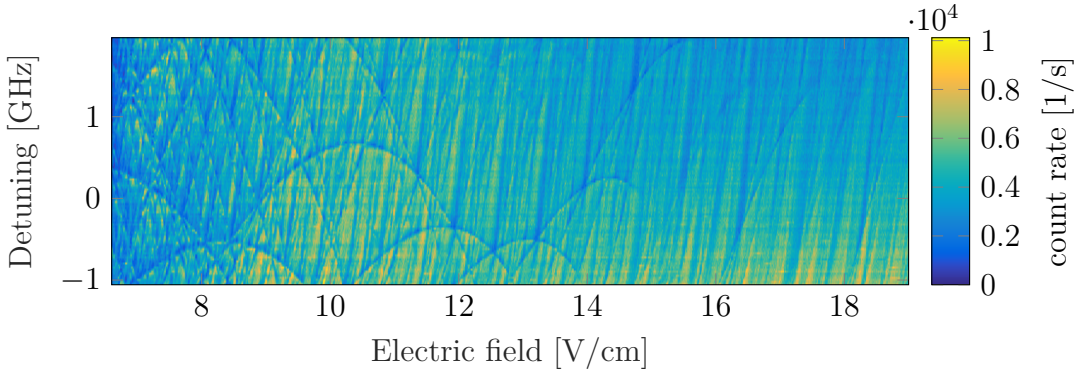

Figure 3.6.: Ionization Stark spectrum near $100S_{1/2}$. Depicted is the detected ion signal from the experiment. The detuning is given relative to the unperturbed state. The classical ionization threshold is located at ≈3.7 V/cm. A numerical calculation was attempted up to a basis size of 14000 states but did not converge. A larger basis would be necessary for convergence, which is however computationally very expensive and would lead to a high calculation time of several days per spectrum.

4. Selective field ionization

Selective field ionization (SFI) is a widely used tool for state selective detection of Rydberg atoms. Typically, the Rydberg atoms are excited at low or zero electric field and after the excitation pulse, a field ramp with a rise time on the order of nanoseconds to microseconds is applied in order to ionize the Rydberg population [42]. From the time resolved shape of the ion signal, inferences can be made about the initial state or state distribution. In general, the state with lower energy is ionized later (cf. Eq. 3.8) and thus a state change can be detected in a shift of the ionization peaks to earlier times in case of a change to a higher state or later times in case of a change to a lower state (assuming a monotonically increasing ramp). However, the zero field separation of the states does not necessarily translate linearly into a separation of the ionization peaks. When we have a look at a Stark map (e.g. Fig. 3.1), we immediately see that the evolution of an initial state at zero field can get very complicated when traversing through the intricate energy level structure governed by many avoided crossings. In general, the state will redistribute into many states depending on the slew rate and the splitting of the anticrossings. Furthermore, as already discussed in Sec. 3.2, the ionization rates of different Stark-shifted states can vary a lot and the simple picture of an onset of ionization at the classical ionization threshold does not hold for nonhydrogenic atoms.

4.1. Numerical calculation

The traversal through an avoided crossing of two states with energetic splitting $|V_{12}|$, initial populations $P_{1,2}$ and energies $E_{1,2}$ (see Fig. 4.1) can be described with the Landau-Zener theory [70]. In this model, the probability to evolve diabatically through the crossing is given by

$$D = \exp\left(-2\pi|V_{12}|^2 \Big/ \left|\frac{dE_1}{dt} - \frac{dE_2}{dt}\right|\right). \tag{4.1}$$

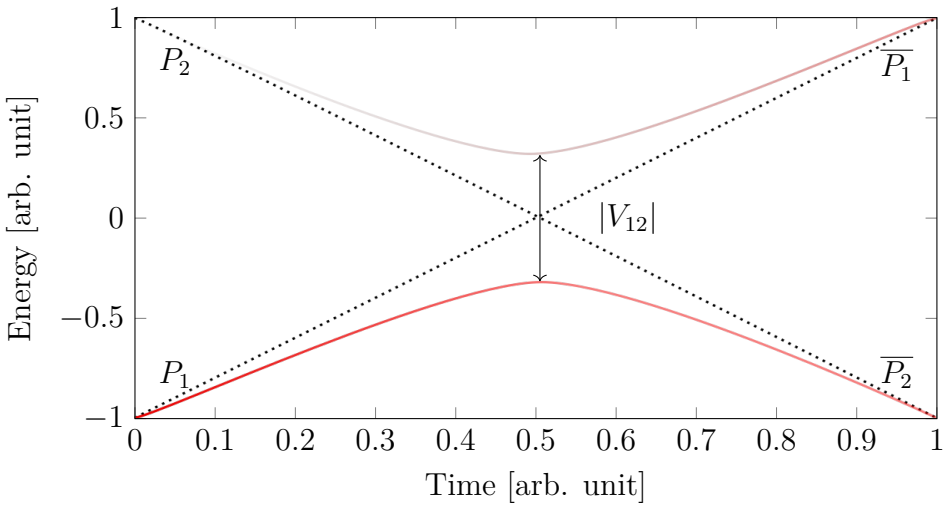

Figure 4.1.: Avoided crossing with energy splitting $|V_{12}|$, initial populations $P_{1,2}$ and final populations $\overline{P_{1,2}}$ after the evolution through the crossing (cf. Eqs. 4.1,4.2 and 4.3). The opacity of the resonance lines depict the population of the corresponding states. In this example, an initial population in P_1 evolves partly diabatically to $\overline{P_1}$ and partly adiabatically to $\overline{P_2}$.

The time derivative of the energy $dE_{1,2}/dt$ can be rewritten as $dE_{1,2}/dF \cdot dF/dt$ with the electric field F. As we can see, the diabatic probability is dependent on the slew rate of the electric field and the slope of the resonances. Thus, a diabatic traversal becomes more probable for avoided crossings with small energy separation as well as with a fast slew rate of the electric field ramp or large slope of the resonance lines. The populations $\overline{P}_{1,2}$ after traversing the avoided crossing are given by

$$\overline{P_1} = DP_1 + AP_2, \tag{4.2}$$

$$\overline{P_2} = DP_2 + AP_1, \tag{4.3}$$

with the adiabatic probability being $A = 1 - D$.

The Landau-Zener model is instructive but due to the large number of avoided crossings that have to be considered, it can be quite cumbersome to calculate selective field ionization dynamics with it. Furthermore, the model describes the evolution of the population but not the ionization process. Nevertheless, SFI dynamics of Li and Rb have been predicted by applying a multichannel Landau-Zener model [71]. The ionization process is included in the calculations by a semi-empirical formula for the ionization rate of hydrogen derived by Damburg and Kolosov [66]. Instead of using a Landau-Zener model, SFI dynamics have also been calculated with a fully

quantum-mechanical time evolution of the Schrödinger equation together with the Damburg-Kolosov model for ionization [72, 73].

In this work, we apply a quantum-mechanical time evolution of the CAP-Hamiltonian presented in Sec. 3.2, which automatically takes ionization into account. The time evolution of a system with Hamiltonian $\hat{H}$ can be described with the time evolution operator $U(t, t_0)$, which propagates an initial state $\Psi(t_0)$ from the time t_0 to t:

$$\Psi(t) = \hat{U}(t, t_0)\Psi(t_0). \tag{4.4}$$

In the case of a Hamiltonian that is not explicitly time dependent, there is an analytic solution in the form of a matrix exponential:

$$\hat{U}(t, t_0) = \exp\left(-\tfrac{i}{\hbar}\hat{H} \cdot (t - t_0)\right). \tag{4.5}$$

However, in our case, the Hamiltonian

$$\hat{H}(t) = \hat{H}_0 + F(t)\hat{z} - i\eta W(\hat{r}, F(t)) \tag{4.6}$$

is explicitly time dependent, since the electric field F(t) is changing over time. A numerical solution for the time evolution can be found by slicing the problem into small time steps τ. These steps have to be small enough for the Hamiltonian to be considered approximately time independent within the step. The propagator for one time step can then be calculated with the matrix exponential of $\hat{H}(t)$. There are different methods for the calculation, one is by diagonalization of $\hat{H}(t)$ to the matrix $\hat{D}(t)$ with the eigenvalues on its diagonal. The matrix exponential of a diagonal matrix can then be calculated trivially by exponentiation of the diagonal entries in $\hat{D}$; the transformation from the diagonal to the original basis is provided by a matrix S with the eigenvectors of $\hat{H}(t)$ in its columns:

$$\hat{U}(t + \tau, t) = \exp\left(-\tfrac{i}{\hbar}\hat{H}(t) \cdot \tau\right) = \hat{S} \exp\left(-\tfrac{i}{\hbar}\hat{D}(t) \cdot \tau\right) \hat{S}^{-1}. \tag{4.7}$$

The stepwise application of the propagator yields the time evolution of the initial state through the Stark map:

$$\Psi(t + \tau) = \hat{U}(t + \tau, t)\Psi(t). \tag{4.8}$$

The state $\Psi(t)$ is thereby represented in the unperturbed basis of $\hat{H}_0$. The ionization process modeled by the CAP can be seen in a decrease of the total population $N(t)$ over time:

$$N(t) = |\Psi(t)|^2. \tag{4.9}$$

The time derivative of the population

$$\dot{N}(t) = \frac{dN}{dt} \tag{4.10}$$

corresponds to the expected ion detection rate.

The calculation was implemented in MATLAB and since the number of time steps can be between 10^3 and 10^4 depending on the field ramp, it was optimized for speed with the help of parallelization and support of calculations on the GPU (graphics processing unit). In this way, the time evolution of a state from zero field to complete ionization can be achieved in a calculation time of around 10 h.

A typical field ramp when the extractor voltage is switched by a fast solid state switch has approximately the from

$$F(t) = F_\infty \cdot \left(1 - e^{-t/\tau}\right) + F_0. \tag{4.11}$$

F_∞ denotes the asymptotic value of the electric field, F_0 the electric field before switching and τ the exponential slew rate. In Fig. 4.2, the time evolution of the $45D_{5/2}, |m_j| = 0.5$ state with $F_\infty = 172\,\mathrm{V/cm}$, $\tau = 4\,\mu\mathrm{s}$ and $F_0 = 0$ is depicted. The form of the electric field ramp is plotted in Fig. 4.3. The initial state is distributed over several of the high angular momentum states crossing the D-state from above. The ionization happens mainly around the classical ionization limit but Fig. 4.3 shows, that the resulting ion signal exhibits a special form with several peaks. The detailed form of the signal is strongly depending on the field ramp, even small changes can alter the substructure quite severely as simulations with slightly different ramp forms have shown. The calculated ion signals for two neighboring states, 43F and 47P, which are 54 GHz above and below the 45D state, are also shown in Fig. 4.3. The data shows that the states can be clearly distinguished with the applied selective field ionization ramp. This will be used for the detection of Förster resonances (see Sec. 4.3).

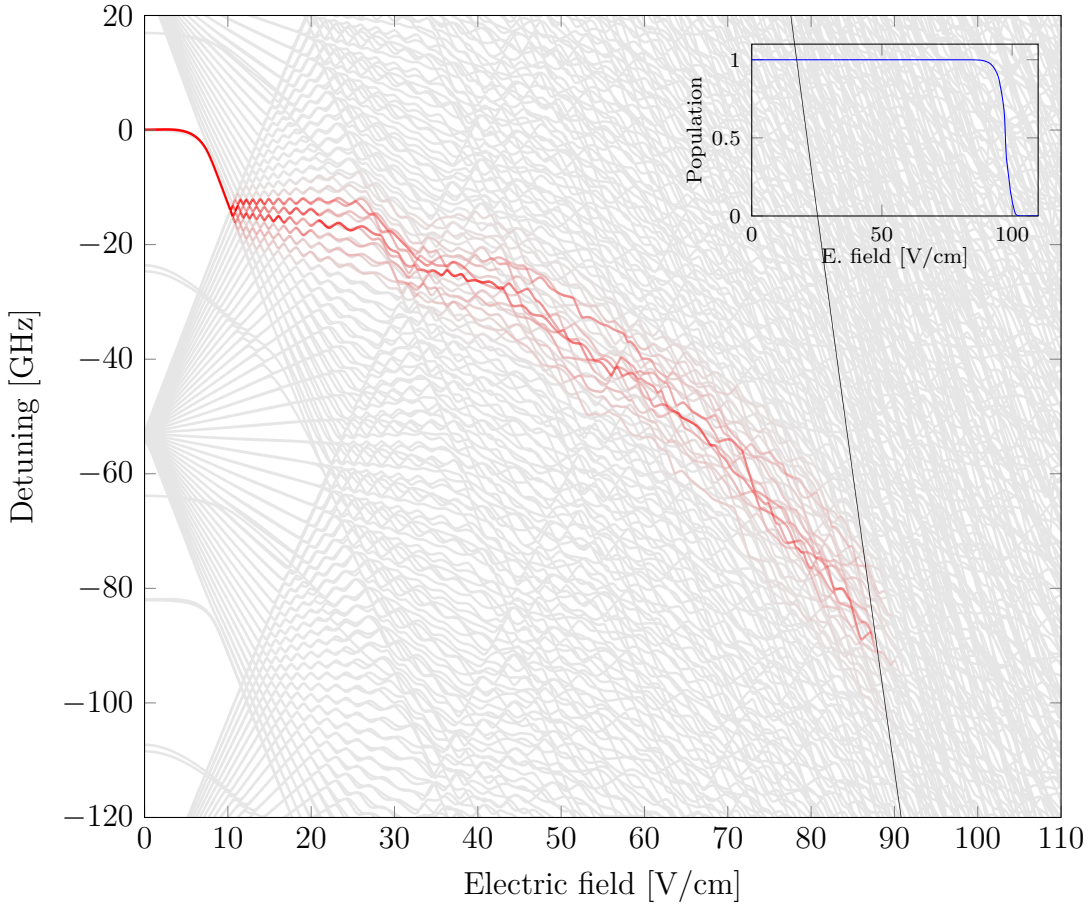

Figure 4.2.: Time evolution of state $45D_{5/2}, |m_j| = 0.5$. The opacity of the states is proportional to their population. A population of ≥ 0.7 corresponds to completely opaque (capped for better visibility), a population of 0 to completely transparent. The complete Stark map is depicted in light gray in the background (only states with $|m_j| = 0.5$). The black line depicts the classical ionization limit. The evolution of the population is shown in the inset. We see that an initially "clean" state gets redistributed over several states during the electric-field ramp through the Stark map due to a mixture of diabatic and adiabatic traversal of the many anticrossings (depending on the ramp speed, the energetic separation of the anticrossings and the slope of the resonance). Around the classical ionization limit, the states begin to ionize and the population vanishes.

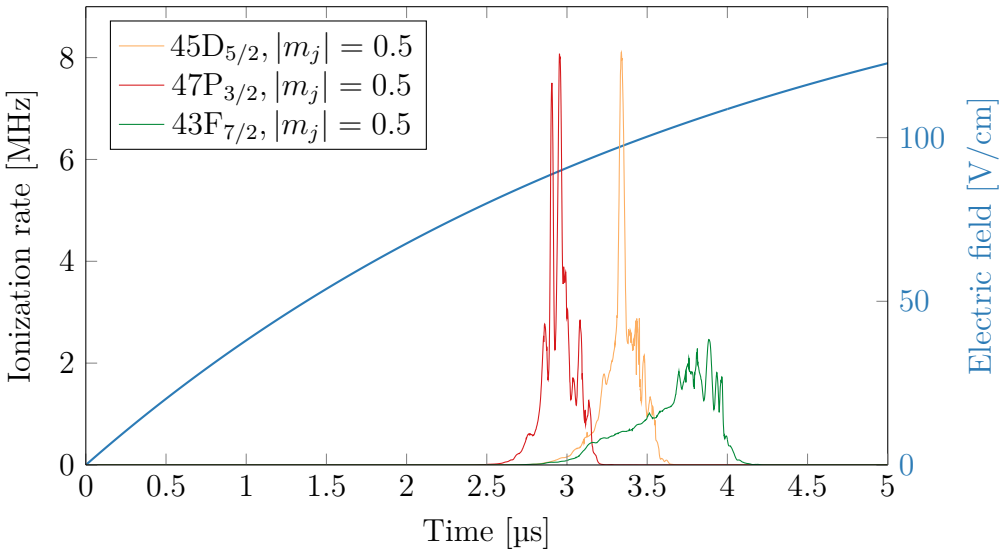

Figure 4.3.: Expected ion signal for the Rydberg states $45D_{5/2}$, $47P_{3/2}$ and $43F_{7/2}$. The electric field ramp is depicted in blue. For the sake of clarity, only the $|m_j| = 0.5$ substates are plotted. The ion signals for the other $|m_j|$ levels have a similar general form but differ in their substructure. This way, even the different $|m_j|$ levels of the same state can be distinguished via SFI.

4.2. Electric field calibration

The controlled excitation of Rydberg atoms requires a quantitative knowledge of the electric field at the position of the atoms. When simply switching both extractor electrodes to ground potential, the region between them is not field free because of stray fields from the other electrodes of the ion-optical system. This can be compensated partially by a small voltage at one or both of the extractor electrodes with an opposite sign with respect to the voltage for extraction. By measuring the spectrum of a Rydberg state, the electric field with respect to the compensation voltage can be determined by comparison with the theoretical calculations. As the polarizability of Rydberg atoms drastically increases with their principal quantum number, even small fields can be measured accurately by using a state with appropriately high n. When using a state with more than one $|m_j|$ sublevel, for example a D-state, the calibration can be done by evaluating the energy differences between the different $|m_j|$ levels which are degenerate only at zero field. This way, the result is only depending on the relative but not the absolute knowledge of the laser frequency.

In contrast to the continuous measurement of large parts of a Stark spectrum described in Chap. 3, the excitation and detection is now realized in a pulsed mode.

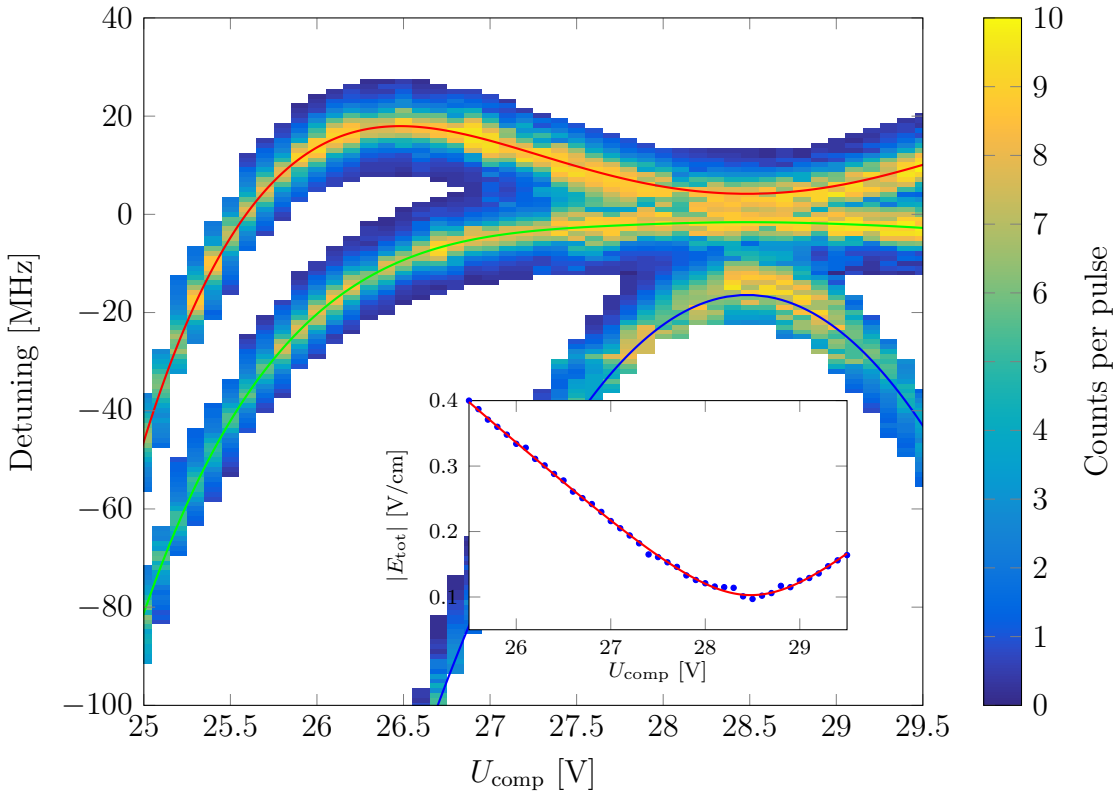

Figure 4.4.: Stark map of the $75D_{5/2}$ state. The colorplot shows the measurement. For each datapoint, the ion counts of 250 excitation pulses with 1 µs duration were averaged. The blue laser was focused to a light sheet (cf. Sec. 3.3) with a power of 1 mW and horizontal polarization (i.e. parallel to electric field). The lower transition between 5S and 5P was driven by a resonant beam with 2 mm $1/e^2$ diameter and 0.5 mW power counterpropagating to the blue beam. In the white areas, no data was taken as the measurement was restricted to the vicinity of the expected positions of the resonances. The solid lines depict the theory curves from a numerical calculation (see Sec. 3.1) with $|m_j| = 0.5$ in red, $|m_j| = 1.5$ in green and $|m_j| = 2.5$ in blue with a specific mapping of the total electric field to the compensation voltage U_{comp}. This mapping is shown in the inset. The datapoints in blue were determined by evaluating the frequency difference of the measured $|m_j| = 0.5$ and $|m_j| = 1.5$ resonances and determining the corresponding electric field from the results of the numerical calculation. The fit in red follows Eq. 4.12 yielding a residual field $E_\perp = 0.103\,\mathrm{V/cm}$ that cannot be compensated by U_{comp} and a field $E_\parallel = 3.67\,\mathrm{V/cm}$, which can be compensated by applying $U_{\mathrm{comp}} = 28.5\,\mathrm{V}$ to the negative extractor electrode.

This means that the Rydberg excitation laser is switched on only for typically 1-10 µs and thereafter the electric field is ramped up to values high enough to ionize the Rydberg population. The ions are then detected with the ion-optical system. This way, the Stark map for small electric fields, where the ionization rate of the Rydberg atoms is nearly zero, can be probed. In Fig. 4.4, we see the Stark shift of the $|75D_{5/2}\rangle$ state with respect to the compensation voltage U_{comp} applied to the negative extractor (the positive extractor is at 0 V). It is apparent that the Stark splitting and therefore the electric field is minimal for a compensation voltage of around 28.5 V. However, as the splitting is still >0, there is obviously a residual field $E_\perp$ that is perpendicular to the extractor field and thus cannot be compensated with the extractor. The total electric field at the position of the MOT can be written as

$$|E_{tot}| = \sqrt{(E_\parallel - \alpha U_{\mathrm{comp}})^2 + E_\perp^2}, \tag{4.12}$$

where $E_\parallel$ denotes the residual field that can be compensated by applying the compensation voltage U_{comp} to the extractor electrode and α the proportionality factor for the conversion from voltage to electric field. The result from this fit is depicted in the inset in Fig. 4.4. The residual fields are $E_\parallel = 3.67\,\mathrm{V/cm}$ and $E_\perp = 0.103\,\mathrm{V/cm}$. To compensate $E_\perp$, electrodes for the other spatial directions would be necessary. The proportionality factor is $\alpha = 0.129\,1/\mathrm{cm}$.

4.3. Förster resonances

Förster resonance energy transfer (FRET) is known as a nonradiative energy transfer between two light-sensitive molecules through dipole-dipole coupling [74] and can be observed for example in the light-harvesting complex of organisms performing photosynthesis. Similarly, in Rydberg physics a Förster resonance is defined as a resonant dipole-dipole interaction between two Rydberg pair states that become energetically degenerate. Typically, this degeneracy has to be induced externally for example by Stark shifting the energy levels with a small external electric field. In this way, the interaction strength between Rydberg atoms can be controlled and switched between a weak van der Waals to a strong resonant dipole-dipole type.

In most cases, one of the pair states consists of two Rydberg atoms of the same state, yet there are of course also interaction channels with different states in both

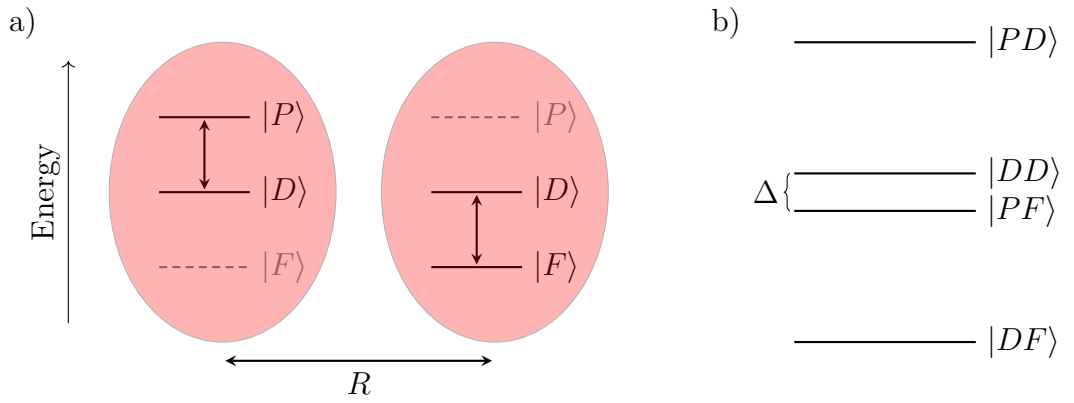

Figure 4.5.: Energy level diagram of (a) the bare states of two atoms separated by a distance R and (b) the corresponding pair states. The states are labeled with their orbital angular momentum in accordance to the resonance channel of Eq. 4.13. The energy defect Δ of the nearly degenerate pair states $|DD\rangle$ and $|PF\rangle$ corresponds to Eq. 4.14. A transition between these states can be realized by the exchange of virtual photons in the near field with transition $|D\rangle \leftrightarrow |P\rangle$ in the first atom and $|D\rangle \leftrightarrow |F\rangle$ in the second atom. Of course, the roles of the atoms could be exchanged. The pair states are dipole-dipole coupled and experience interactions (cf. Eq. 4.17). Transitions to the other pair states $|PD\rangle$, $|DF\rangle$, $|PP\rangle$ and $|FF\rangle$ are energetically forbidden.

pair states. One of the many possible interaction channels has the form

$$nD_{5/2} + nD_{5/2} \rightarrow (n+2)P_{3/2} + (n-2)F. \tag{4.13}$$

The F-state constitutes of two different angular momentum states ($j = 5/2, 7/2$) that can be involved in a resonance, but it is worth noting that j is not a good quantum number in the presence of an electric field anymore. The resonance channel can be characterized by its energy defect

$$\Delta = 2 \times E_{nD_{5/2}} - E_{(n+2)P_{3/2}} - E_{(n-2)F}. \tag{4.14}$$

The bare states and the possible pair states are depicted in Fig. 4.5. In contrast to the dipole-dipole interaction of Rydberg atoms with permanent electric dipole moment described in Chap. 5, at a Förster resonance, there is a resonant dipole-dipole interaction also resulting in a $1/R^3$ interaction but without a permanent dipole moment (the dipole moment resulting out of the small external electric field to tune the resonance is negligible). The coupling of the degenerate pair states $|DD\rangle$ and $|PF\rangle$ (following the abbreviated nomenclature of Fig. 4.5) is mediated by the exchange

of virtual photons in the near field. This means that the coupling is only possible when the separation of the atoms is much smaller than the transition wavelength [75]. For the interaction channel of Eq. 4.13, the transition is in the GHz regime (wavelength on the order of 1 cm); the typical density of our cold atomic sample is around $1 \cdot 10^{10}\,1/\mathrm{cm}^3$ (inter-particle distance on the order of 5 µm). When we compare these two length scales, we see that we are deep in the near field limit. In a classical picture, the coupling can be understood as a coupling of the field of the oscillating dipole of the transition $|D\rangle \leftrightarrow |P\rangle$ in the first atom to the oscillating dipole of the transition $|D\rangle \leftrightarrow |F\rangle$ in the second atom.

In a quantum-mechanical picture, the system can be described by a two-level Hamiltonian in the basis of the pair states $|DD\rangle$ and $|\widetilde{PF}\rangle = \frac{1}{\sqrt{2}}(|PF\rangle + |FP\rangle)$ (symmetrized version of the $|PF\rangle$ pair state as the roles of the first and second atom can be exchanged) with the interaction potential $U(R)$:

$$H = \begin{pmatrix} 0 & U(R) \\ U(R) & \Delta \end{pmatrix}, \tag{4.15}$$

The eigenvalues of the Hamiltonian are

$$\lambda_{1,2} = \frac{\Delta}{2} \pm \sqrt{\frac{\Delta^2}{4} + U^2(R)}. \tag{4.16}$$

In the case of $U \gg \Delta$, which includes the case of degeneracy with $\Delta \to 0$, the eigenvalues are $\lambda_{1,2} = \pm U(R)$. In the case of a large energy defect $\Delta \gg U$ compared to the interaction, the eigenvalues are $\lambda_1 = \Delta + U^2(R)/\Delta$ and $\lambda_2 = -U^2(R)/\Delta$.

The strength of the dipole-dipole interaction can be determined by evaluating

$$U(R) = \langle \widetilde{PF}|\, \hat{V}_{dd}\, |DD\rangle\,, \tag{4.17}$$

with the dipole-dipole interaction operator [43]

$$\hat{V}_{dd} = \frac{1}{4\pi\epsilon_0} \frac{\hat{d}_1 \cdot \hat{d}_2 - 3(\vec{n} \cdot \hat{d}_1)(\vec{n} \cdot \hat{d}_2)}{r^3}. \tag{4.18}$$

$\hat{d}_{1,2}$ denote the electric dipole moment operators for the two atoms and $\vec{n}$ the vector between the dipoles. In case of a Förster resonance, $\hat{d_{1,2}}$ are oscillating dipoles and their coupling is polarization dependent, which leads to an angular depenence of the interaction energy that does not necessarily resemble the classical case [76]. The

evaluation of Eq. 4.17 results in an interaction potential of the form [75]

$$U_{dd}(R) = \pm\frac{C_3}{R^3}. \tag{4.19}$$

Hence, following Eq. 4.16, at a Förster resonance the energy shift in dependence on the interatomic distance is of the form $1/R^3$ (resonant dipole-dipole interaction). Without degeneracy, the energy shift is of the form $1/R^6$ (van der Waals interaction). As the the interaction energy $U(R)$ increases with decreasing R, also in the non-degenerate case, the interaction eventually changes from van der Waals to resonant dipole-dipole for small distances (crossover distance $r_c = \sqrt[3]{C_3/\Delta}$). But in contrast to that, at a Förster resonance, the interaction is resonant dipole-dipole for all R.

In general, in the non-resonant van der Waals case, several pair states have to be taken into account. The interaction can be calculated from second order perturbation theory [43]:

$$U_{vdW}(R) = -\sum_{i',i''} \frac{|\langle i'i''|\hat{V}_{dd}|ii\rangle|^2}{\Delta_{i',i''}}. \tag{4.20}$$

$\Delta_{i',i''}$ denotes the energy defect between the initial pair state $|ii\rangle$ and the pair state $|i'i''\rangle$ that is dipole coupled to it. The resulting interaction potential is of van der Waals form:

$$U_{vdW}(R) = -\frac{C_6}{R^6}. \tag{4.21}$$

As mentioned before, the energy defect Δ between the pair states $|DD\rangle$ and $|PF\rangle$ is in general nonzero but can be shifted into resonance by an external electric field. When applying a small electric field, all states get Stark shifted but the dominant contribution comes from the F-state (see Fig. 4.6), which gets shifted to lower energies thus decreasing the energy of the pair state $|PF\rangle$. For $n \leq 43$, the energy defect Δ at zero electric field is positive, hence the interaction cannot be tuned into resonance by an electric field. At $n = 43$, the interaction channel is near resonant at zero electric field with $\Delta = 2\pi \times 6.5\,\mathrm{MHz}$. In this case, an external electric field tunes the channel out of resonance as observed in [77]. For $n > 43$, at zero field the defect is negative so the interaction channel can be tuned to exact resonance by an external electric field. The dipole-dipole coupling strength for $n > 48$ decreases rapidly as the mixing of the F-state with high-l states becomes stronger even in small electric fields [43]. Therefore, in the region $n = 44 - 48$, we expect strong Förster resonances at electric fields of around $0.2\,\mathrm{V/cm}$.

The occurrence of a Förster resonance can be measured by selective field ionization

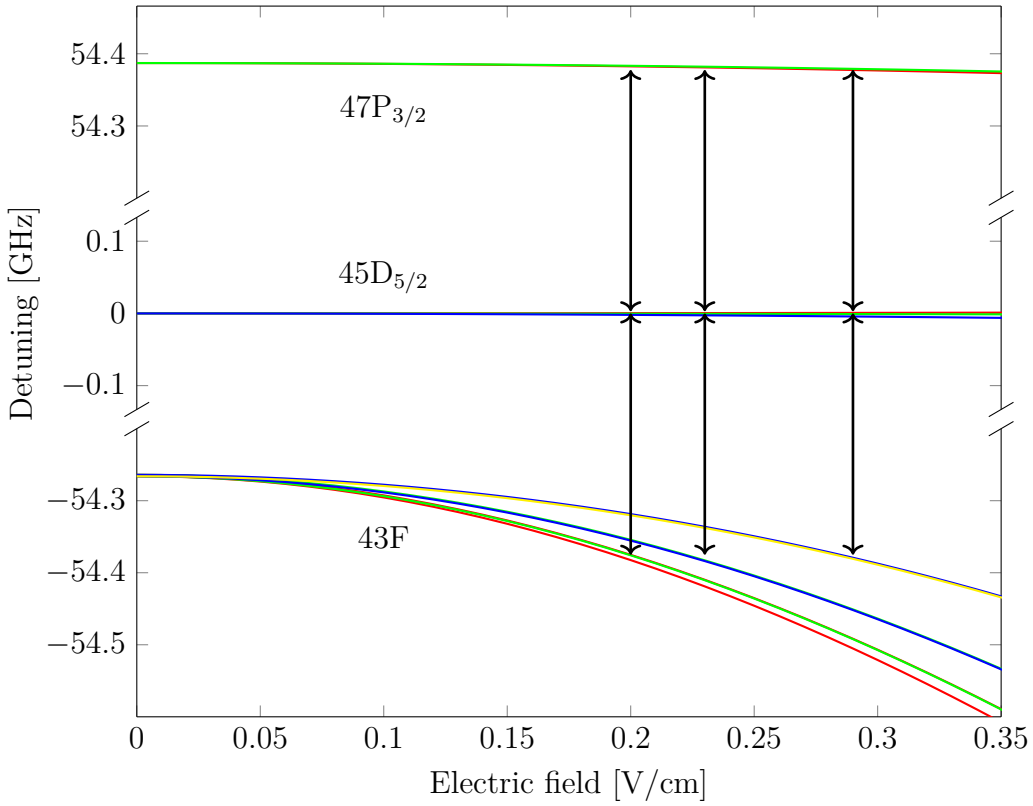

Figure 4.6.: Stark map of the states involved in the Förster resonances described in Eq. 4.22 (all other states were omitted for this plot), with $|m_j| = 0.5$ in red, $|m_j| = 1.5$ in green, $|m_j| = 2.5$ in blue and $|m_j| = 3.5$ in yellow. The vertical arrows depict the resonant transitions with zero energy defect.

as the different states in Eq. 4.13 will have different ion signatures (cf. Fig. 4.3). In our measurements, we used the interaction channel

$$45D_{5/2} + 45D_{5/2} \rightarrow 47P_{3/2} + 43F. \tag{4.22}$$

The Stark map for these states with the corresponding Förster transitions is depicted in Fig. 4.6. All the states have several sublevels that can be involved in a resonance and all the states have different Stark shifts. Consequently, we expect several resonances at slightly different electric fields. The dipole allowed transitions form three groups around 0.20 V/cm, 0.23 V/cm and 0.29 V/cm.

To measure the occurrence of a Förster resonance, the initial electric field is set according to the field calibration presented in Sec. 4.2 and the initial $45D_{5/2}$ Rydberg state is excited by a pulsed two photon excitation (see Sec. 2.1) and detected via selective field ionization. The blue laser is focused to a light sheet (cf. Sec. 3.3) with a power of 0.5 mW and horizontal polarization (i.e. parallel to the electric field). The transition between 5S and 5P is driven by a laser beam that is 133 MHz blue detuned from resonance (2 mm $1/e^2$ diameter, 0.5 mW power, counterpropagating to the blue beam). The excitation pulse length is 2 µs. For selective field ionization, the extractor voltage is ramped up within several microseconds (the ramp parameters are equal to the ones used in Sec. 4.1). At a Förster resonance, a population transfer to 47P and 43F should be visible in the SFI signal. The two pair states are coupled by the dipole-dipole interaction as described in the Hamiltonian of Eq. 4.15, so the population should show Rabi oscillations [78]. However, the Rabi frequency is depending on the interaction strength and thereby on the distance between the atoms. As our sample is a thermal gas, many different distances with different Rabi frequencies are realized, so we do not observe Rabi oscillations but we can measure the steady-state distribution of the pair states via SFI. In Fig. 4.7, the SFI signals for two different initial electric field values are plotted. There is a clear change in the SFI signal from a single peak to three peaks. The SFI signal was also numerically calculated following Sec. 4.1 for all the states that participate in the Förster resonance (including the different $|m_j|$ substates). A linear combination of the resulting SFI spectra

$$\begin{aligned} S_{\text{tot}} = a \cdot S(45D_{5/2}, m_j = 0.5) + b \cdot S(45D_{5/2}, m_j = 1.5) \\ + c \cdot S(45D_{5/2}, m_j = 2.5) + d \cdot S(47P_{3/2}, m_j = 0.5) + ... \end{aligned} \tag{4.23}$$

was then fitted to the measured data with $a, b, c, ...$ as fit parameters and is plotted as a red dashed line in Fig. 4.7. The time axis of the calculated signal is shifted by 7 µs compared to the results shown in Fig. 4.3a because of the ion's time of flight of around 12 µs less a trigger delay of 5 µs. We see that the observed signal fits nicely to the theory. Even the substructure can be partly reproduced, however some subpeaks seem to be somewhat shifted. Most probably, this is due to a slight change of the time of flight during the field ramp because of the changing extraction field.

In Fig. 4.8, the SFI signal for a range of initial electric fields is depicted in a colorplot together with the numerical calculations fitted to each field value. In Fig. 4.9, the corresponding fit parameters are plotted. As we could already see in Fig. 4.7, the theory shows good agreement to the measurement. As expected, at three different field regions we can see the Förster transition becoming resonant. Compared to the field values mentioned above, there is a slight shift to lower fields by around 0.04 V/cm. This shift most likely comes from residual magnetic fields. The earth magnetic field is not compensated in the experiment and the MOT coils are not switched off during the excitation of the Rydberg atoms.

As aforementioned, when a Förster interaction channel is tuned into resonance, the Rydberg-Rydberg interaction gets much stronger and changes from van der Waals ($\sim 1/R^6$ with interatomic distance R) to dipole-dipole type ($\sim 1/R^3$). The stronger interaction results in a stronger Rydberg blockade. The blockade manifests itself in a sub-Poissonian excitation number distribution, as predicted theoretically in [79, 80] and demonstrated experimentally in [81]. The excitation number statistics can be analyzed with the help of the Mandel Q parameter [82], which is defined by

$$Q = \frac{\langle (\Delta N)^2 \rangle - \langle N \rangle}{\langle N \rangle} = \frac{\langle N^2 \rangle - \langle N \rangle^2}{\langle N \rangle} - 1, \tag{4.24}$$

where N denotes the number of detected excitations after each excitation pulse, $\langle ... \rangle$ the mean value and $\Delta N = N - \langle N \rangle$. Values of $Q > 0$ correspond to super-Poissonian, $Q = 0$ to Poissonian and $Q < 0$ to sub-Poissonian excitation statistics. In Fig. 4.10, we can see the Q-parameter for the different electric fields of the measurement depicted in red. For orientation, the right hand side y-axis together with the blue line depicts the relative 45D population, which shows a decrease at the Förster resonances. As expected, the Q parameter also shows a decrease when the Förster interaction channel is tuned into resonance.

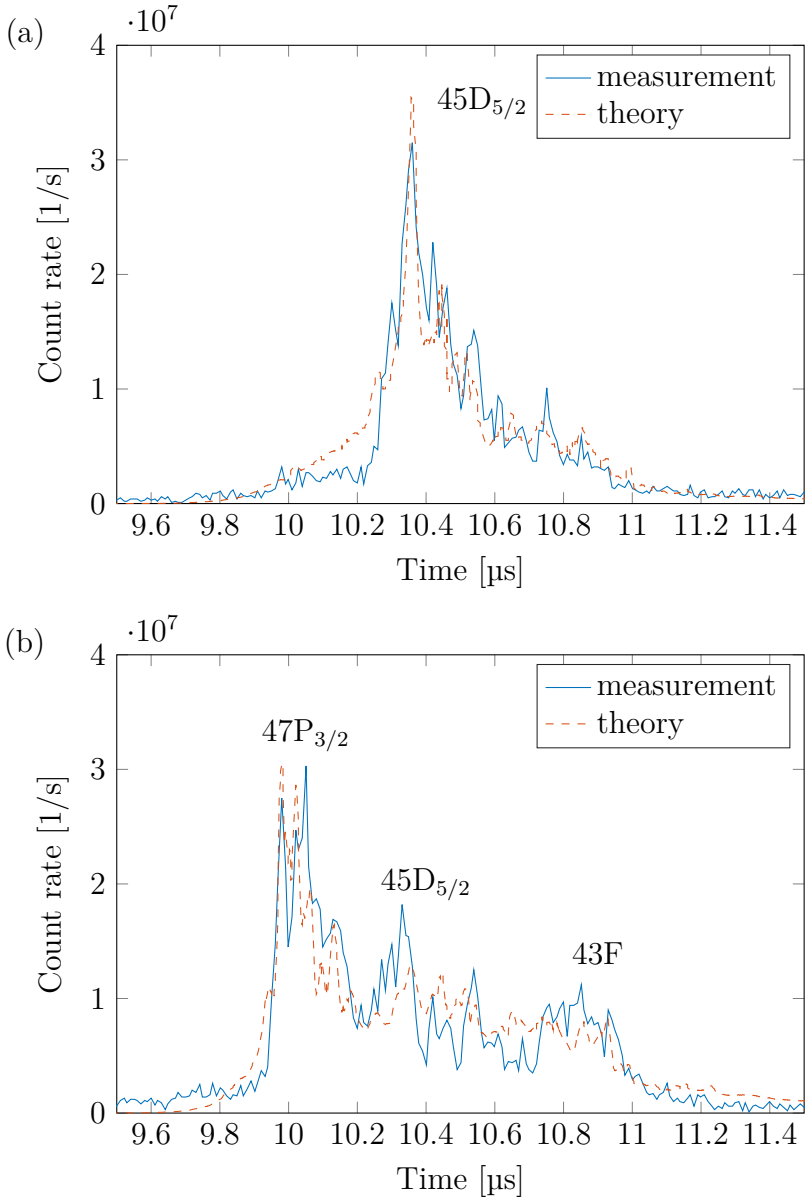

Figure 4.7.: SFI signal for two different initial electric field values far away from a Förster resonance (a, $F = 0.108\,\mathrm{V/cm}$) and on resonance (b, $F = 0.161\,\mathrm{V/cm}$). The measurements are depicted with blue solid lines. The red dashed lines correspond to the numerical calculation of the time evolution of the involved states. The time evolution was calculated according to Sec. 4.1 and a linear combination of the resulting SFI spectra was fitted to the measurement. The histogram of the measurement has a temporal binning of 10 ns. The peak around 10.4 µs corresponds to the 45D state. At the Förster resonance, the SFI signal shows a clear redistribution to two peaks around 10 µs (47P) and 10.9 µs (43F).

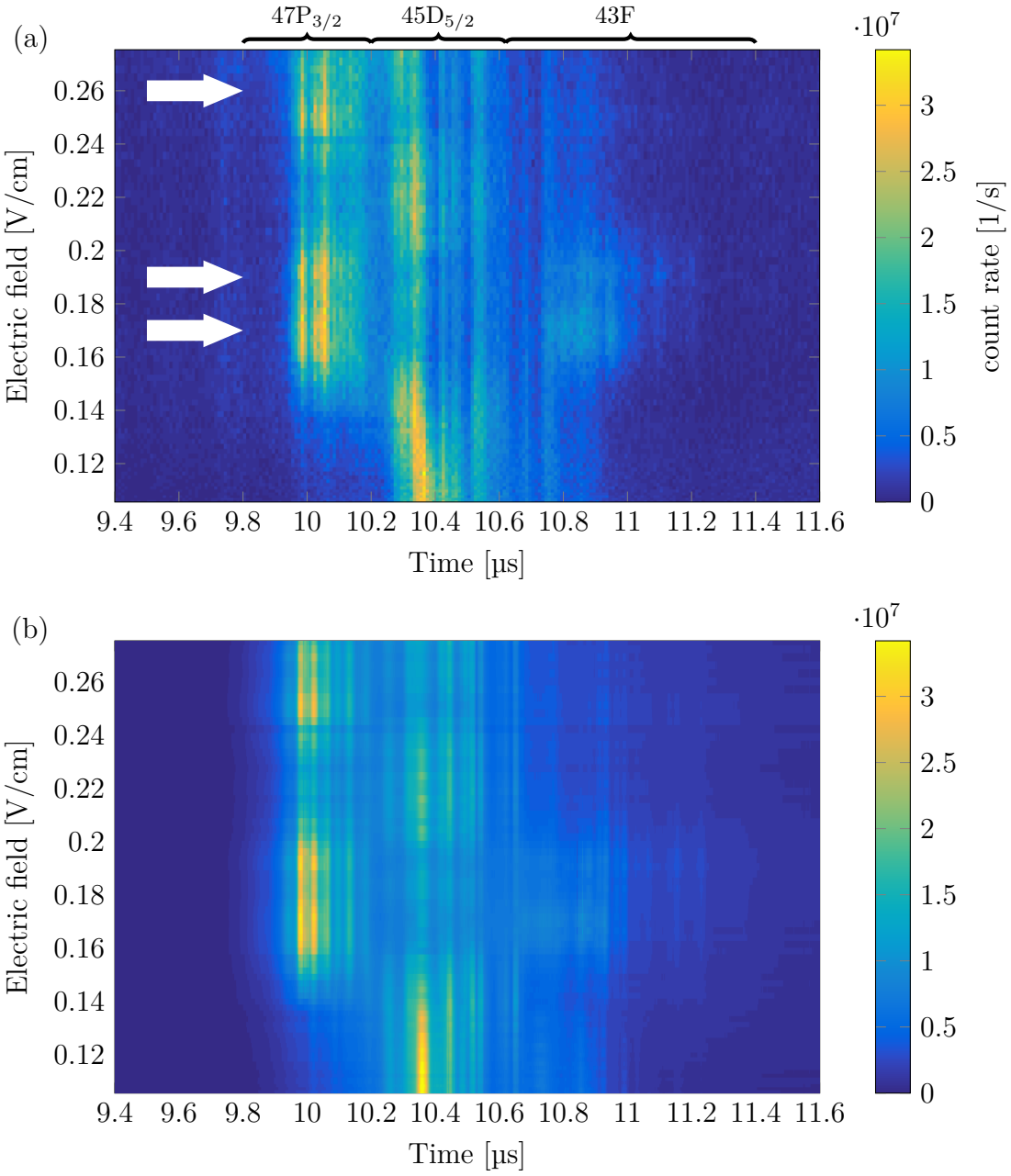

Figure 4.8.: (a) Histogram of the arrival times of the ions after a selective field ionization ramp for different initial electric fields at the position of the MOT (binning of 10 ns). The ramp has the same form and parameters as described in Sec. 4.1. The braces on top depict the estimated arrival times for the different states involved in the Förster resonance channel of Eq. 4.22. When this channel becomes resonant, a state change can be observed in the SFI signal (around 0.17 V/cm, 0.19 V/cm and 0.26 V/cm, marked in the plot with thick arrows). (b) Numerical calculation of the time evolution of the involved states. The time evolution was calculated according to Sec. 4.1 and a linear combination of the resulting SFI spectra was fitted to the the measured SFI signal for each field value (fit parameters depicted in Fig. 4.9).

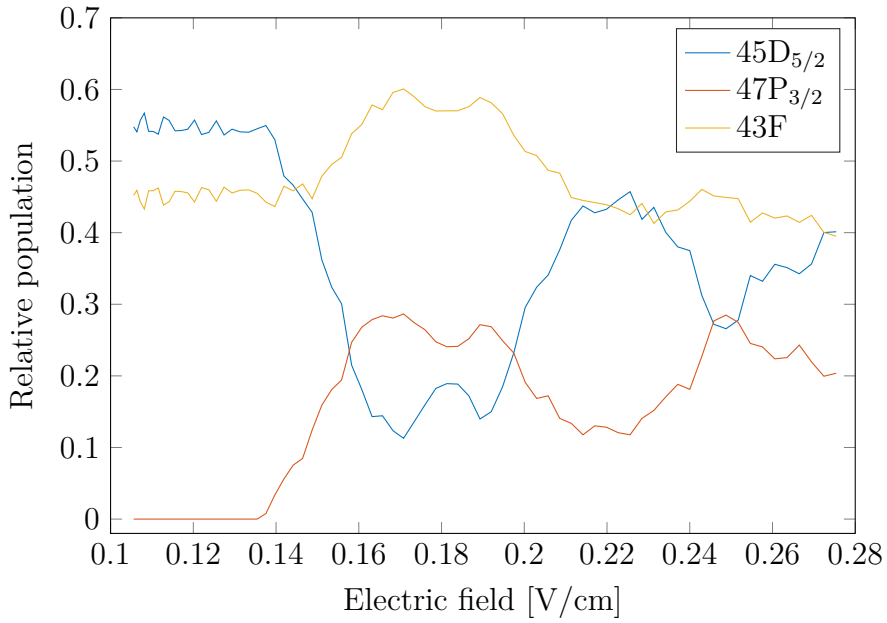

Figure 4.9.: Normalized fit parameters corresponding to the fit of the calculated SFI spectra to the measurement depicted in Fig. 4.8. The contributions of the $|m_j|$ substates were summed up for the plot. As expected, at a Förster resonance an increase of the relative population of the states $47P_{3/2}$ and 43F together with a decrease of the population of $45D_{5/2}$ is visible. While the population of the $47P_{3/2}$ state is zero far away from the Förster resonance, there is a constant background in 43F population. This might partly be an artifact of the fitting but it is also likely that part of the initial $45D_{5/2}$ population decays to lower lying states before detection.

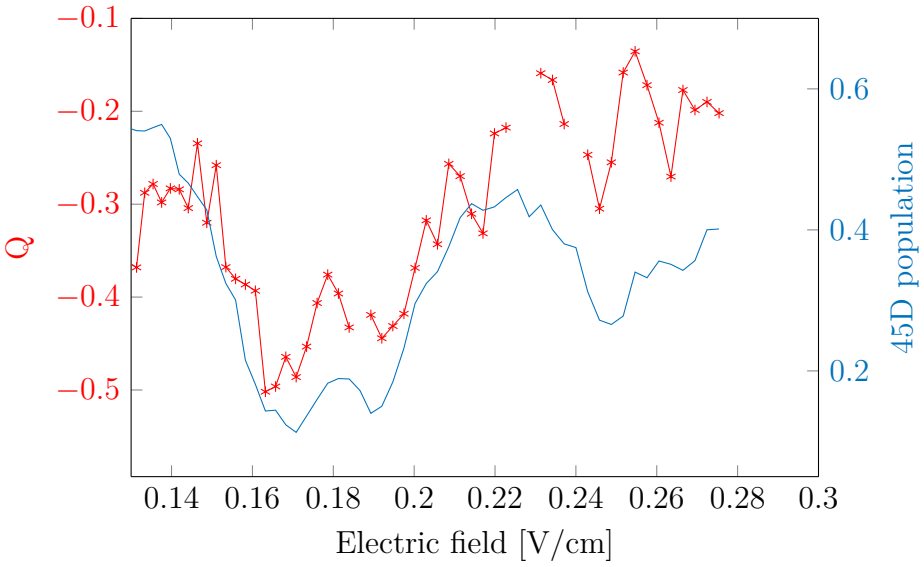

Figure 4.10.: Left y-axis with red dots: Mandel Q parameter for different inital electric fields (1000 excitation-detection pulses for each point, four data points are missing because the measurement was disturbed at these points). Right y-axis with blue line: relative population of the 45D state. A decrease of Q and the 45D population is visible when the Förster interaction channel is tuned into resonance by the electric field.

4.4. Detector limitations

In case of the SFI measurements presented above, only the temporal resolution of our ion detector was used. For the spatial imaging of Rydberg excitations in zero or low electric fields, the extraction field has to be switched on as fast as possible (in our case $< 50\,\mathrm{ns}$) to ensure imaging by our ion-optical systems with a fixed magnification factor. The extraction field has to lie above the classical ionization threshold to ensure rapid ionization. Typically, a voltage of $\pm 500\,\mathrm{V}$ is applied to the extractors, which corresponds to an electric field of $157\,\mathrm{V/cm}$. That means that states with $n > 41$ can be used with this extraction field (the classical ionization threshold of $41S_{1/2}$ is $156.3\,\mathrm{V/cm}$). A fast switching of the extraction field with a transition time of several nanoseconds can be achieved with high voltage transistor switches[1]. When we look at the histogram of the arrival times of the ions after such a fast switching (Fig. 4.11), we see several separate peaks. While the first one contains the ions with correct positions that were created in the object plane of the microscope, the rest of the ion signal comes from ions that are created outside of the object plane. Due to the characteristics of our ion microscope, the trajectories of some of the ions created outside of the object plane can be bent back onto the detector plane. These ions do not carry a suitable position information. As the different peaks in the histogram are clearly distinct, the arrival time can be used to filter for the correct ion signal.

Nevertheless, a problem arises with this kind of detection with a fast switching of the extractor voltage because several ions are produced in a very short amount of time, which can lead to a saturation of the ion detector or a loss of spatial resolution. A general saturation is connected to the dead time of our detector[2] and the signal width of the delay line (1-2 ns), as overlapping signals cannot be distinguished as separate events. Besides this, low temporal separation of the ion events also limits the functionality of the delay line anode: the position is encoded by the difference of the signal arrival times at the two ends of the delay line (two separate layers for x and y position). The propagation speed is $0.75\,\mathrm{ns/mm}$, meaning that for our detector of 40 mm diameter, the two signals at the ends of the delay line of a single event can have a time separation of up to 30 ns. If two or more ion events arrive with a small but separable time difference, depending on the position, the delay line signal of the second ion can arrive before the first one on the one end of the delay line and the

[1] Behlke HTS 61-03-GSM

[2] The manufacturer of our MCP states for the Time-to-Digital-Converter a typical dead time between multiple hits on one channel of 5 ns and an overall multi-hit dead time of 10-20 ns.

other way around on the other end. This can cause an incorrect conversion from time signal to position information thus causing a loss in spatial resolution even if the number of detected particles is not saturated in the sense of the time separation being smaller than the width of the signal peaks.

In summary, if only the MCP is used (no spatial resolution), the time separation of two events should be >5 ns, corresponding to an ion count rate up to 200 MHz. If the delay line detector is used, this limit changes to >30 ns, corresponding to an ion count rate up to 33 MHz. These count rate limits are only valid for a very small amount of particles. The continuous count rate should not exceed 1 MHz, otherwise the MCP can be permanently damaged.

In Fig. 4.12, the loss of resolution can be seen as a broadening of the spatial structure imprinted onto the MOT. The problem can be circumvented by greatly reducing the excitation power so that on average less than one Rydberg atom is excited inside the detection region. However, the detection of multiple particles is essential for measuring two-body or many-body physics like the Rydberg blockade. With the spatial detection method we developed in order to be able to measure the blockade effect for highly Stark-shifted Rydberg states (see Chap. 5), the ionization rate of the atoms can be precisely controlled, therefore avoiding detector saturation and loss of spatial resolution. Furthermore, as the electric field is changed only by a small amount in order to ionize the atoms, the magnification factor remains nearly constant.

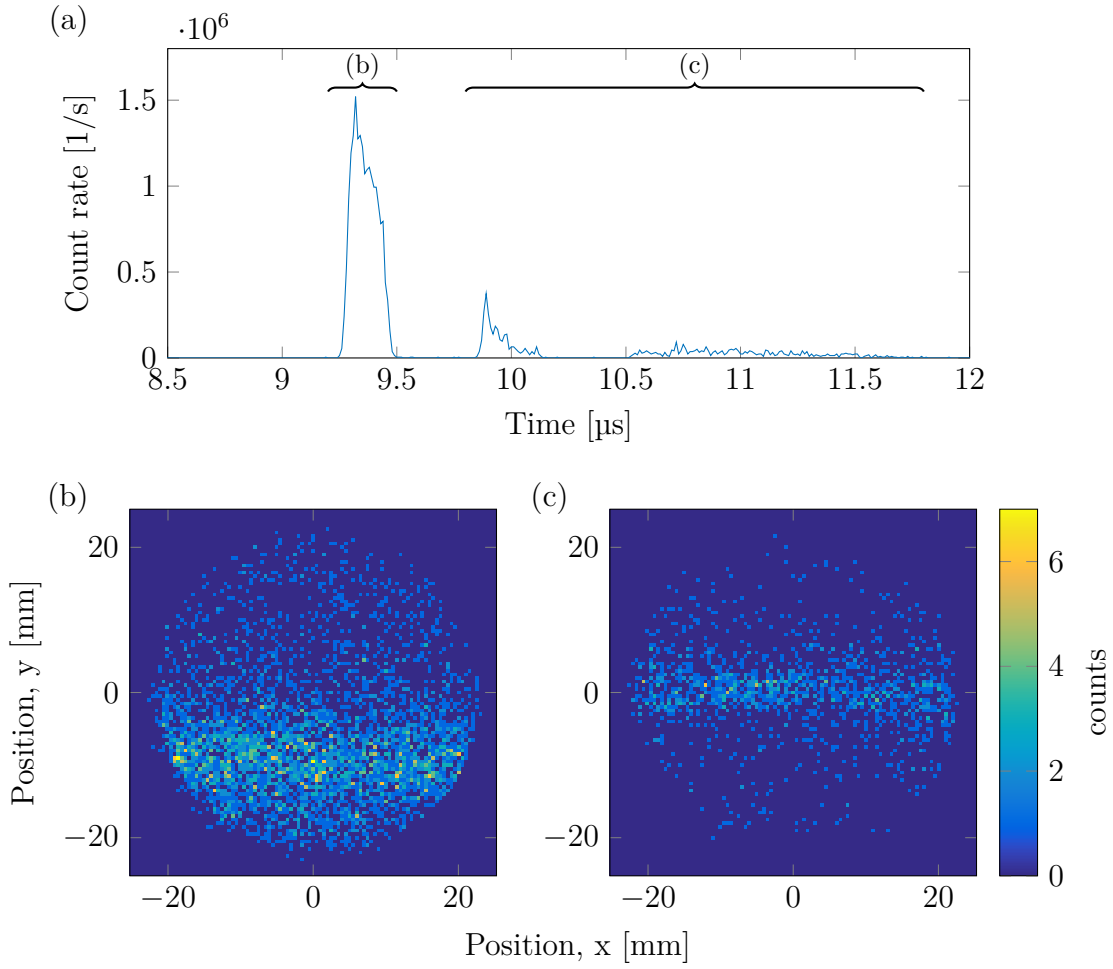

Figure 4.11.: Excitation of 43S Rydberg atoms at zero field with 5 µs pulse length. The magnification of the ion microscope was set to 1000. 1 µs after the excitation pulse, the extractor voltages are ramped up in 30 ns from zero or the compensation voltage to their final values. (a) Histogram of the arrival times of ions out of 21635 pulses (0.3 events per pulse on average, 10 ns bin size). (b) and (c): Positions of the ions corresponding to the regions marked with the braces in the histogram. The original excitation area (a line of 10 µm width, shifted to the lower part of the detection area) is reproduced in figure (b). In contrast to that, the strip in figure (c) always stays in the middle of the detection area irrespective of the position of the excitation line.

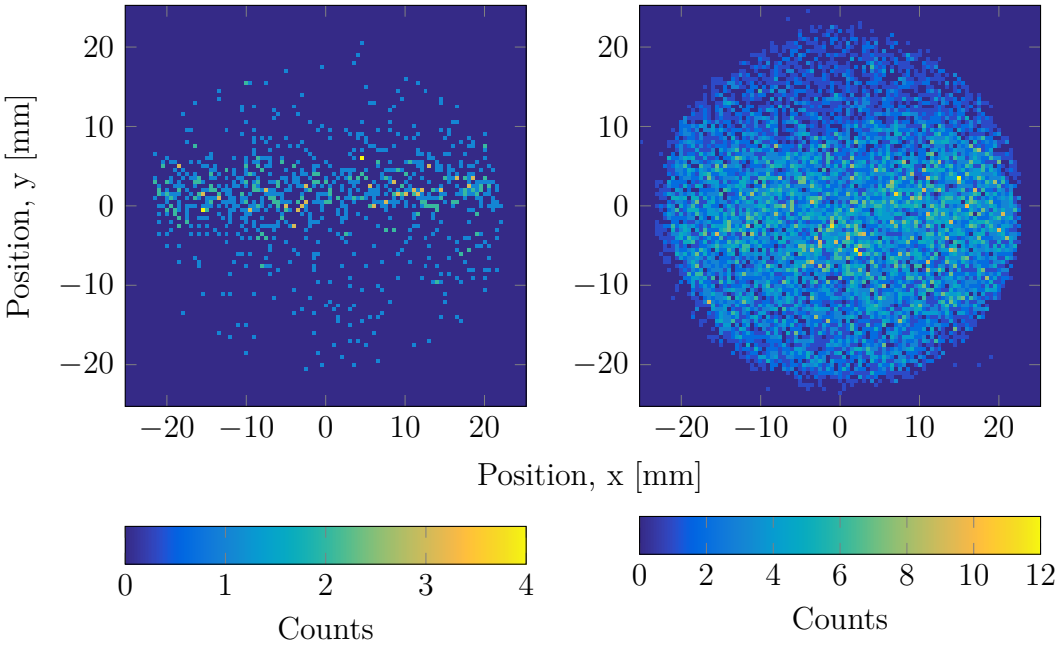

Figure 4.12.: Ion signal for different excitation laser powers (pulse length 1 µs) that result in 0.1 detected ion hits per pulse on average (left) and 1.3 hits per pulse, respectively (11354 pulses in total). In the second case, it is likely that the real number of events is higher but could not be resolved by the detector. The excitation area was a line of 6 µm width. The magnification was set to 1000. With the very low count rates in the left plot, the form is reproduced correctly, while for higher count rates in the right plot, the spatial resolution is lost.

5. Control of dipole blockade in high electric fields

The Rydberg blockade is observed conventionally in the zero electric field regime, where Rydberg states do not carry a permanent electric dipole moment. Thus, the interaction between the atoms is of second order van der Waals type $-C_6/r^6$ with the interatomic dinstance r. The magnitude of the interaction scales with n^{11} (with n being the principal quantum number of the state). A change in interaction strength and with that a change in the blockade radius is only possible by changing the excited Rydberg state. An increased interaction strength is for example desirable in order to enhance the fidelity of a blockade-based quantum gate or to obtain a tunable interaction potential for quantum simulators [83]. For this reason, different approaches to enhance and tune the interaction have been studied. At zero electric field, the interaction is of van der Waals type and its magnitude can be calculated with second order perturbation theory (see also Sec. 4.3):

$$U_{vdW}(R) = -\sum_{i',i''} \frac{|\langle i'i''|\hat{V}_{dd}|ii\rangle|^2}{\Delta_{i',i''}}. \tag{5.1}$$

Depending on the angular momentum of the state, the n^{11} scaling can be interrupted by a near resonant interaction channel, where the energy defect $\Delta_{i',i''}$ between the initial pair state $|ii\rangle$ and another dipole-dipole coupled pair state $|i'i''\rangle$ tends to zero. The interaction is then resonantly enhanced and the interaction type changes from second order van der Waals to first order dipole-dipole type $-C_3/r^3$. While for $n\mathrm{S}_{1/2}$ states of rubidium, there is no such resonant channel, for $n\mathrm{D}_{5/2}$ states a near resonant channel is present for $n = 43$ ($|43D_{5/2}, 43D_{5/2}\rangle \rightarrow |41F_{7/2}, 45P_{3/2}\rangle$) [43]. A small external electric field can be applied to tune the interaction out of resonance again and by that diminish the interaction strength [77, 84]. However, it is worth noting that despite the enhanced interaction strength, the Zeeman degeneracies of the states at zero external field can still lead to poor blockade characteristics [83, 85]. Similar

to that, a Förster resonance (see Sec. 4.3) can be tuned into resonance by a small electric field [51, 77, 81] and by that the interaction strength is increased. Instead of using a DC Stark shift to tune the interaction channel in and out of resonance, the same can also be achieved by the AC Stark effect of a microwave dressing field [86].

In the presence of an external electric field but without a resonantly enhanced interaction channel, the dipole-dipole interaction energy scales quadratically with the dipole moment p_z [43]:

$$\Delta W = \frac{1}{4\pi\epsilon_0}\frac{p_z^2}{R^3}\left(1 - 3\cos^2\Theta\right). \tag{5.2}$$

Here, the electric field is oriented in z-direction, R denotes the interatomic distance and Θ the angle between R and the z-axis. In an external electric field F, the dipole moment p_z of a Stark-shifted state with energy $E(F)$ is given by the slope of the resonance line $-dE(F)/dF$ (in SI units). Therefore, the interaction can be tuned by using states with different slopes as has been shown in [51] for Cs Rydberg P states with principal quantum numbers between 60 and 85 and electric fields up to 0.4 V/cm. A recent work uses Rb Rydberg atoms near the unperturbed 50S state, which are excited in a small electric field around 2.8 V/cm [52, 87]. In this field region, there is an anticrossing between a nonpolar and a highly dipolar state. Atoms are excited to the nonpolar Rydberg state and then adiabatically transfered to the highly dipolar state, which dramatically changes the magnitude of the Rydberg-Rydberg interaction. Compared to the classical ionization threshold (see Eq. 3.8), the electric field used in the experiments presented above is small. For the 50S state of Rb, the ionization threshold is 66.6 V/cm and for 60P and 85P of Cs, it is 31.7 V/cm and 7.3 V/cm, respectively.

5.1. Ionization rates in high electric fields

As shown in Sec. 3.2, around and above the classical ionization limit, the Stark spectrum of Rydberg atoms has an intricate form and is dominated by strongly varying line broadening due to ionization. While the measurements of [2] focus on calculating and measuring complete spectra, here we want to focus on the ionization behavior of individual resonance lines in the highly Stark shifted regime around the ionization threshold. In Fig. 5.1, a small part of the numerically calculated Stark spectrum around the unperturbed $43S_{1/2}$ state is depicted. The classical ionization

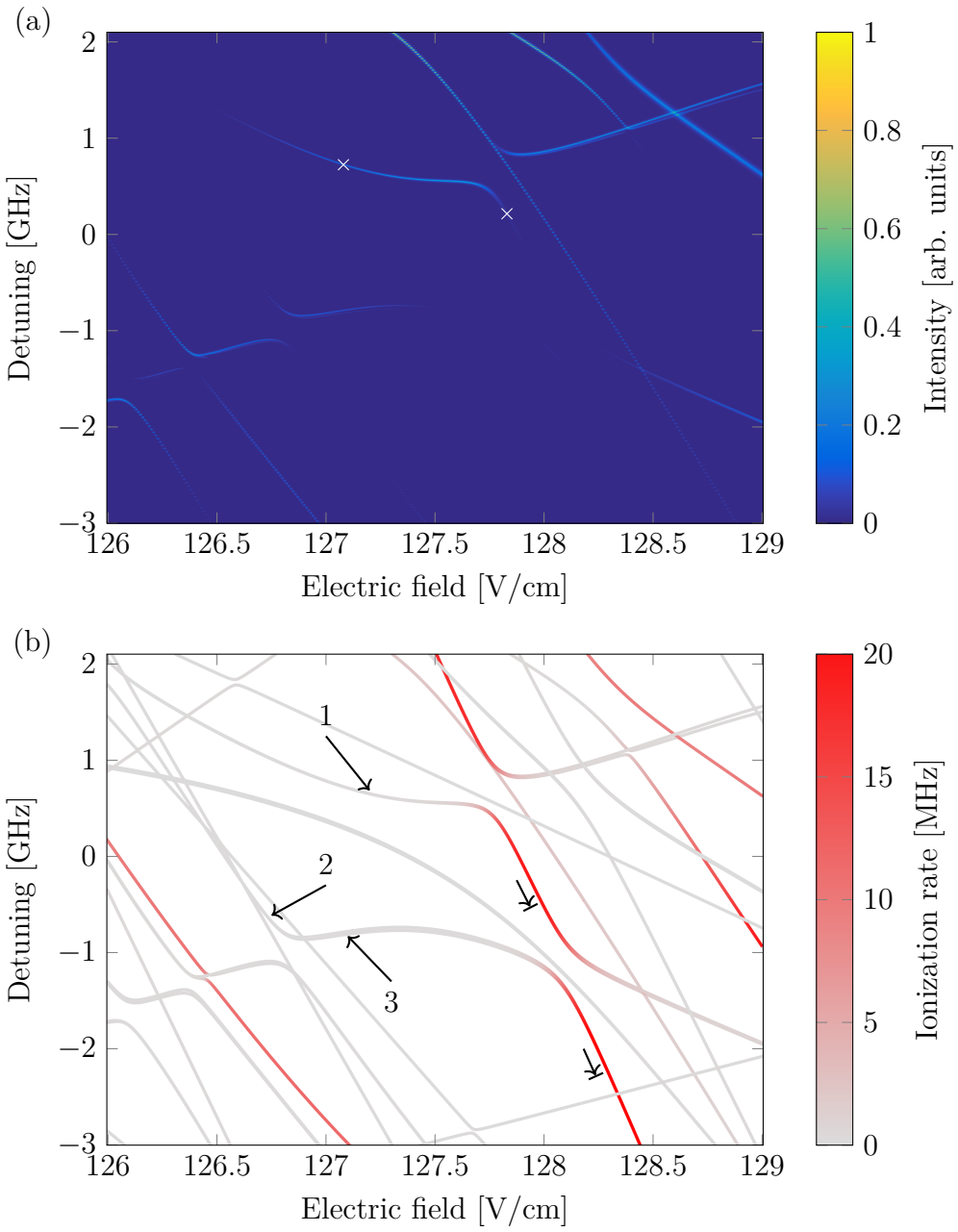

Figure 5.1.: Numerically calculated Stark spectrum of ^{87}Rb [2]. The detuning is given relative to the unperturbed $43S_{1/2}$ state. The $m_j = 0.5, 1.5, 2.5$ substates are plotted. (a) The colorplot shows transition strength and linewidth of the resonances. The crosses mark the Rydberg states excited in the measurement shown in Fig. 5.2. (b) The solid lines depict the ionization rates of the states from nonionizing (gray) to strongly ionizing (red). The arrows with numbers depict the Rydberg states that are excited in the blockade experiment. The arrowheads with delimiters mark the ionizing state that these Rydberg states are transferred to for detection.

threshold is 127 V/cm. The colorplot in sub figure (a) shows the transition strengths and linewidths of the resonances, which are given by the ionization rate of the corresponding state. Since the ionization rates are comparably low in this field region and states with high ionization rate often have a small transition strength, a change in the rate cannot be clearly seen in the colorplot by means of the linewidth. Furthermore the linwidth is capped at a minimum value of 5 MHz. This is done for better visibility in the plot but also to account for broadening mechanisms which dominate in the absence of strong ionization, namely excitation laser linewidth, power broadening and the lifetime of the intermediate state. To visualize the ionization rate, solid lines are plotted in sub figure (b). The color of the line depicts the change from non-ionizing (gray) to an ionization rate of 20 MHz (red). This again shows the existence of states with very low ionization rates (≈ 100 kHz) but also the possibility to rapidly change the ionization rate of a state by a small change in the electric field. In order to experimentally verify these results, we excited Rydberg atoms at different points in the spectrum with a blue laser pulse of 5 µs duration and simultaneously detected the arrival time of the ions with our ion microscope without changing the applied electric field. The blue laser was switched by an AOM with a transition time of 13 ns. The beam had a power of 4 mW, was polarized horizontally and focused to a light sheet (cf. Sec. 3.3). The lower transition was driven by the MOT beams (detuning of 12 MHz to intermediate state, 25 mm $1/e^2$ diameter, 60 mW total power), which were not switched. In Fig. 5.2, the histograms of the ion arrival times of 500 excitation pulses for two different points in the spectrum are plotted. The ionization rate is evaluated by fitting an exponential decay to the ion signal after the end of the excitation pulse. It is already apparent that there is a drastic change in ionization rate from the kHz to the MHz regime. The measurement is repeated for many different points along the resonance line. The results for the ionization rates are shown in Fig. 5.3 together with the values from the numerical calculations. We find good agreement between theory and measurements. In the nonionizing region, the residual ionization rate is even slightly lower than expected (< 100 kHz). At 500 MHz detuning and 127.8 V/cm, respectively, there is a fast increase of the ionization rate up to around 20 MHz.

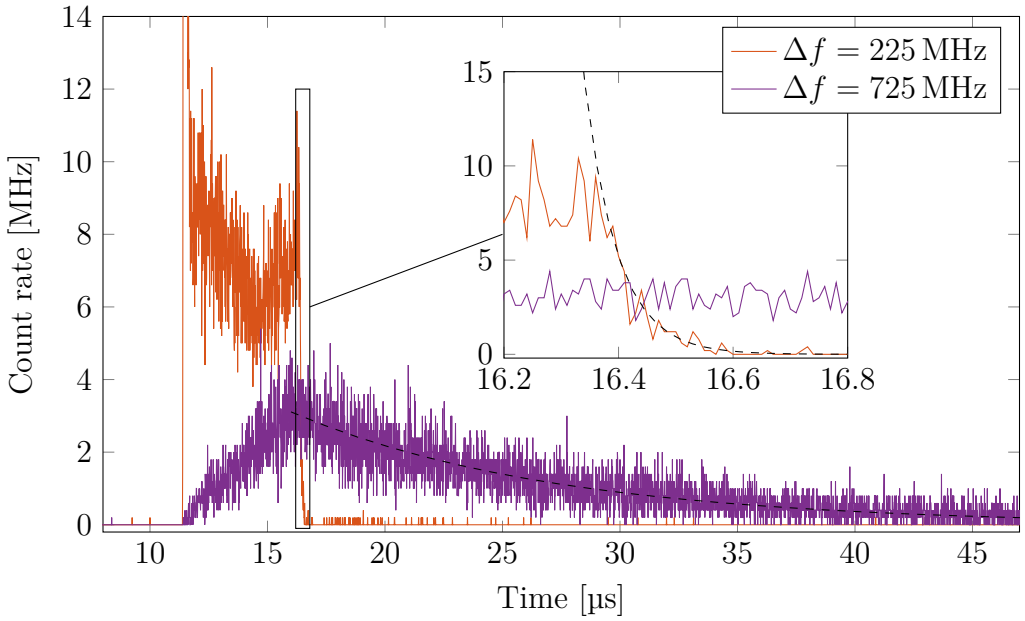

Figure 5.2.: Histograms of ion arrival times for the two different Rydberg states marked with crosses in Fig. 5.1a (bin size of 10 ns, average over 500 excitation pulses for each curve). The excitation pulse of 5 µs duration is switched on between 11.38 µs and 16.38 µs. The ionization rates of Fig. 5.3 are deduced by fitting an exponential decay to the ion signal after the end of the excitation pulse. These fits are depicted as black dashed lines in the plot. The ionization rates are (89.2 ± 3.8) kHz for the slowly ionizing state and (17.4 ± 0.3) MHz for the quickly ionizing state.

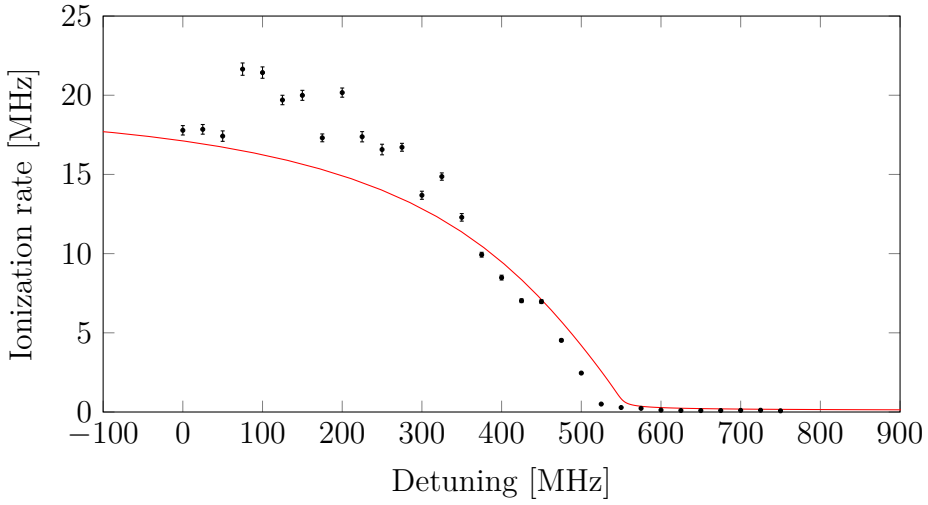

Figure 5.3.: Measured (black dots with errorbars) and calculated (solid red line) ionization rates following the line containing resonance 1 (see Fig. 5.1). Figure and caption taken from [3] and adapted.

5.2. Ionization by adiabatic transfer

Conventionally, when Rydberg atoms are detected via ionization, the electric field is ramped up to a value well above the ionization threshold. For state selective ionization, typically a ramp with a duration of 100 ns to 5 µs is used; in case of spatially resolved imaging, the ramp is normally as fast as possible to avoid movement of the atoms and to have fixed imaging parameters. As discussed in Sec. 4.4, this kind of fast switching is problematic for our imaging system and also not necessary because there are ionizing states nearby.

Therefore, we implemented a novel detection scheme utilizing the highly Stark-shifted resonances presented in the last section. In this scheme, Rydberg atoms are first excited to nonionizing states and the ionization is then done by only a small field change of typically 1 V/cm with the field ramp slow enough to transfer the Rydberg population adiabatically to an ionizing state. The final field value determines the ionization rate. The ionization signal in dependence on the final field is shown in Fig. 5.4. The excitation pulses in this measurement had the same parameters as described in Sec. 5.1. Following the excitation pulse, after a delay of 1 µs, a field ramp with $\approx$ 1 µs transition time is applied. The measurement clearly shows that the ionization rate (and with it the width of the ion peak) can be varied by changing the final field value. Besides the decreasing width of the ion peak, there is also an apparent shift to earlier times. This happens because of our rather slow field ramp, which causes the Rydberg atoms to get ionized before the final field value is reached.

Apart from circumventing the technical limitations of our detector, our ionization method could also be reversed, meaning that the ionizing state can be brought back to the original state. When switching to a much higher field for ionization, the original state evolves through the Stark map and gets redistributed over many Stark-shifted states. This process is obviously not reversible by ramping down the electric field again.

5.3. Measurement of the dipole blockade

The dipole blockade can be measured by analyzing the spatial correlations of the positions of the Rydberg atoms after the excitation laser pulse. For that, the excitation-detection scheme described above was applied to three different Rydberg states depicted with arrows and numbers in Fig. 5.1 and we chose the final value of the electric

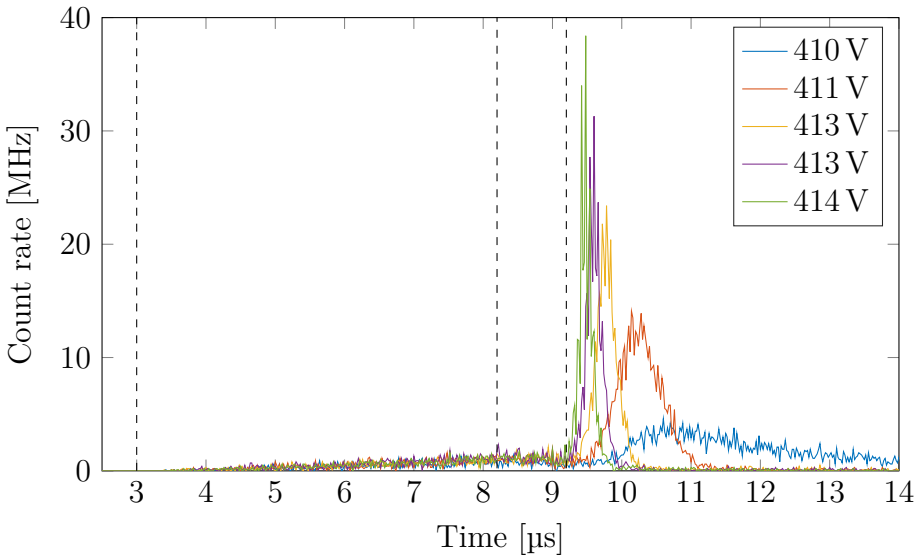

Figure 5.4.: Histogram of ion arrival times for different final values of the extractor voltage (bin size of 20 ns, average over 500 excitation pulses for each curve). The first two dashed vertical lines depict the Rydberg excitation pulse (duration of 5 µs, resonance 1 in Fig. 5.1b), the third line shows the start of the electric-field ramp (transition time $\approx 1\,\mu s$). With increasing voltage, the ionization occurs earlier and faster. The final extractor voltages of 410-414 V correspond to electric fields of 127.5-128.4 V/cm. Figure and caption taken from [3] and adapted.

field such that the Rydberg population gets ionized within 1 µs. The excitation pulse of the blue laser had a duration of 1 µs. It was polarized horizontally and focused to a light sheet (cf. Sec. 3.3). Depending on the transition dipole moment of the Rydberg transition, the power of the blue laser was set to obtain a Rabi frequency of around $2\pi \times 300\,\text{kHz}$. The lower transition was driven by the MOT beams (Rabi frequency around $2\pi \times 8\,\text{MHz}$), which were not switched. The density of the MOT was around $4 \cdot 10^{10}\,1/\text{cm}^3$. The magnification of the ion microscope was set to 1129 with U_{Ex}=±412 V, $U_{L1} = -3\,\text{kV}$, U_{L2}=620 V, U_{L3}=620 V, U_{L4}=690 V (cf. Fig. 2.3). The following table lists the laser detunings (with respect to the unperturbed 43S state), powers and electric field values used for the different resonances:

Resonance	*Laser detuning*	*Laser power*	*Initial E-field*	*Final E-field*
1	686 MHz	0.8 mW	127.2 V/cm	128 V/cm
2	−614 MHz	4 mW	126.7 V/cm	128.4 V/cm
3	−794 MHz	3.8 mW	127.1 V/cm	128.4 V/cm

Each excitation pulse yields around 5 ions and their position and timing infor-

mation is recorded by our ion microscope. For each pulse, the spatial second order correlation function

$$g^{(2)}(u,v) = \frac{\langle\langle f(x+u, y+v) f(x,y)\rangle\rangle_{x,y}}{\langle\langle f(x+u, y+v)\rangle\rangle_{x,y}\langle\langle f(x,y)\rangle\rangle_{x,y}} \tag{5.3}$$

with displacements u, v is calculated with the the detector function

$$f(x,y) = \sum_{i=1}^{N} \delta(x - x_i)\delta(y - y_i). \tag{5.4}$$

x_i, y_i denote the coordinates of the N ions from the excitation pulse. Due to the small number of events in each pulse, the excitation is repeated several thousand times to gather enough data for a meaningful correlation analysis. The resulting correlation functions are summed up and the result is normalized to the correlation function calculated from the (uncorrelated) set of events from all pulses. This normalization accounts for the fact that the detector area is finite, so larger distances between two events are less likely to be observed and thus the correlation function decreases radially from the center. Furthermore, it also accounts for the spatial inhomogeneity of the excitation efficiency due to the Gaussian profile of the light sheet.

The Rydberg blockade shows up as a decreased (< 1) correlation function for small interparticle distances. If plotted as a two-dimensional colorplot as in Fig. 5.5 for the results of resonance 1, this corresponds to a region around the center with $g^{(2)}(u,v) < 1$. An ideal blockade would result in a correlation function going down to zero. Since our excitation volume is not perfectly two-dimensional, in our case the minimal value of $g^{(2)}$ is >0. Furthermore, due to the detector characteristics, there is an uncorrelated ion signal coming from ions that are produced outside of the imaged area. Other than in Fig. 4.11 of Sec. 4.4, this signal cannot be completely separated from the desired signal because of the rather low ramp speed and ionization rate. Hence, the uncorrelated ion signal reduces the decrease of the correlation function.

For better comparability, the radial average of the correlation function is calculated by (in polar coordinates)

$$g^{(2)}_{\mathrm{rad}}(r) = \frac{1}{2\pi r}\int_0^{2\pi} g^{(2)}(r,\phi)\, d\phi \tag{5.5}$$

and the results are plotted in Fig. 5.6 for resonances 2 and 3. A clear change in the blockade behavior is visible. For resonance 2, the blockade effect starts at an

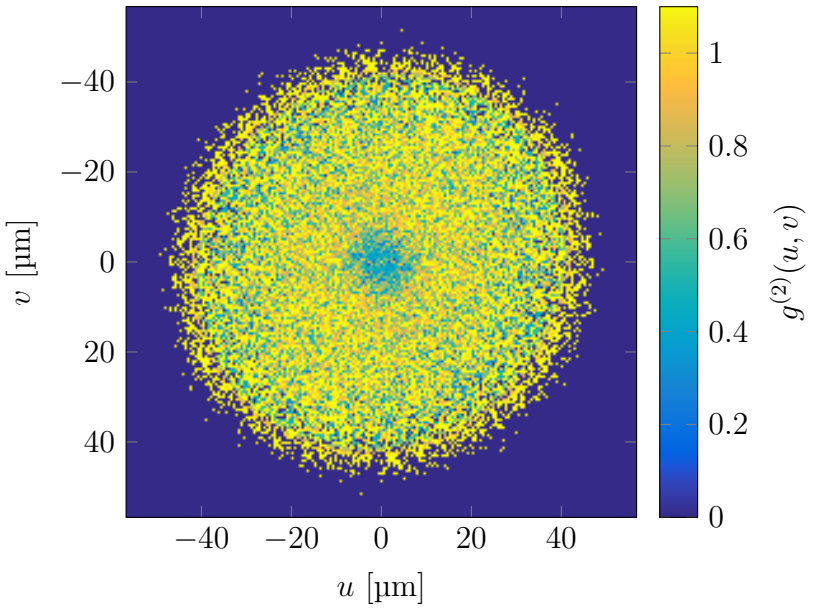

Figure 5.5.: Spatial correlation function $g^{(2)}(u, v)$ when exciting resonance 1 of Fig. 5.1. The Rydberg blockade effect manifests itself by a decrease of $g^{(2)}$ to values smaller than 1 for interatomic separations smaller than the blockade radius. Figure and caption taken from [3].

interatomic distance of 12 µm, for resonance 3 at 2 µm. The two Rydberg states are part of the same resonance line and are only 0.4 V/cm apart from each other. The drastic change in the interaction strength comes from a strongly varying electric dipole moment p_z for the two states visible in the Stark spectrum as a change in the slope of the line. A theoretical value for the blockade radius can be defined as the distance r_b at which the energy shift ΔW due to the interatomic interaction (cf. Eq. 5.2) equals the excitation laser linewidth $\delta\nu_L$:

$$\hbar \cdot 2\pi\delta\nu_L = \Delta W(r_b). \tag{5.6}$$

The dashed vertical lines in Fig. 5.6 depict the theoretical values of the blockade radius (12.5 µm and 2.6 µm, respectively) calculated out of the corresponding dipole moments ($1.90 \cdot 10^{-26}$ Cm and $1.76 \cdot 10^{-27}$ Cm, respectively) and an estimated excitation linewidth of 5 MHz.

The theoretical values for resonances 2 and 3 are in good agreement with the measurement. For resonance 1, the dipole moment is $4.19 \cdot 10^{-27}$ Cm, which would result in a blockade of 4.5 µm. However, the measured blockade is significantly larger. Besides the interaction due to the permanent electric dipole moment, there

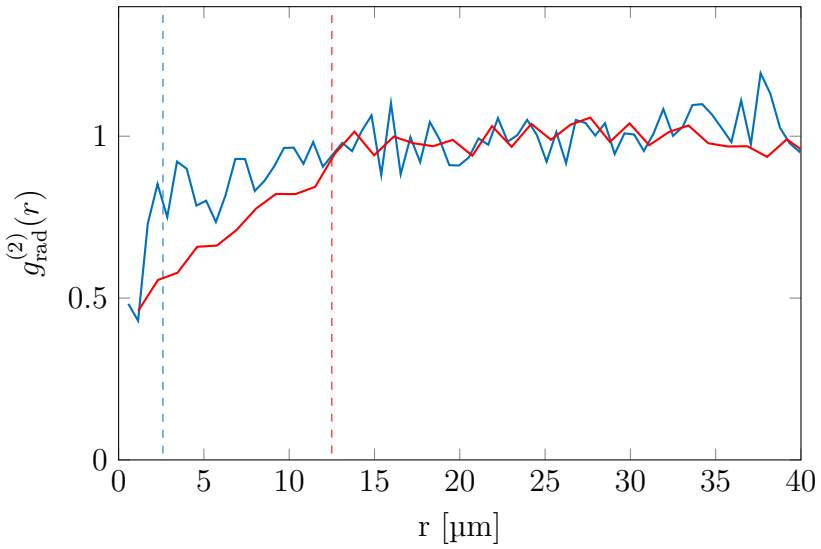

Figure 5.6.: Radial average of $g^{(2)}(u, v)$ for excitation of resonances 2 and 3 from Fig. 5.1. The dashed lines depict the theoretical blockade radii (see Eq. 5.6). Figure taken from [3].

is also always a second order van der Waals interaction [43]. The strength of this interaction depends on the energy level structure, which varies very much in the strongly Stark-shifted regime. Furthermore the presence of one or several resonant interaction channels can vary the interaction strength severely (see Sec. 4.3). Both effects could be the reason for the enhanced interaction that we observe here.

In summary, we have shown in the measurements presented in this chapter, that the Rydberg blockade can be observed at highly Stark-shifted states and the strength of the Rydberg-Rydberg interaction can be altered by small changes in the electric field. Conventional Rydberg blockade experiments operate at zero electric field, which requires a set of electrodes to compensate stray electric fields in all directions, or at small fields in order to induce a dipole moment to the Rydberg atoms. In this work, we have shown an alternative way which utilizes the complicated "spaghetti region" of the Stark spectrum with its diversity of states and varying ionization rates. These properties could be seen as an annoyance, but we have shown that they can also be seen as an advantage, which opens up new perspectives to tailor interaction and ionization of Rydberg states.

6. Conclusion and Outlook

In this work, we have described an ion microscope for magnified imaging of ultracold atoms that was put into operation and characterized experimentally in a cold atom setup [1]. The system incorporates a set of four electrostatic lenses and a MCP for ion detection. The system has a maximum magnification of 1000, simulations show a resolution of better than 100 nm. The measurements show good agreement with the expected parameters from the simulations; the smallest available test structure of 2.7 µm could be imaged easily. We have shown that the microscope is capable of detecting both ground state atoms via photoionization as well as Rydberg atoms via field ionization and subsequent ion imaging. While this work mainly focused on the detection of Rydberg atoms, the microscope is also suitable for detecting other ultracold samples, for example Bose-Einstein condensates. There, the system could be operated in a continuous, quasi non-destructive mode by ionizing only a small subset of the sample. This can be used to analyze global properties like temperature, density and atom number as well as local statistics and opens the possibility for a continuous observation of dynamical processes, for example vortices [88], collective excitations [89] and oscillations [90]. In the field of Rydberg atoms, the microscope can be used for the spatio-temporal analysis of many-body effects like facilitation [91], crystallization [92], Rydberg molecules [93] and ion-atom collisions [94, 95].

The theoretical treatment of highly Stark-shifted Rydberg atoms with the help of a complex absorbing potential (CAP) that was developed in this work, allows for the accurate prediction of wide ranges of the spectrum with only one free parameter. The numerical calculations were verified by measurements of these spectra for different Rydberg states [2]. We have shown the existence of sharp resonances with low ionization rates even for high electric fields above the classical ionization threshold. These findings allow for new ways of performing experiments with Rydberg atoms in a non field-free environment. This is of particular interest when Rydberg atoms are brought close to surfaces, which often exhibit strong static electric fields due to adsorbates [96]. Our results can help towards constructing hybrid quantum devices by coupling

Rydberg atoms to superconducting resonators [97]. Another prospect is the tailoring of the ionization process by using Stark-shifted states of varying ionization rate for the realization of cold ion or electron sources [98–101]. It has also been shown in this work, that with the CAP theory selective field ionization (SFI) signals of Rydberg atoms can be predicted. This was used to investigate the occurrence of Rydberg Förster resonances that become manifest in the SFI signal. At a Förster resonance, the interaction strength between the Rydberg atoms is enhanced, the resulting blockade effect has been observed in the excitation number statistics. The calculation of SFI spectra can be used to select suitable Rydberg states for an experiment as well as to analyze the initial state distribution on the basis of a measured SFI signal.

Direct observation of the Rydberg blockade utilizing the spatial resolution of our ion microscope has been accomplished for highly Stark-shifted Rydberg states by analyzing the spatial correlations of the excited atoms [3]. With the help of the CAP-theory, suitable states with low ionization rates were chosen for the demonstration of the blockade effect. Our work proves that even in high electric fields around the classical ionization limit Rydberg states exist that can be used for blockade experiments. Furthermore, the interaction strength can be tuned by the external electric field. We have implemented a detection technique that ionizes the Rydberg atoms in a controlled way by adiabatic transfer to an ionizing state for subsequent ion imaging. A state with a large interaction strength could be used for quantum gate operations with enhanced fidelity [102]. In quantum simulators, the interaction potential is changed by using a different Rydberg state or by varying the distance between the atoms. Our work shows the possibility of tuning the interaction strength via the applied electric field and can be utilized in the future for the realization of interaction potentials that vary in space and time. The dipole blockade together with the variable ionization rate in the highly Stark-shifted regime can also be used for the realization of Rydberg superatoms [103], deterministic single atom [104], single photon [105] and single ion sources [106] as well as single photon absorbers [107].

Bibliography

[1] M. Stecker, H. Schefzyk, J. Fortágh, and A. Günther, "A high resolution ion microscope for cold atoms", New Journal of Physics **19**, 043020 (2017).

[2] J. Grimmel, M. Stecker, M. Kaiser, F. Karlewski, L. Torralbo-Campo, A. Günther, and J. Fortágh, "Ionization spectra of highly Stark-shifted rubidium Rydberg states", Physical Review A **96**, 013427 (2017).

[3] M. Stecker, J. Grimmel, R. Nold, M. Reinschmidt, J. Fortágh, and A. Günther, "Controlling the dipole blockade of highly Stark-shifted rubidium Rydberg states", to be published (2018).

[4] I. M. Georgescu, S. Ashhab, and F. Nori, "Quantum simulation", Reviews of Modern Physics **86**, 153 (2014).

[5] I. Bloch, J. Dalibard, and W. Zwerger, "Many-body physics with ultracold gases", Reviews of Modern Physics **80**, 885 (2008).

[6] P. Hauke, M. Heyl, L. Tagliacozzo, and P. Zoller, "Measuring multipartite entanglement through dynamic susceptibilities", Nature Physics **12**, 778 (2016).

[7] H. Pichler, G. Zhu, A. Seif, P. Zoller, and M. Hafezi, "Measurement Protocol for the Entanglement Spectrum of Cold Atoms", Physical Review X **6**, 041033 (2016).

[8] W. Hofstetter, J. I. Cirac, P. Zoller, E. Demler, and M. D. Lukin, "High-Temperature Superfluidity of Fermionic Atoms in Optical Lattices", Physical Review Letters **89**, 220407 (2002).

[9] V. Khemani, A. Lazarides, R. Moessner, and S. L. Sondhi, "Phase Structure of Driven Quantum Systems", Physical Review Letters **116**, 250401 (2016).

[10] T. Monz, P. Schindler, J. T. Barreiro, M. Chwalla, D. Nigg, W. A. Coish, M. Harlander, W. Hänsel, M. Hennrich, and R. Blatt, "14-Qubit Entanglement: Creation and Coherence", Physical Review Letters **106**, 130506 (2011).

[11] R. Islam, C. Senko, W. C. Campbell, S. Korenblit, J. Smith, A. Lee, E. E. Edwards, C.-C. J. Wang, J. K. Freericks, and C. Monroe, "Emergence and Frustration of Magnetism with Variable-Range Interactions in a Quantum Simulator", Science **340**, 583 (2013).

[12] M. Gärttner, J. G. Bohnet, A. Safavi-Naini, M. L. Wall, J. J. Bollinger, and A. M. Rey, "Measuring out-of-time-order correlations and multiple quantum spectra in a trapped-ion quantum magnet", Nature Physics **13**, 781 (2017).

[13] N. Ofek, A. Petrenko, R. Heeres, P. Reinhold, Z. Leghtas, B. Vlastakis, Y. Liu, L. Frunzio, S. M. Girvin, L. Jiang, M. Mirrahimi, M. H. Devoret, and R. J. Schoelkopf, "Extending the lifetime of a quantum bit with error correction in superconducting circuits", Nature **536**, 441 (2016).

[14] C. Song, K. Xu, W. Liu, C.-p. Yang, S.-B. Zheng, H. Deng, Q. Xie, K. Huang, Q. Guo, L. Zhang, P. Zhang, D. Xu, D. Zheng, X. Zhu, H. Wang, Y.-A. Chen, C.-Y. Lu, S. Han, and J.-W. Pan, "10-Qubit Entanglement and Parallel Logic Operations with a Superconducting Circuit", Physical Review Letters **119**, 180511 (2017).

[15] D. Greif, M. F. Parsons, A. Mazurenko, C. S. Chiu, S. Blatt, F. Huber, G. Ji, and M. Greiner, "Site-resolved imaging of a fermionic Mott insulator", Science **351**, 953 (2016).

[16] A. Mazurenko, C. S. Chiu, G. Ji, M. F. Parsons, M. Kanász-Nagy, R. Schmidt, F. Grusdt, E. Demler, D. Greif, and M. Greiner, "A cold-atom Fermi–Hubbard antiferromagnet", Nature **545**, 462 (2017).

[17] W. S. Bakr, J. I. Gillen, A. Peng, S. Fölling, and M. Greiner, "A quantum gas microscope for detecting single atoms in a Hubbard-regime optical lattice", Nature **462**, 74 (2009).

[18] J. F. Sherson, C. Weitenberg, M. Endres, M. Cheneau, I. Bloch, and S. Kuhr, "Single-atom-resolved fluorescence imaging of an atomic Mott insulator", Nature **467**, 68 (2010).

[19] D. Barredo, S. de Léséleuc, V. Lienhard, T. Lahaye, and A. Browaeys, "An atom-by-atom assembler of defect-free arbitrary two-dimensional atomic arrays", Science **354**, 1021 (2016).

[20] M. Endres, H. Bernien, A. Keesling, H. Levine, E. R. Anschuetz, A. Krajenbrink, C. Senko, V. Vuletic, M. Greiner, and M. D. Lukin, "Atom-by-atom assembly of defect-free one-dimensional cold atom arrays", Science **354**, 1024 (2016).

[21] H. Weimer, M. Müller, I. Lesanovsky, P. Zoller, and H. P. Büchler, "A Rydberg quantum simulator", Nature Physics **6**, 382 (2010).

[22] H. Labuhn, D. Barredo, S. Ravets, S. de Léséleuc, T. Macrì, T. Lahaye, and A. Browaeys, "Tunable two-dimensional arrays of single Rydberg atoms for realizing quantum Ising models", Nature **534**, 667 (2016).

[23] S. de Léséleuc, D. Barredo, V. Lienhard, A. Browaeys, and T. Lahaye, "Optical Control of the Resonant Dipole-Dipole Interaction between Rydberg Atoms", Physical Review Letters **119**, 053202 (2017).

[24] H. Bernien, S. Schwartz, A. Keesling, H. Levine, A. Omran, H. Pichler, S. Choi, A. S. Zibrov, M. Endres, M. Greiner, V. Vuletić, and M. D. Lukin, "Probing many-body dynamics on a 51-atom quantum simulator", Nature **551**, 579 (2017).

[25] J. Zeiher, J.-y. Choi, A. Rubio-Abadal, T. Pohl, R. van Bijnen, I. Bloch, and C. Gross, "Coherent Many-Body Spin Dynamics in a Long-Range Interacting Ising Chain", Physical Review X **7**, 041063 (2017).

[26] T. D. Ladd, F. Jelezko, R. Laflamme, Y. Nakamura, C. Monroe, and J. L. O'Brien, "Quantum Computing", Nature **464**, 45 (2010).

[27] M. A. Nielsen and I. L. Chuang, *Quantum Computation and Quantum Information* (Cambridge University Press, Cambridge, 2000).

[28] P. W. Shor, "Algorithms for quantum computation: discrete logarithms and factoring", 124 (1994).

[29] R. Blatt and D. Wineland, "Entangled states of trapped atomic ions", Nature **453**, 1008 (2008).

[30] M. H. Devoret and R. J. Schoelkopf, "Superconducting Circuits for Quantum Information: An Outlook", Science **339**, 1169 (2013).

[31] X. Li, Y. Wu, D. Steel, D. Gammon, T. H. Stievater, D. S. Katzer, D. Park, C. Piermarocchi, and L. J. Sham, "An All-Optical Quantum Gate in a Semiconductor Quantum Dot", Science **301**, 809 (2003).

[32] P. Kok, W. J. Munro, K. Nemoto, T. C. Ralph, J. P. Dowling, and G. J. Milburn, "Linear optical quantum computing with photonic qubits", Reviews of Modern Physics **79**, 135 (2007).

[33] I. Bloch, "Quantum coherence and entanglement with ultracold atoms in optical lattices", Nature **453**, 1016 (2008).

[34] J. Benhelm, G. Kirchmair, C. F. Roos, and R. Blatt, "Towards fault-tolerant quantum computing with trapped ions", Nature Physics **4**, 463 (2008).

[35] D. Jaksch, J. I. Cirac, P. Zoller, S. L. Rolston, R. Côté, and M. D. Lukin, "Fast Quantum Gates for Neutral Atoms", Physical Review Letters **85**, 2208 (2000).

[36] M. D. Lukin, M. Fleischhauer, R. Cote, L. M. Duan, D. Jaksch, J. I. Cirac, and P. Zoller, "Dipole Blockade and Quantum Information Processing in Mesoscopic Atomic Ensembles", Physical Review Letters **87**, 037901 (2001).

[37] L. Isenhower, E. Urban, X. L. Zhang, A. T. Gill, T. Henage, T. A. Johnson, T. G. Walker, and M. Saffman, "Demonstration of a Neutral Atom Controlled-NOT Quantum Gate", Physical Review Letters **104**, 10503 (2010).

[38] T. Wilk, A. Gaëtan, C. Evellin, J. Wolters, Y. Miroshnychenko, P. Grangier, and A. Browaeys, "Entanglement of Two Individual Neutral Atoms Using Rydberg Blockade", Physical Review Letters **104**, 2 (2010).

[39] A. S. Sørensen, C. H. van der Wal, L. I. Childress, and M. D. Lukin, "Capacitive Coupling of Atomic Systems to Mesoscopic Conductors", Physical Review Letters **92**, 063601 (2004).

[40] D. Petrosyan and M. Fleischhauer, "Quantum Information Processing with Single Photons and Atomic Ensembles in Microwave Coplanar Waveguide Resonators", Physical Review Letters **100**, 170501 (2008).

[41] S. Bernon, H. Hattermann, D. Bothner, M. Knufinke, P. Weiss, F. Jessen, D. Cano, M. Kemmler, R. Kleiner, D. Koelle, and J. Fortágh, "Manipulation and coherence of ultra-cold atoms on a superconducting atom chip", Nature Communications **4**, 2380 (2013).

[42] T. F. Gallagher, *Rydberg atoms* (Cambridge University Press, Cambridge, 1994).

[43] A. Reinhard, T. C. Liebisch, B. Knuffman, and G. Raithel, "Level shifts of rubidium Rydberg states due to binary interactions", Physical Review A **75**, 032712 (2007).

[44] D. Tong, S. M. Farooqi, J. Stanojevic, S. Krishnan, Y. P. Zhang, R. Côté, E. E. Eyler, and P. L. Gould, "Local Blockade of Rydberg Excitation in an Ultracold Gas", Physical Review Letters **93**, 063001 (2004).

[45] W. Ketterle, D. S. Durfee, and D. M. Stamper-Kurn, "Making, probing and understanding Bose-Einstein condensates", Proceedings of the International School of Physics "Enrico Fermi", 67 (1999).

[46] M. R. Andrews, M.-O. Mewes, N. J. van Druten, D. S. Durfee, D. M. Kurn, and W. Ketterle, "Direct, Nondestructive Observation of a Bose Condensate", Science **273**, 84 (1996).

[47] M. T. Depue, S. Lukman Winoto, D. J. Han, and D. S. Weiss, "Transient compression of a MOT and high intensity fluorescent imaging of optically thick clouds of atoms", Optics Communications **180**, 73 (2000).

[48] A. Schwarzkopf, R. E. Sapiro, and G. Raithel, "Imaging Spatial Correlations of Rydberg Excitations in Cold Atom Clouds", Physical Review Letters **107**, 103001 (2011).

[49] T. Gericke, P. Würtz, D. Reitz, T. Langen, and H. Ott, "High-resolution scanning electron microscopy of an ultracold quantum gas", Nature Physics **4**, 949 (2008).

[50] K. Singer, M. Reetz-Lamour, T. Amthor, L. G. Marcassa, and M. Weidemüller, "Suppression of Excitation and Spectral Broadening Induced by Interactions in a Cold Gas of Rydberg Atoms", Physical Review Letters **93**, 163001 (2004).

[51] T. Vogt, M. Viteau, A. Chotia, J. Zhao, D. Comparat, and P. Pillet, "Electric-Field Induced Dipole Blockade with Rydberg Atoms", Physical Review Letters **99**, 073002 (2007).

[52] N. Thaicharoen, L. F. Gonçalves, and G. Raithel, "Atom-Pair Kinetics with Strong Electric-Dipole Interactions", Physical Review Letters **116**, 213002 (2016).

[53] H. Schefzyk, "Entwicklung eines hochauflösenden Ionenmikroskops für kalte Atome", PhD thesis (Universität Tübingen, Tübingen, 2016).

[54] D. A. Steck, *Rubidium 87 D Line Data*, (revision 2.1.5, 13 January 2015) `http://steck.us/alkalidata`.

[55] L. Ricci, M. Weidemüller, T. Esslinger, A. Hemmerich, C. Zimmermann, V. Vuletic, W. König, and T. Hänsch, "A compact grating-stabilized diode laser system for atomic physics", Optics Communications **117**, 541 (1995).

[56] C. E. Shannon, "Communication in the presence of noise", Proceedings of the IRE **37**, 10 (1949).

[57] W. Li, I. Mourachko, M. W. Noel, and T. F. Gallagher, "Millimeter-wave spectroscopy of cold Rb Rydberg atoms in a magneto-optical trap: Quantum defects of the ns, np, and nd series", Physical Review A **67**, 052502 (2003).

[58] A. Tauschinsky, R. Newell, H. B. van Linden van den Heuvell, and R. J. C. Spreeuw, "Measurement of ^{87}Rb Rydberg-state hyperfine splitting in a room-temperature vapor cell", Physical Review A **87**, 042522 (2013).

[59] D. Meschede, "Centimeter-wave spectroscopy of highly excited rubidium atoms", Journal of the Optical Society of America B **4**, 413 (1987).

[60] M. L. Zimmerman, M. G. Littman, M. M. Kash, and D. Kleppner, "Stark Structure of the Rydberg States of Alkali-Metal Atoms", Physical Review A **20**, 2251 (1979).

[61] J. Grimmel, M. Mack, F. Karlewski, F. Jessen, M. Reinschmidt, N. Sandor, and J. Fortagh, "Measurement and numerical calculation of Rubidium Rydberg Stark spectra", New Journal of Physics **17**, 53005 (2015).

[62] J. Han, Y. Jamil, D. V. L. Norum, P. J. Tanner, and T. F. Gallagher, "Rb nf quantum defects from millimeter-wave spectroscopy of cold ^{85}Rb Rydberg atoms", Physical Review A **74**, 054502 (2006).

[63] K. Afrousheh, P. Bohlouli-Zanjani, J. A. Petrus, and J. D. D. Martin, "Determination of the ^{85}Rb ng-series quantum defect by electric-field-induced resonant energy transfer between cold Rydberg atoms", Physical Review A **74**, 062712 (2006).

[64] M. Mack, F. Karlewski, H. Hattermann, S. Höckh, F. Jessen, D. Cano, and J. Fortágh, "Measurement of absolute transition frequencies of ^{87}Rb to nS and nD Rydberg states by means of electromagnetically induced transparency", Physical Review A **83**, 052515 (2011).

[65] M. Marinescu, H. R. Sadeghpour, and A. Dalgarno, "Dispersion coefficients for alkali-metal dimers", Physical Review A **49**, 982 (1994).

[66] R. J. Damburg and V. V. Kolosov, "A hydrogen atom in a uniform electric field. iii", Journal of Physics B: Atomic and Molecular Physics **12**, 2637 (1979).

[67] R. Kosloff and D. Kosloff, "Absorbing boundaries for wave propagation problems", Journal of Computational Physics **63**, 363 (1986).

[68] U. V. Riss and H. D. Meyer, "Calculation of resonance energies and widths using the complex absorbing potential method", Journal of Physics B: Atomic, Molecular and Optical Physics **26**, 4503 (1993).

[69] S. Sahoo and Y. K. Ho, "The complex absorbing potential method (CAP) to study the Stark effect in hydrogen and lithium", Journal of Physics B: Atomic, Molecular and Optical Physics **33**, 2195 (2000).

[70] C. Zener, "Non-adiabatic crossing of energy levels", Proceedings of the Royal Society of London A: Mathematical, Physical and Engineering Sciences **137**, 696 (1932).

[71] F. Robicheaux, C. Wesdorp, and L. D. Noordam, "Selective field ionization in Li and Rb: Theory and experiment", Physical Review A **62**, 043404 (2000).

[72] M. Førre and J. P. Hansen, "Selective-field-ionization dynamics of a lithium $m = 2$ Rydberg state: Landau-Zener model versus quantal approach", Physical Review A **67**, 053402 (2003).

[73] R. Feynman, J. Hollingsworth, M. Vennettilli, T. Budner, R. Zmiewski, D. P. Fahey, T. J. Carroll, and M. W. Noel, "Quantum interference in the field ionization of Rydberg atoms", Physical Review A **92**, 043412 (2015).

[74] T. Förster, "Zwischenmolekulare Energiewanderung und Fluoreszenz", Annalen der Physik **437**, 55 (1948).

[75] J. M. Nipper, "Interacting Rydberg atoms: Coherent control at Förster resonances and polar homonuclear molecules", PhD thesis (Universität Stuttgart, Stuttgart, 2012).

[76] J. Nipper, J. B. Balewski, A. T. Krupp, B. Butscher, R. Löw, and T. Pfau, "Highly resolved measurements of stark-tuned förster resonances between rydberg atoms", Physical Review Letters **108**, 113001 (2012).

[77] A. Reinhard, K. C. Younge, T. C. Liebisch, B. Knuffman, P. R. Berman, and G. Raithel, "Double-Resonance Spectroscopy of Interacting Rydberg-Atom Systems", Physical Review Letters **100**, 233201 (2008).

[78] S. Ravets, H. Labuhn, D. Barredo, L. Béguin, T. Lahaye, and A. Browaeys, "Coherent dipole–dipole coupling between two single Rydberg atoms at an electrically-tuned Förster resonance", Nature Physics **10**, 914 (2014).

[79] F. Robicheaux and J. V. Hernández, "Many-body wave function in a dipole blockade configuration", Physical Review A **72**, 063403 (2005).

[80] C. Ates, T. Pohl, T. Pattard, and J. M. Rost, "Strong interaction effects on the atom counting statistics of ultracold Rydberg gases", Journal of Physics B: Atomic, Molecular and Optical Physics **39**, L233 (2006).

[81] A. Reinhard, K. C. Younge, and G. Raithel, "Effect of Förster resonances on the excitation statistics of many-body Rydberg systems", Physical Review A **78**, 060702 (2008).

[82] L. Mandel, "Sub-Poissonian photon statistics in resonance fluorescence", Optics Letters **4**, 205 (1979).

[83] M. Saffman, T. G. Walker, and K. Mølmer, "Quantum information with Rydberg atoms", Reviews of Modern Physics **82**, 2313 (2010).

[84] A. Reinhard, T. Cubel Liebisch, K. C. Younge, P. R. Berman, and G. Raithel, "Rydberg-Rydberg Collisions: Resonant Enhancement of State Mixing and Penning Ionization", Physical Review Letters **100**, 123007 (2008).

[85] T. G. Walker and M. Saffman, "Consequences of Zeeman degeneracy for the van der Waals blockade between Rydberg atoms", Physical Review A **77**, 032723 (2008).

[86] P. Bohlouli-Zanjani, J. A. Petrus, and J. D. D. Martin, "Enhancement of Rydberg Atom Interactions Using ac Stark Shifts", Physical Review Letters **98**, 203005 (2007).

[87] L. F. Gonçalves and L. G. Marcassa, "Control of Rydberg-atom blockade by dc electric-field orientation in a quasi-one-dimensional sample", Physical Review A **94**, 043424 (2016).

[88] M. R. Matthews, B. P. Anderson, P. C. Haljan, D. S. Hall, C. E. Wieman, and E. A. Cornell, "Vortices in a Bose-Einstein Condensate", Physical Review Letters **83**, 2498 (1999).

[89] M.-O. Mewes, M. R. Andrews, N. J. van Druten, D. M. Kurn, D. S. Durfee, C. G. Townsend, and W. Ketterle, "Collective Excitations of a Bose-Einstein Condensate in a Magnetic Trap", Physical Review Letters **77**, 988 (1996).

[90] A. Altmeyer, S. Riedl, C. Kohstall, M. J. Wright, R. Geursen, M. Bartenstein, C. Chin, J. H. Denschlag, and R. Grimm, "Precision Measurements of Collective Oscillations in the BEC-BCS Crossover", Physical Review Letters **98**, 040401 (2007).

[91] I. Lesanovsky and J. P. Garrahan, "Out-of-equilibrium structures in strongly interacting Rydberg gases with dissipation", Physical Review A **90**, 011603 (2014).

[92] P. Schauß, J. Zeiher, T. Fukuhara, S. Hild, M. Cheneau, T. Macrì, T. Pohl, I. Bloch, and C. Gross, "Crystallization in Ising quantum magnets", Science **347**, 1455 (2015).

[93] V. Bendkowsky, B. Butscher, J. Nipper, J. P. Shaffer, R. Löw, and T. Pfau, "Observation of ultralong-range Rydberg molecules", Nature **458**, 1005 (2009).

[94] M. Tomza, K. Jachymski, R. Gerritsma, A. Negretti, T. Calarco, Z. Idziaszek, and P. S. Julienne, "Cold hybrid ion-atom systems", arXiv:1708.07832 (2017).

[95] T. Schmid, C. Veit, N. Zuber, R. Löw, T. Pfau, M. Tarana, and M. Tomza, "Rydberg molecules for ion-atom scattering in the ultracold regime", Physical Review Letters **120**, 153401 (2018).

[96] H. Hattermann, M. Mack, F. Karlewski, F. Jessen, D. Cano, and J. Fortágh, "Detrimental adsorbate fields in experiments with cold Rydberg gases near surfaces", Physical Review A **86**, 022511 (2012).

[97] H. Hattermann, D. Bothner, L. Y. Ley, B. Ferdinand, D. Wiedmaier, L. Sárkány, R. Kleiner, D. Koelle, and J. Fortágh, "Coupling ultracold atoms to a superconducting coplanar waveguide resonator", Nature Communications **8**, 2254 (2017).

[98] L. Kime, A. Fioretti, Y. Bruneau, N. Porfido, F. Fuso, M. Viteau, G. Khalili, N. Šantić, A. Gloter, B. Rasser, P. Sudraud, P. Pillet, and D. Comparat, "High-flux monochromatic ion and electron beams based on laser-cooled atoms", Physical Review A **88**, 033424 (2013).

[99] D. Murphy, R. E. Scholten, and B. M. Sparkes, "Increasing the Brightness of Cold Ion Beams by Suppressing Disorder-Induced Heating with Rydberg Blockade", Physical Review Letters **115**, 214802 (2015).

[100] D. J. Thompson, D. Murphy, R. W. Speirs, R. M. W. van Bijnen, A. J. McCulloch, R. E. Scholten, and B. M. Sparkes, "Suppression of Emittance Growth Using a Shaped Cold Atom Electron and Ion Source", Physical Review Letters **117**, 193202 (2016).

[101] E. Moufarej, M. Vielle-Grosjean, G. Khalili, A. J. McCulloch, F. Robicheaux, Y. J. Picard, and D. Comparat, "Forced field ionization of Rydberg states for the production of monochromatic beams", Physical Review A **95**, 043409 (2017).

[102] D. Petrosyan, F. Motzoi, M. Saffman, and K. Mølmer, "High-fidelity Rydberg quantum gate via a two-atom dark state", Physical Review A **96**, 042306 (2017).

[103] T. M. Weber, M. Höning, T. Niederprüm, T. Manthey, O. Thomas, V. Guarrera, M. Fleischhauer, G. Barontini, and H. Ott, "Mesoscopic Rydberg-blockaded ensembles in the superatom regime and beyond", Nature Physics **11**, 157 (2015).

[104] M. Saffman and T. G. Walker, "Creating single-atom and single-photon sources from entangled atomic ensembles", Physical Review A **66**, 065403 (2002).

[105] D. Petrosyan, "Dipolar exchange induced transparency with Rydberg atoms", New Journal of Physics **19**, 033001 (2017).

[106] C. Ates, I. Lesanovsky, C. S. Adams, and K. J. Weatherill, "Fast and Quasi-deterministic Single Ion Source from a Dipole-Blockaded Atomic Ensemble", Physical Review Letters **110**, 213003 (2013).

[107] J. Honer, R. Löw, H. Weimer, T. Pfau, and H. P. Büchler, "Artificial Atoms Can Do More Than Atoms: Deterministic Single Photon Subtraction from Arbitrary Light Fields", Physical Review Letters **107**, 093601 (2011).

A. Publication [1]

IOP Publishing New J. Phys. 19 (2017) 043020 https://doi.org/10.1088/1367-2630/aa6741

New Journal of Physics
The open access journal at the forefront of physics

Deutsche Physikalische Gesellschaft DPG
IOP Institute of Physics
Published in partnership with: Deutsche Physikalische Gesellschaft and the Institute of Physics

OPEN ACCESS

RECEIVED
2 December 2016

REVISED
17 February 2017

ACCEPTED FOR PUBLICATION
16 March 2017

PUBLISHED
13 April 2017

PAPER

A high resolution ion microscope for cold atoms

Markus Stecker[1], **Hannah Schefzyk, József Fortágh and Andreas Günther**

Center for Quantum Science, Physikalisches Institut, Eberhard Karls Universität Tübingen, Auf der Morgenstelle 14, D-72076 Tübingen, Germany

[1] Author to whom any correspondence should be addressed.

E-mail: markus.stecker@uni-tuebingen.de **and** a.guenther@uni-tuebingen.de

Keywords: ultracold gases, ion microscopy, ion optics, photoionization, charged-particle detector, Rydberg atoms

Abstract

We report on an ion-optical system that serves as a microscope for ultracold ground state and Rydberg atoms. The system is designed to achieve a magnification of up to 1000 and a spatial resolution in the 100 nm range, thereby surpassing many standard imaging techniques for cold atoms. The microscope consists of four electrostatic lenses and a microchannel plate in conjunction with a delay line detector in order to achieve single particle sensitivity with high temporal and spatial resolution. We describe the design process of the microscope including ion-optical simulations of the imaging system and characterize aberrations and the resolution limit. Furthermore, we present the experimental realization of the microscope in a cold atom setup and investigate its performance by patterned ionization with a structure size down to 2.7 μm. The microscope meets the requirements for studying various many-body effects, ranging from correlations in cold quantum gases up to Rydberg molecule formation.

1. Introduction

The development of efficient laser cooling [1] paved the way to the production of ultracold atom clouds with temperatures down to several nanokelvin and finally to the experimental realization of Bose–Einstein condensates [2, 3] and degenerate Fermi gases [4]. In order to study the unique properties of ultracold quantum matter, various techniques have been established.

The standard way to image ultracold atom clouds is absorption imaging [5], where the cloud is illuminated by a resonant laser beam and the shadow image is recorded on a camera. However, the cloud is destroyed by this method. The destruction can be suppressed when using the related method of phase contrast imaging, allowing to image the same cloud several times [6–8], yet at a reduced contrast.

For non-destructive imaging of dilute samples with single atom sensitivity, fluorescence imaging is typically used. Here, non-destructive means that the atoms are not lost out of the trap during the imaging process. In general, this type of imaging requires relatively long exposure times up to 1 s to gather enough fluorescence photons. During this time the atoms may heat up, such that single atom resolution is typically achieved in deep trapping structures. With cold atoms loaded into a two dimensional optical lattice and a light-optical system with high numerical aperture placed close to the atom sample, a spatial resolution below 1 μm could be achieved with single atom and single site sensitivity [9, 10]. These 'quantum gas microscopes' revolutionized the capabilities of detection and control of quantum many body systems and allow for example the direct observation of the superfluid to Mott insulator phase transition on the microscopic level [10, 11]. Recently, this technique was extended from bosonic to fermionic quantum matter [12–15], thus providing an ideal quantum simulator for investigating solid-state Fermi systems that are difficult to analyze numerically [16, 17]. These microscopes promise important insights into open questions such as high-temperature superconductivity.

Above methods work well for closed cycle transitions, where multiple photons within the visible or near infrared regime can be scattered. If not ground state atoms but Rydberg atoms (atoms in states of high principal quantum number [18]) shall be imaged, the imaging techniques cannot always be applied directly. In case of earth alkali Rydberg atoms, the second valence electron can be used for such a closed cycle [19]. But with the

more commonly used alkali Rydberg atoms, only an indirect approach is possible, by detecting losses in the ground state population [20, 21] or by transferring the Rydberg population to the detectable ground state [22]. Thus, alkali Rydbergs are preferably detected by ionization [18]—which also works for ground state atoms [23]—or alternatively by the all-optical approach of electromagnetic induced transparency [24, 25].

The detection of ions or electrons with high temporal and spatial resolution can be achieved with microchannel plates (MCP). Such detectors have been used to image cold electron or ion beams extracted out of a laser-cooled atom cloud [26–30]. Similar to a field ion microscope, spatially resolved detection of Rydberg atoms has been demonstrated by ionization and acceleration in the divergent electrical field of a metallic nanotip with a magnification of 300 and a resolution better than 1 μm [31, 32]. Imaging of spatially structured photoionization and Rydberg excitation patterns in a magneto-optical trap (MOT) could be achieved with a magnification of 46 and a resolution of 10–20 μm [33]. In a different approach, a spatial resolution of 100 nm has been realized, using a scanning electron microscope for local ionization of cold atoms [34, 35]. All these methods image a two-dimensional plane. However, a MCP can also be used for three-dimensional detection, with the third dimension being calculated out of the timing information, as demonstrated with a Bose–Einstein condensate of metastable helium [36].

Here, we present a novel ion microscope for *in situ* and real-time imaging of ultracold atomic gases. The microscope features a full ion-optical imaging system with four electrostatic lenses and a MCP of 40 mm diameter for ion detection. Using the MCP in conjunction with a delay line detector (DLD), single particle sensitivity with high temporal and spatial resolution is achieved. Depending on the ionization scheme, the system may be used for detecting ground state atoms as well as Rydberg atoms. The ion microscope has been optimized for detecting cold atomic ensembles with typical extensions in the 10–100 μm range. Therefore, the magnification can be adjusted between 10 and 1000 with a theoretical resolution limit of 100 nm. Ion-optical abberations have been minimized to provide a distortion-free imaging over the whole field of view. A large depth of field ensures the possibility to reckon back from the timing information onto the third spatial direction. We demonstrate the microscope using a continuously operated MOT of rubidium atoms. In order to test the performance of the microscope, different optical ionization patterns are imprinted onto the MOT, with the generated ions being imaged by the electrostatic lens system.

2. Ion optics

In analogy to light optics, where light beams can be refracted by materials with different refractive indices, the trajectories of charged particles can be manipulated by electromagnetic fields. The trajectories of ions are—compared to electrons—less sensitive to magnetic fields, so we use electrostatic fields for our ion-optical system. Our setup consists of a set of four einzel lenses—a type of lens that is typically used for low-energy ions [37]. Each einzel lens consists of three consecutive, rotational symmetric electrodes with an aperture. Usually, the two outer electrodes are held at the same electric potential, so the energy of the charged particle after exiting the lens is equal to its energy before entering. By changing the potential of the inner electrode, the focal length of the lens can be varied.

For the design of the ion optics, we made use of a commercial field and particle trajectory simulation program. The program calculates the electrostatic potential for a given electrode geometry by applying a finite difference method and then simulates charged particle trajectories in this potential. All measures like aperture sizes, lens separations and electrode lengths have been optimized to meet the microscope's target specifications with a maximum magnification of 1000 and a resolution better than 100 nm (see section 3).

The microscope is realized in a 700 mm long tube with a diameter of 111 mm (see figure 1 and table 1). The object, here an atom cloud in a MOT, is centered in between a pair of extraction electrodes. These are typically held at $U_{\mathrm{ext}} = \pm 500$ V and form the electric field to extract the ions generated in the MOT. Four consecutive einzel lenses image the ions onto a MCP detector with 40 mm diameter. Starting with einzel lens 1, each lens produces a magnified image in the image plane behind the lens, which is further magnified by the next lens and finally imaged onto the MCP plane. In order to achieve a sharp image, the focal length of each lens is matched to the position of the image plane of the previous lens. The position of the image planes is determined by simulating different ion trajectories coming from a common starting point and determining the intersection of the trajectories behind the lens. There are of course several voltage settings for the different lenses to achieve a sharp image for a specific magnification but typically the refractive power should be distributed homogeneously over the lenses to reduce aberrations.

The drift tubes between the lenses and the outer electrodes of the lenses 2, 3 and 4 are held at -2.4 kV which equals the potential at the front plate of the MCP detector. The drift tubes keep the lenses at a fixed distance and ensure an undisturbed (field free) particle movement in between the lenses. In contrast to the other lenses, einzel lens 1, with the negative extractor serving as its first electrode, acts as an immersion lens, accelerating the ions to

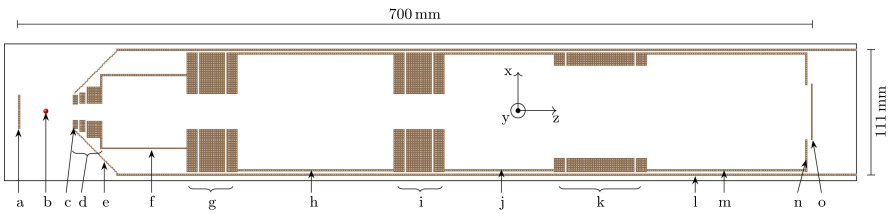

Figure 1. Cross section (to scale) of the rotational symmetric electrode geometry: (a) positive extraction electrode, (b) center of MOT, (c) negative extraction electrode, (d) einzel lens L1 (consisting of three electrodes including the negative extraction electrode), (e) grounded shielding cone, (f) drift tube 1, (g) einzel lens L2, (h) drift tube 2, (i) einzel lens L3, (j) drift tube 3, (k) einzel lens L4, (l) grounded shielding tube, (m) drift tube 4, (n) MCP shielding, (o) MCP stack.

Table 1. Dimensions of the ion-optical elements. The given distances are meant as clear distance to the preceding element. Front electrodes correspond to electrodes facing towards the MOT, rear electrodes towards the MCP. The labels (a)–(o) refer to figure 1.

Element	Aperture radius	Outer radius	Length	Distance
Positive extraction electrode (a)	—	15 mm	2 mm	—
Negative extraction electrode (c)	6.5 mm	15 mm	5 mm	46 mm
Center electrode of L1 (d)	7 mm	17.5 mm	5 mm	1 mm
Rear electrode of L1 (d)	7.5 mm	22.5 mm	14.5 mm	1 mm
Drift tube 1 (f)	31 mm	32 mm	74 mm	0 mm
Front electrode of L2 (g)	15 mm	52.5 mm	10 mm	0 mm
Center electrode of L2 (g)	15 mm	49 mm	22.5 mm	1 mm
Rear electrode of L2 (g)	15 mm	52.5 mm	10 mm	1 mm
Drift tube 2 (h)	50 mm	51.5 mm	137.5 mm	0 mm
Front electrode of L3 (i)	15 mm	52.5 mm	10 mm	0 mm
Center electrode of L3 (i)	15 mm	49 mm	22.5 mm	1 mm
Rear electrode of L3 (i)	15 mm	52.5 mm	10 mm	1 mm
Drift tube 3 (j)	50 mm	51.5 mm	96.5 mm	0 mm
Front electrode of L4 (k)	40 mm	52.5 mm	10 mm	0 mm
Center electrode of L4 (k)	40 mm	49 mm	60 mm	1 mm
Rear electrode of L4 (k)	40 mm	52,5 mm	10 mm	1 mm
Drift tube 4 (m)	50 mm	51.5 mm	138.5 mm	0 mm
MCP shielding (n)	23.5 mm	51.5 mm	2 mm	0 mm
MCP stack (o)	—	25 mm (20 mm active)	3 mm	3 mm

the drift tube potential. The voltage at the inner electrodes of the einzel lenses can be adjusted to change the focal length of the lens and with that the magnification of the system. In general, a higher voltage leads to a higher magnification. The inner electrode of the first einzel lens is typically held at $U_{L1} = -2.7 \ldots -3$ kV, the inner electrodes of the three other lenses at $U_{L2,3,4} = 0 \ldots 800$ V.

To determine the achievable magnification, we simulated the imaging of ion patterns positioned in the center between the extractor electrodes onto the MCP plane. In figure 2, the magnification of the system depending on the voltages at einzel lens 3 and 4 is shown. The simulations predict the desired magnification of 1000 for a voltage at the einzel lenses 2, 3 and 4 of $U_{L2,3,4} \simeq 750$ V (with $U_{ext} = \pm 500$ V and $U_{L1} = -2700$ V). The time of flight of the ions also varies with electrode voltages and ranges in between 10 and 14 μs.

3. Aberrations and resolution limit

The resolution of an ion-optical system is, in analogy to light optical systems, in general limited by aberrations. In the following section, the types of aberrations that have a relevant influence on our imaging system are covered. Independent of the properties of the ion-optical imaging system, the resolution is limited by the MCP ion detector itself, which has a center-to-center pore distance of 17 μm. Therefore, following the Nyquist–Shannon sampling theorem [38], only structures of size $\geqslant 2 \times 17$ μm can be resolved. Thus, every aberration effect has to be compared to this principal limit.

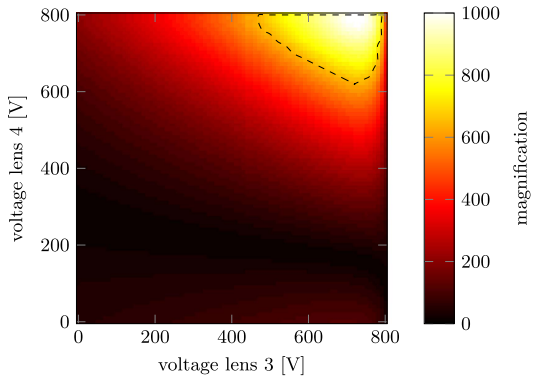

Figure 2. Magnification of the ion optics at the MCP plane for different voltages at the inner electrodes of einzel lens 3 and 4. The remaining parameters were fixed to $U_{ext} = \pm 500$ V, $U_{L1} = -2700$ V and $U_{L2} = +750$ V. All data is derived from a numerical simulation. The sharpest images (smallest point spread function) can be achieved with voltage combinations inside the dashed line. For a sharp image at other magnifications, the voltages at the lenses L1 and L2 have to be adjusted accordingly.

3.1. Spherical aberrations

Spherical aberrations in rotational symmetric lens systems are unavoidable [39], but can be limited by splitting the total refractive power on several lenses, as realized in our microscope. This reduces the angle of incidence of the ion trajectories at each lens and minimizes spherical aberrations. Besides this, thorough optimization of the lens parameters is required to reduce spherical aberrations further.

With the outer lens electrodes being at the same potential as the drift tubes, their length does not play a crucial role for the imaging system. Basically, the refraction takes place in the interspaces between the outer electrodes and the central electrode, where the potential landscape is changing rapidly. The separation between the electrodes has been fixed to 1 mm to ensure a sufficient dielectric strength (see section 4). This leaves the applied voltages, the aperture sizes, and the lengths of the central electrodes for optimization. They all have direct impact on the refractive power of the lens and thus on the focal length and magnification. On the other hand, they strongly influence the spherical abberations.

With the spherical abberations being inverse proportional to the aperture sizes [40], large apertures are generally preferable. For large apertures, however, the focal length and the principal distance of the image plane are increased. This can be partially compensated by increasing the applied voltage to the central electrode. Aperture sizes are thus limited by the target length of the microscope and the maximal applicable voltages. For our imaging system, we limited the size to 700 mm and the voltage difference between neighboring electrodes to 3.2 kV.

The aperture sizes cannot be optimized independently of the lengths of the central electrodes. For increasing electrode length, the focal length and the magnification is reduced. As with the aperture size, the central electrode length has direct influence onto the spherical abberations. They can be minimized by minimizing the gradient of the electrostatic potential along the optical axis at the entrance and exit of the lens. This means that the electrode has to be long compared to the aperture [41]. In our setup, the optimization resulted in a length of the central electrode being typically 50% larger than its aperture radius.

The remaining effects of spherical aberration in our system can be seen in figure 3(a). It shows the focus region of einzel lens 4 for ion trajectories with different starting points. The focal length for off-axis beams is considerably shorter than for beams close to the optical axis.

3.2. Astigmatism and distortion

The effects of astigmatism and distortion are also an inherent feature of einzel lenses [42].

Astigmatism means, that the meridional section (the plane containing the object point and the optical axis) of a beam of rays far away from the optical axis has a different focal length than the sagittal section (the plane perpendicular to the meridional plane). This can lead to a different imaging resolution of the ion optics in sagittal and meridional direction. In figure 3(b), the effect of astigmatism on our ion-optical imaging is visualized: the position of the focal point differs between meridional and sagittal section of the beam. Also the beam radius at the focal point and therefore the resolution of the imaging system is different for the two directions. This effect of directional resolution can also be seen in the simulated imaging of ion test structures in figure 5.

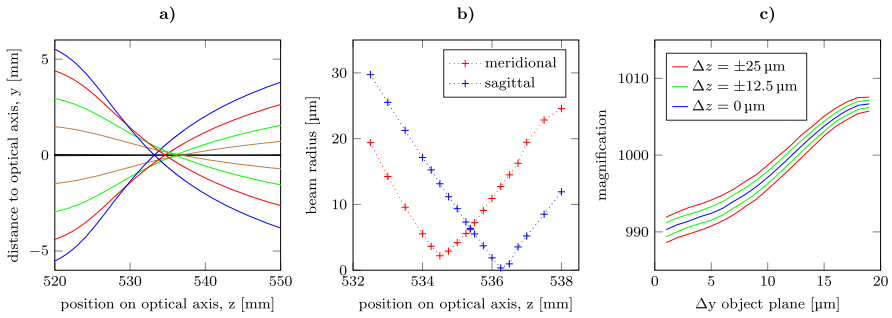

Figure 3. Monochromatic abberations of the ion-optical system at a magnification of 1000. (a) Spherical aberration: ion trajectories near the focus of einzel lens 4. The different lines correspond to different starting distances of the ion to the optical axis (from outer to inner lines: $\Delta y = \pm 19\ \mu$m, $\pm 15\ \mu$m, $\pm 10\ \mu$m, $\pm 5\ \mu$m, ± 100 nm). These result in different focal points and a broadened focus size. (b) Astigmatism: radius of an ion beam starting with a diameter of 100 nm and a distance of 10 μm to the optical axis in meridional and sagittal direction. Depicted is the beam radius after refraction by einzel lens 4. (c) Distortion: magnification as a function of the object distance to the optical axis. Different colors correspond to different object positions along the optical axis.

Distortion means, that the magnification of the optics changes with increasing distance from the optical axis. Its influence is shown in figure 3(c) for different positions of the object plane with respect to the central position between the two extraction electrodes. In principal, the magnification changes by about 1.5% across the image plane, resulting in a superposition of barrel and pincushion distortion.

3.3. Chromatic aberrations

Besides these monochromatic aberrations, there are also chromatic aberrations effecting the imaging quality. In general, the focal length decreases for ions with lower energy, as the refractive power of the lens is increased. This makes the starting energy distribution of the ions to be one of the main sources for chromatic aberrations. For the experiments described here, the ions are produced via photoionization of rubidium atoms out of a continuously operated MOT (see section 4). The starting energy distribution is thus given by the temperature of the MOT, the excess energy (the difference between the photon energy and the ionization energy of rubidium) and the momentum transfer from the photoionization process. The MOT temperature is typically around $T = 100\ \mu$K which corresponds to a particle energy of $E_{\mathrm{kin}} = k_B T = 8.6$ neV. Following energy conservation, the excess energy is distributed on the electron and the ion correspondingly to their mass ratio. With $m_{\mathrm{Rb}^+}/m_e \approx 1.6 \times 10^5$ less than 0.001% of the energy goes to the ion. With the ionization laser being tuned close to the ionization threshold, the excess energy can be very small, in our case 104 μeV, which leads to an energy transfer onto the ion of 0.65 neV. The contribution of the momentum transfer from the photon can be neglected as it is more than one order of magnitude smaller than the other two. This leaves the thermal energy of the particles and the excess energy to be the dominant contribution to the chromatic aberration. Our ion-optical system is designed such that starting energies up to 2.5 μeV will not affect the minimal resolution. This ensures optimal imaging conditions for cloud temperatures up to 30 mK or total excess energies up to 0.4 eV.

3.4. Depth of field

In addition to the chromatic aberration resulting out of the starting energy of the ions, there is also another source of varying ion energy: the ions are not only produced in a plane but in a three dimensional volume. Ions with different starting points along the optical axis experience different accelerations before they reach the first lens. The simulations show, that at a magnification of 1000 the spread of starting positions along the optical axis of the ions can be as big as 50 μm without limiting the resolution to a value worse than the principal limit of the ion detector. At the same time, this value defines the depth of field for our imaging system. The effects are visualized in figure 4(a), showing the relative position shift of ions in the detector plane due to varying starting positions along the optical axis. For starting position shifts $|\Delta z| \leqslant 25\ \mu$m the relative shift in the image plane stays within the pixel size of the MCP detector.

3.5. Modulation transfer function and resolution

In summary, all of the above aberrations limit the final resolution of the ion-optical imaging system. This is typically quantified via the modulation transfer function, describing the contrast in the image plane as function of the point separation in the object plane. Figure 4(b) shows the resulting modulation transfer function for our ion-optical imaging system with the magnification set to 1000 and neglecting the discretization due to the finite

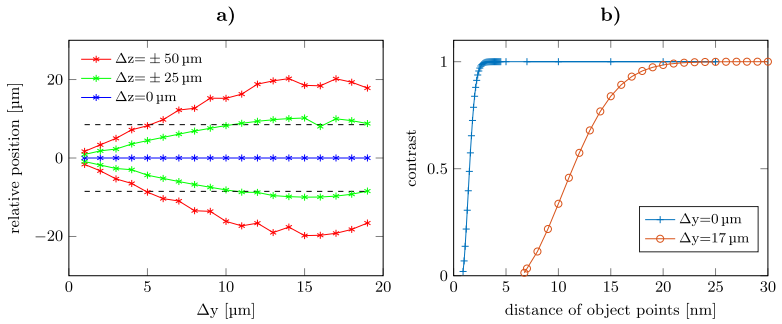

Figure 4. (a) Depth of field: radial position of the ion trajectories at the detector plane for various starting positions along the optical axis Δz and distances to the optical axis Δy in the object plane. $\Delta y = \Delta z = 0$ is the center point between the extraction electrodes. The position is shown relative to the point of incidence of an ion starting at the given Δy but with $\Delta z = 0$ (blue line). The dashed lines depict the MCP pore distance. (b) Modulation transfer function: contrast in the image plane as a function of the point separation in the object plane, for on-axis ($\Delta y = 0$) and off-axis ($\Delta y = 17$ μm) objects. The magnification is set to 1000.

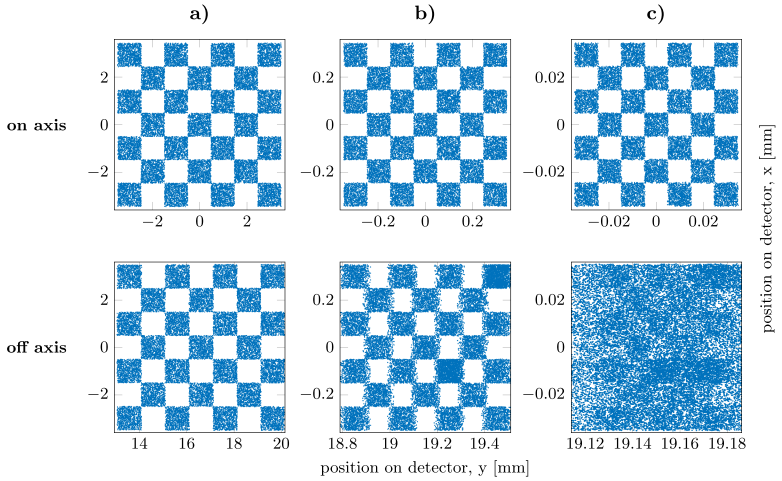

Figure 5. Simulated imaging of several test patterns near (top row) and 19 μm away (bottom row) from the optical axis (ion optics set to a magnification of 1000). The test structures consist of cuboids of different sizes filled with ions: (a) 1 μm $\times$ 1 μm, (b) 100 nm $\times$ 100 nm, (c) 10 nm $\times$ 10 nm. The extent along the optical axis is always 50 μm, the starting energy 9.3 neV.

MCP pore size. The object depth along the optical axis has been chosen to be 25 μm. For on-axis beams, full contrast can be transferred for point separations down to several nanometer. However, off-axis beams are limited to point separations in the 10 nm regime.

The results can be nicely visualized by simulating the imaging of a test pattern (see figure 5). The starting points of the simulated ions are randomly distributed in cuboids of different sizes placed in the center plane between the extraction electrodes. The extension of such a cuboid in the object plane (perpendicular to the optical axis) is small (down to 10 nm) in order to visualize the resolution limit of the ion optics. In contrast to that, the extent along the optical axis is large (50 μm) to show the large depth of field of the system. The starting kinetic energy of each ion is 9.3 neV (see section 3.3) with a random direction of the starting velocity. The trajectories of all ions are simulated and in the ideal case, the spatial distribution should be reproduced on the detector plane with the corresponding magnification. The results in figure 5 show that for structures close to the optical axis the imaging is nearly perfect, but further away from the optical axis, aberrations play a significant role in the imaging quality. With an object depth of $\Delta z = 50$ μm the 100 nm structures can be nicely resolved, however, the 10 nm structures are fully washed out for off-axis patterns. Here, the resolution limit is at about 50 nm.

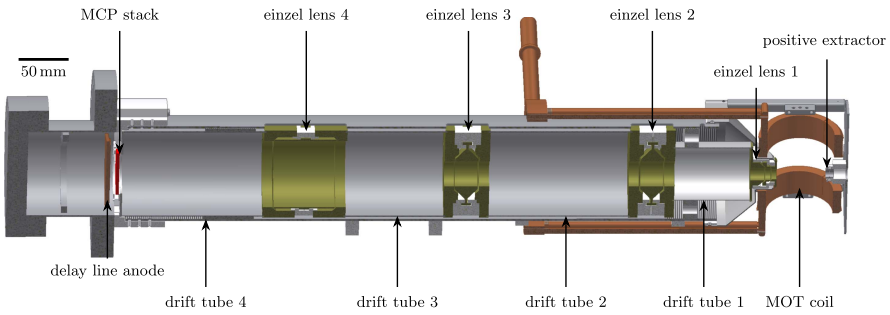

Figure 6. Cross-section of the full ion optics setup inside the vacuum chamber.

3.6. Three-dimensional imaging

As the time of flight of the ion varies with its starting position, it is possible to calculate back from the timing information of the MCP on the initial z-position of the ion. This position along the optical axis is not directly accessible by the imaging. For the procedure to work, the ion has to be inside the depth of field of the imaging system because the time of flight also varies with the starting position in the object plane (x- and y-direction). For the system set to a magnification of 1000, the time of flight increases quadratically with the distance from the image center. It is 200 ns higher at the edge of the image than in the center. If this effect has been taken into account, the residual variation of the time of flight originates from the starting position along the optical axis. This variation is linear and has a gradient between 0.244 and 0.315 μs mm^{-1} depending on the x/y-position of the ion. Therefore, the accuracy of the time of flight measurement has a direct influence on the spatial resolution in z-direction. With a timing resolution of the MCPs time to digital converter (TDC) of <100 ps, the spatial resolution in z-direction is about 400 nm. This is about an order of magnitude higher than the design resolution in x/y-direction. Similar results may be achieved using a movable light sheet for localizing the ionization process along the z-axis.

4. Experimental realization

The complete experimental setup is illustrated in figure 6. It can be divided into three parts: MOT, ion optics and ion detection. All parts are placed in a vacuum chamber under ultra-high vacuum conditions at a pressure of $\sim 1 \times 10^{-10}$ mbar.

The MOT-part (see figure 7) is located between the two extractor electrodes and allows for optical access from several directions. The MOT is created at the minimum of a magnetic quadrupole field generated by a pair of coils in anti-Helmholtz configuration. The magnetic field gradient along the coil axis is 11 G cm^{-1}. The radius of the coils (inside/outside: 34/42 mm) was chosen to be as big as possible to minimize the influence of the coils and their copper holders on the extraction field, while keeping the number of windings and current required for obtaining the field gradient to reasonable values. The laser cooling is provided by three pairs of counterpropagating laser beams which intersect at the magnetic field minimum. The MOT is loaded with rubidium 87 atoms that are provided by current-heated dispensers.

Before imaging the cold atoms, they have to be ionized. This is done by a two-step photoionization process. Using the cooling laser of the MOT, rubidium 87 ground state atoms are first excited from the $5S_{1/2}$, $F = 2$ to the $5P_{3/2}$, $F = 3$ state. Ionization is then achieved via a laser with wavelength of 479.04 nm. The produced Rb^+ ions are then imaged with the ion optics.

The ion optics was built in accordance to the simulated electrostatic lens system. The electrodes were produced out of stainless steel, for insulating parts Macor (a glass-ceramic well suited for UHV conditions) was used. To avoid surface charges on the insulators, which could severely influence the electric field, the electrode geometry was designed in a way that there is no direct connection from any point of the ion beam to the insulator surfaces (see figure 8). In addition, the minimal distance between the electrodes has been limited to 1 mm in vacuum and 7.25 mm at Macor insulators. This ensures a sufficient dielectric strength of about 6 kV [37]. In contrast to all the other electrodes, the positive extractor consists out of transparent glass, coated with 80 nm of indium tin oxide (ITO). By using such a glass electrode, we gain optical access to the MOT parallel to the optical axis of the ion optics while being able to apply a voltage.

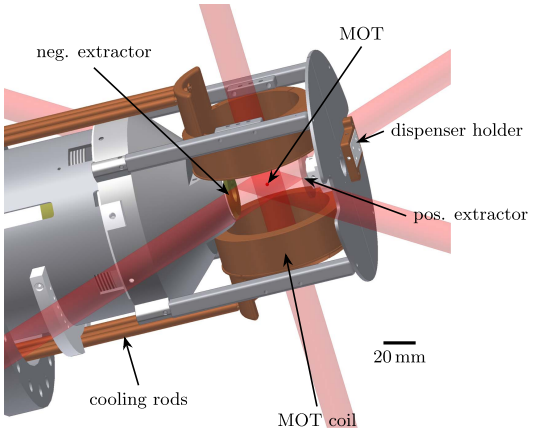

Figure 7. Part of the setup where the magneto-optical trap (MOT) is formed by six intersecting laser beams and a magnetic field formed by two coils.

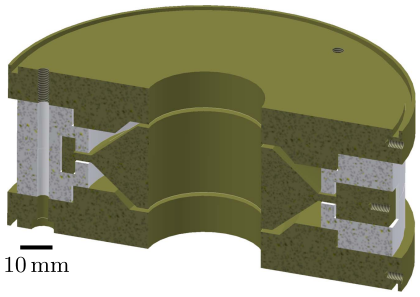

Figure 8. Cross section of einzel lens 3 with stainless steel electrodes (dark) and Macor insulators (light). The distance between two electrode surfaces is 1 mm in vacuum and 7.25 mm at Macor insulators.

The ion detection with high temporal and spatial resolution is done by a combination of a MCP and a DLD [43, 44]. The electrical signals of the DLD are discriminated by a set of constant fraction discriminators and recorded with a TDC. An ion-optical image is typically achieved by accumulating the ion events at the detector for a given amount of time and plotting a histogram of the detected ion positions. The detection efficiency of the system is expected to be mainly given by the MCP, which typically lies in the range of 60%–85% for positive ions with the kinetic energy used in our setup [45].

5. Measurement

In order to prove the ability of our ion optics to image cold atoms, defined test structures have been applied. Therefore, we spatially structured the ionization laser since the photoionization rate is proportional to the laser intensity.

We imaged a resolution test target (USAF1951) illuminated by the ionization laser onto the MOT with an achromatic lens positioned outside the vacuum chamber. The magnification of this light-optical imaging system was $M_L = 1.14$, the optical axis of the imaging is parallel to the optical axis of the ion optics and goes through the ITO coated glass electrode. The test target consists of several groups of elements with varying size. Each element consists of three vertical and three horizontal bars with a distance identical to their width. Obviously, our very simple light-optical projection has a limited quality, so the smallest usable structures has a center-to-center distance of 20 μm at the position of the MOT. Hence, this method is suitable for testing the ion imaging at small magnifications with relatively large structures.

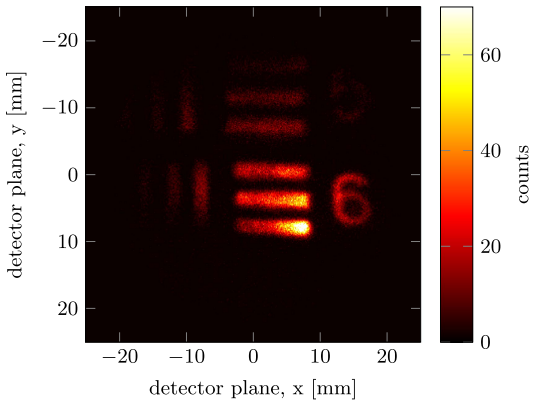

Figure 9. Ion image of a USAF1951 test structure that was projected with the ionization laser onto the MOT. The visible bar structure (number six) has a center to center distance of 80 μm at the position of the MOT. The voltages at the center electrodes of the einzel lenses were $U_{L3} = 300$ V, $U_{L1,2,4} = -2.4$ kV. The magnification is about 50.

To test the imaging of each einzel lens individually, we measured the ion image of a test structure with only one active einzel lens, all the other einzel lenses were 'switched off' by applying the drift-tube voltage of −2.4 kV to the center electrode. At the extraction electrodes, voltages of ±500 V were applied. Because of that, the first einzel lens still has a focussing effect even with the center electrode at −2.4 kV. From the USAF1951 target, we used the structure 6 of group 3, that has a center to center distance of $M_L \cdot 70.16\ \mu\text{m} \approx 80\ \mu\text{m}$. The corresponding image, as measured with our ion microscope at a magnification of 50, is shown in figure 9. It nicely visualizes the original target pattern and yields a distortion free and sharp image. We now imaged this structure for different voltages at the center electrode of the active einzel lens and measured the line distance in the detector image. The results are shown in figure 10 and unveil the voltage dependent magnifications of each einzel lens. All measurements (black) show good agreement to the values extracted from the simulations (red). Only at high voltages, the measurements deviate from the simulations. Partly, this can be explained by inaccuracies in the mechanical assembly, asymmetries and voltage deviations, but it is also likely, that the extraction field in the experiment differs from the simulations. The simulations only consider a rotational-symmetric electrode geometry but in reality, there are also other, non-rotational-symmetric parts that can influence the electric field (for example the MOT-coil holders). Another source for the deviation can be the position of the MOT between the extractor electrodes. In the simulations, the ions start exactly in the center between the extractors, but in the experiment the position of the MOT relative to the extractors cannot be determined exactly.

The USAF1951 target is well suited to characterize the relatively small magnification of a single einzel lens but cannot be used to characterize high magnifications and the resolution limit of the ion optics. For smaller, but still well defined structures, an optical lattice as described in [46] was implemented by superimposing two parallel beams of the ionization laser with a lens onto the MOT. By varying the distance between the parallel beams, the angle between the beams behind the lens and with that the lattice spacing of the emerging interference pattern can be changed. As the beams go through the glass electrode, the maximum beam distance and with that the minimal lattice spacing is limited to about 2.7 μm. With this setup, the predicted magnification of 1000 could be achieved and structures down to the lattice spacing limit could be imaged easily as displayed in figure 11(a). There is a small curvature of the fringes visible, that can be explained by monochromatic aberrations (see figure 3). The fringes are bent in the same direction over the whole image plane and furthermore there is a slight increase in magnification from one side of the detector region to the other, resulting in a changing fringe separation. Both effects indicate, that one or more electrodes are not positioned exactly rotationally symmetric to the optical axis. A line scan of the measurement is depicted in figure 11(b), showing a fringe contrast of 0.32. However, it is difficult to extrapolate a resolution limit out of this contrast, due to the large depth of field of our imaging system. Ions from areas where there is little to no overlap of the beams producing the lattice structure get also imaged onto the detector plane, thus adding an offset to the ion signal. Furthermore, the trajectories of ions produced outside the detection region can get bent back onto the detector. For the future, a reduction of the ionization area to a plane—for example with a light sheet—is advisable. Nevertheless, the 2.7 μm lattice is clearly resolvable, which implies that the actual resolution limit lies lower.

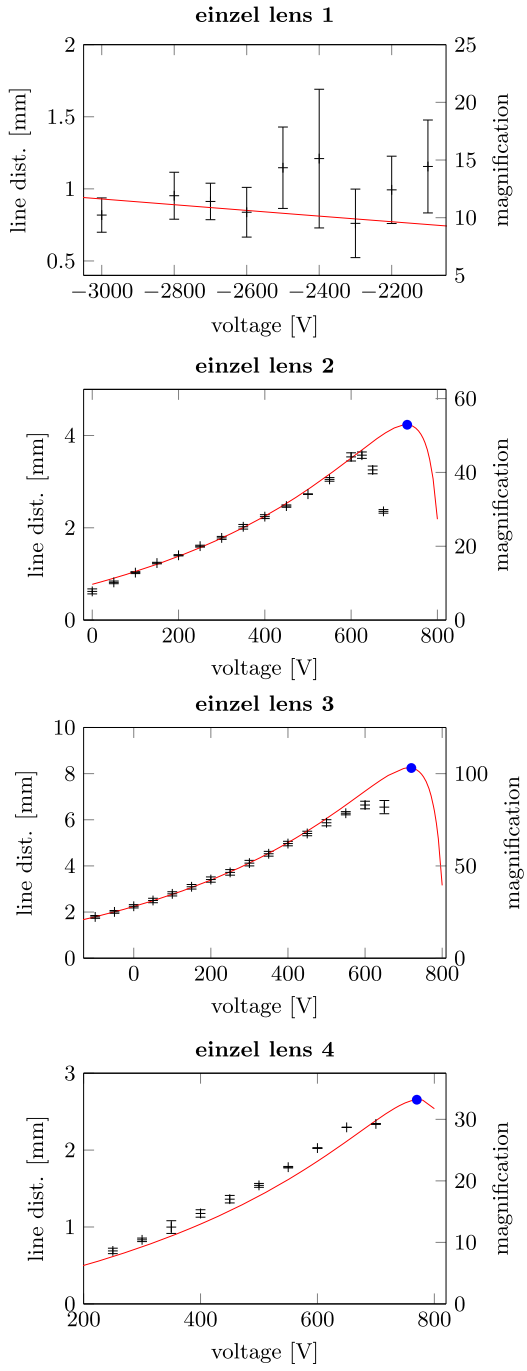

Figure 10. Center to center distance of the test structure from figure 9 on the detector in dependence on the voltage applied to the center electrode of the corresponding einzel lens. The measurement was evaluated by determining the distances between multiple line pairs of the corresponding structure and is shown in black with error bars. The results of the simulation are depicted as solid red lines. The voltage setting for the sharpest image (minimum of the point spread function) is marked with a blue dot (if any). For other settings, the voltage of at least one other lens has to be adapted in order to achieve the sharpest possible image.

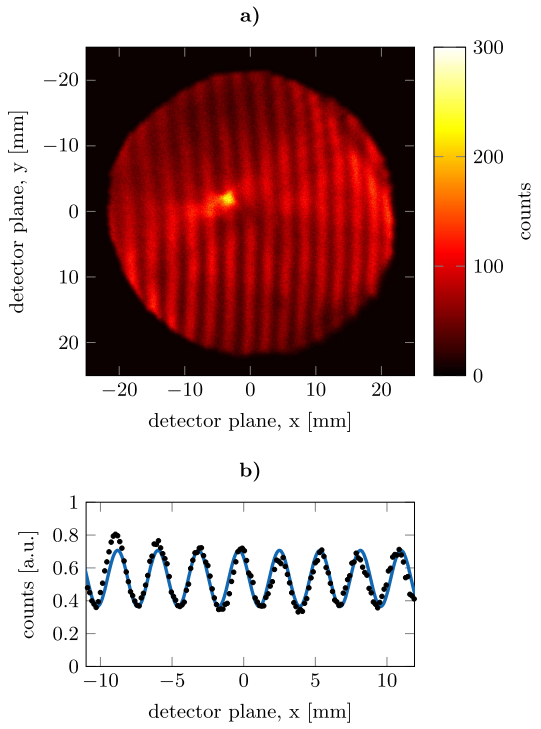

Figure 11. (a) Ion-optical imaging of a MOT onto the MCP with the ionization laser intensity spatially modulated by an interference structure with fringe spacing of 2.7 μm. The magnification is 1050. The bright spot in the middle is produced by ions that are generated outside of the detection region and whose trajectories get bent back into the image. (b) Line scan of the measurement summed up over $y \in$ [11.6 mm, 13.1 mm]. The blue line is a a fit with a sine-function plus offset. The contrast of the fringes (calculated out of the fit) is 0.32.

Testing the ultimate resolution limit of the system would require smaller structures to be imprinted onto the atoms. This could be done by using the standing wave pattern of a retro-reflected ionization laser. In our setup, that would result in a lattice structure with 240 nm fringe spacing. The structure would probably have to be mechanically stabilized to the ion-optical system to minimize the effect of vibrations. Another crucial point is the stability of the voltage sources of the electrodes, especially for ions starting far away from the optical axis. Simulations show that a stability of $\pm 0.05\%$ has to be maintained in order to not limit the resolution of the system. In addition to that, deviations from rotational symmetry can also limit the resolution as well as the characteristics of the delay line signals and detector electronics. As the lattice spacing of the retro-reflective configuration is more than one order of magnitude smaller than the smallest structure demonstrated here, a more promising approach would be to start with structure sizes closer to the demonstrated 2.7 μm. This could be done with a variable standing wave similar to the one we used but with a higher maximum angle between the laser beams, which was not possible in our setup due to limited optical access. Another approach would be to use a different photoionization path involving a wavelength suitable for the desired lattice spacing.

6. Conclusion

In summary, we have presented an ion-optical setup to image and magnify cold atom clouds. The system consists out of four electrostatic lenses and a MCP for ion detection. Simulations show, that the resolution should be better than 100 nm with a maximum magnification of 1000. Therefore, it surpasses standard light optical imaging techniques. The ion optics was realized experimentally and integrated into a cold atom setup. It was characterized by photoionization of atoms out of a MOT. The results are in good agreement with the simulations and show, that the system can be used to study ultracold atom clouds.

Although, the ion microscope was demonstrated here on a continuously operated MOT, it can be easily applied to investigate ultracold quantum gases and Bose–Einstein condensates. Then, the microscope can be

operated in a quasi non-destructive mode by ionizing only a small subset of particles. If this subset resembles the whole quantum gas, global properties like atom number, density and temperature can be extracted from the ion microscope. With the microscope being able to operate continuously, also the observation of dynamical processes in quantum gases, like vortices, solitons, collective excitations or oscillations come into direct reach. Furthermore, the system should be well suited to investigate local statistics in quantum gases via temporal and spatial correlation analysis. Such correlation measurements become even more important in the context of Rydberg gases, where many-body effects like the Rydberg blockade [47, 48], facilitation [49], crystallization [50] or molecule formation [51] could be directly observed. The cold atom microscope is thus perfectly suited to investigate physics beyond the standard mean-field approach.

Acknowledgments

We gratefully acknowledge financial support from Deutsche Forschungsgemeinschaft through SFB TRR21 and SPP1929/GiRyd (FO 740/2-1), from Baden-Württemberg Stiftung through 'Kompetenznetz Funktionelle Nanostrukturen' and from FET-Open Xtrack Project HAIRS. MS acknowledges financial support from Landesgraduiertenförderung Baden-Württemberg. The authors would also like to thank C Zimmermann and P Federsel for helpful discussions and C Billington for assistance during the set-up of the experiment.

References

[1] Chu S, Hollberg L, Bjorkholm J E, Cable A and Ashkin A 1985 *Phys. Rev. Lett.* **55** 48
[2] Anderson M H, Ensher J R, Matthews M R, Wieman C E and Cornell E A 1995 *Science* **269** 198
[3] Davis K B, Mewes M O, Andrews M R, van Druten N J, Durfee D S, Kurn D M and Ketterle W 1995 *Phys. Rev. Lett.* **75** 3969
[4] DeMarco B and Jin D S 1999 *Science* **285** 1703
[5] Ketterle W, Durfee D S and Stamper-Kurn D M 1999 **140** 67
[6] Andrews M R, Mewes M-O, van Druten N J, Durfee D S, Kurn D M and Ketterle W 1996 *Science* **273** 84
[7] Higbie J M, Sadler L E, Inouye S, Chikkatur A P, Leslie S R, Moore K L, Savalli V and Stamper-Kurn D M 2005 *Phys. Rev. Lett.* **95** 050401
[8] Meppelink R, Rozendaal R A, Koller S B, Vogels J M and van der Straten P 2010 *Phys. Rev.* A **81** 053632
[9] Bakr W S, Gillen J I, Peng A, Fölling S and Greiner M 2009 *Nature* **462** 74
[10] Sherson J F, Weitenberg C, Endres M, Cheneau M, Bloch I and Kuhr S 2010 *Nature* **467** 68
[11] Bakr W S, Peng A, Tai M E, Ma R, Simon J, Gillen J I, Folling S, Pollet L and Greiner M 2010 *Science* **329** 547
[12] Edge G J A, Anderson R, Jervis D, McKay D C, Day R, Trotzky S and Thywissen J H 2015 *Phys. Rev.* A **92** 063406
[13] Cheuk L W, Nichols M A, Okan M, Gersdorf T, Ramasesh V V, Bakr W S, Lompe T and Zwierlein M W 2015 *Phys. Rev. Lett.* **114** 193001
[14] Haller E, Hudson J, Kelly A, Cotta D A, Peaudecerf B, Bruce G D and Kuhr S 2015 *Nat. Phys.* **11** 738
[15] Greif D, Parsons M F, Mazurenko A, Chiu C S, Blatt S, Huber F, Ji G and Greiner M 2016 *Science* **351** 953
[16] Troyer M and Wiese U-J 2005 *Phys. Rev. Lett.* **94** 170201
[17] Parsons M F, Mazurenko A, Chiu C S, Ji G, Greif D and Greiner M 2016 *Science* **353** 1253
[18] Gallagher T F 1994 *Rydberg Atoms* (Cambridge: Cambridge University Press)
[19] McQuillen P, Zhang X, Strickler T, Dunning F B and Killian T C 2013 *Phys. Rev.* A **87** 013407
[20] Urban E, Johnson T A, Henage T, Isenhower L, Yavuz D D, Walker T G and Saffman M 2009 *Nat. Phys.* **5** 110
[21] Gaëtan A, Miroshnychenko Y, Wilk T, Chotia A, Viteau M, Comparat D, Pillet P, Browaeys A and Grangier P 2009 *Nat. Phys.* **5** 115
[22] Schauss P, Cheneau M, Endres M, Fukuhara T, Hild S, Omran A, Pohl T, Gross C, Kuhr S and Bloch I 2012 *Nature* **490** 87
[23] Stibor A, Bender H, Kühnhold S, Fortágh J, Zimmermann C and Günther A 2010 *New J. Phys.* **12** 065034
[24] Günter G, Robert-de Saint-Vincent M, Schempp H, Hofmann C S, Whitlock S and Weidemüller M 2012 *Phys. Rev. Lett.* **108** 013002
[25] Karlewski F, Mack M, Grimmel J, Sándor N and Fortágh J 2015 *Phys. Rev.* A **91** 043422
[26] Claessens B J, Reijnders M P, Taban G, Luiten O J and Vredenbregt E J D 2007 *Phys. Plasmas* **14** 093101
[27] Hanssen J L, Hill S B, Orloff J and McClelland J J 2008 *Nano Lett.* **8** 2844
[28] Reijnders M P, van Kruisbergen P A, Taban G, van der Geer S B, Mutsaers P H A, Vredenbregt E J D and Luiten O J 2009 *Phys. Rev. Lett.* **102** 034802
[29] McCulloch A J, Sheludko D V, Saliba S D, Bell S C, Junker M, Nugent K A and Scholten R E 2011 *Nat. Phys.* **7** 785
[30] McCulloch A J, Sheludko D V, Junker M and Scholten R E 2013 *Nat. Commun.* **4** 1692
[31] Schwarzkopf A, Sapiro R E and Raithel G 2011 *Phys. Rev. Lett.* **107** 103001
[32] Schwarzkopf A, Anderson D A, Thaicharoen N and Raithel G 2013 *Phys. Rev.* A **88** 061406
[33] van Bijnen R M W, Ravensbergen C, Bakker D J, Dijk G J, Kokkelmans S J J M F and Vredenbregt E J D 2015 *New J. Phys.* **17** 023045
[34] Gericke T, Würtz P, Reitz D, Langen T and Ott H 2008 *Nat. Phys.* **4** 949
[35] Manthey T, Weber T M, Niederprüm T, Langer P, Guarrera V, Barontini G and Ott H 2014 *New J. Phys.* **16** 083034
[36] Schellekens M, Hoppeler R, Perrin A, Gomes J V, Boiron D, Aspect A and Westbrook C I 2005 *Science* **310** 648
[37] Drummond I W 1984 *Vacuum* **34** 51
[38] Shannon C E 1949 *Proc. IRE* **37** 10
[39] Scherzer O 1936 *Z. Phys.* **101** 593
[40] Szilagyi M 1986 *Appl. Phys. Lett.* **49** 767
[41] Sise O, Ulu M and Dogan M 2005 *Nucl. Instrum. Methods Phys. Res.* A **554** 114
[42] Klemperer O 1953 *Electron Optics* (Cambridge: Cambridge University Press)
[43] Sobottka S E and Williams M B 1988 *IEEE Trans. Nucl. Sci.* **35** 348
[44] Friedman P G, Cuza R A, Fleischman J R, Martin C, Schiminovich D and Doyle D J 1996 *Rev. Sci. Instrum.* **67** 596
[45] Wiza J L 1979 *Nucl. Instrum. Methods* **162** 587
[46] Li T C, Kelkar H, Medellin D and Raizen M G 2008 *Opt. Express* **16** 5465
[47] Singer K, Reetz-Lamour M, Amthor T, Marcassa L G and Weidemüller M 2004 *Phys. Rev. Lett.* **93** 163001

[48] Tong D, Farooqi S M, Stanojevic J, Krishnan S, Zhang Y P, Côté R, Eyler E E and Gould P L 2004 *Phys. Rev. Lett.* **93** 063001
[49] Lesanovsky I and Garrahan J P 2014 *Phys. Rev.* **90** 011603
[50] Schauss P, Zeiher J, Fukuhara T, Hild S, Cheneau M, Macri T, Pohl T, Bloch I and Gross C 2015 *Science* **347** 1455
[51] Bendkowsky V, Butscher B, Nipper J, Shaffer J P, Löw R and Pfau T 2009 *Nature* **458** 1005

B. Publication [2]

Reprint with permission of the American Physical Society.

PHYSICAL REVIEW A **96**, 013427 (2017)

Ionization spectra of highly Stark-shifted rubidium Rydberg states

Jens Grimmel,* Markus Stecker,† Manuel Kaiser, Florian Karlewski, Lara Torralbo-Campo, Andreas Günther, and József Fortágh‡

Center for Quantum Science, Physikalisches Institut, Eberhard-Karls-Universität Tübingen, Auf der Morgenstelle 14, D-72076 Tübingen, Germany

(Received 21 March 2017; published 26 July 2017)

We report on the observation and numerical calculation of ionization spectra of highly Stark-shifted Rydberg states of rubidium beyond the classical ionization threshold. In the numerical calculations, a complex absorbing potential (CAP) allows us to predict the energy levels and ionization rates of Rydberg states in this regime. Our approach of adjusting the CAP to the external electric field reduces the number of free parameters from one per resonance to a single one. Furthermore, we have measured the ionization spectra of magneto-optically trapped rubidium atoms which are excited to principal quantum numbers of 43 and 70 at various electric fields. The emerging ions are detected using an ion optics. We find good agreement between the numerically and experimentally obtained spectra.

DOI: 10.1103/PhysRevA.96.013427

I. INTRODUCTION

Stark spectra of alkali-metal Rydberg states above the classical ionization threshold exhibit an intricate energy-level structure with strongly varying ionization behavior, including rapidly ionizing states as well as the extreme of narrow resonances where ionization is almost suppressed [1]. The latter feature is clearly distinct from hydrogen, where the ionization rate of a given state grows exponentially with the applied external electric field [2]. The study of these ionization spectra of nonhydrogenic atoms is therefore of particular interest not only from a fundamental point of view, but also for the prospect of improved control over the ionization process in Rydberg gases.

The method of complex rotation (CR) is well known for the theoretical treatment of ionization rates of highly Stark-shifted states of hydrogen and alkali atoms [3–5]. It is applied by substituting the location and momentum operators in the Hamiltonian by the complex terms $\hat{r} \rightarrow \hat{r} \cdot \exp(i\theta)$ and $\hat{p} \rightarrow \hat{p} \cdot \exp(-i\theta)$, respectively, which results in a non-Hermitian Hamiltonian. This leads to complex eigenvalues of the Hamiltonian which can be used to obtain the energy levels and linewidths, i.e., the ionization rates in the present case. As an alternative to this method, a complex absorbing potential (CAP) can be employed to create a non-Hermitian Hamiltonian [6–9]. The CAP is added to the original Hamiltonian in the form $-i\eta W(\vec{r})$. Both of these methods, CR and CAP, work with free parameters θ and η, respectively, which are determined for every single resonance of the system by a variational method.

In a previous work [10] we have calculated Stark-shifted energy levels including the corresponding dipole matrix elements by diagonalization of a matrix representation of the Hamiltonian [11]. While this methods yields very precise results for spectra at electric fields below the classical ionization threshold, the broadening of the states by ionization at higher fields can no longer be neglected. Hence, in this work, we combine the matrix diagonalization method with an adaptive CAP method by choosing a potential that is adjusted to the external electric field. This removes the need to determine the free parameter η for each resonance separately and thereby greatly reduces the computational effort for the numerical calculation. We calculate ionization spectra near the unperturbed $43S_{1/2}$ and $70S_{1/2}$ ^{87}Rb Rydberg states for electric fields far beyond the classical ionization threshold. Furthermore, we present an experiment in which rubidium atoms in a magneto-optical trap (MOT) are excited to Rydberg states in the presence of an external electric field. When the atoms ionize from these Stark-shifted Rydberg states, the ions are guided to a detector by an ion-optical system [12]. We have measured ionization spectra by ramping up the external electric field and scanning the excitation laser frequency near the aforementioned states.

The methods we present here can be used to search for resonances from the ionization spectra, such as highly Stark-shifted states which have a desirable ionization rate or sensitivity to the external electric field across a certain range. Furthermore, this opens up the possibility to tune a coupling between ionizing and nonionizing states by the external electric field. This way of tailoring the ionization process is highly useful for the design of sources of cold ions and electrons for microscopy purposes [13–16]. Moreover, a precise knowledge of these ionization spectra opens new perspectives for experiments incorporating Rydberg atoms near surfaces, where static electric fields arise due to adsorbates [17–20].

II. APPLICATION OF A COMPLEX ABSORBING POTENTIAL

The Hamiltonian $\hat{H}$ for an atom in an external electric field F_E along the z axis is given by

$$\hat{H} = \hat{H}_0 + F_E \hat{z}, \tag{1}$$

where $\hat{H}_0$ denotes the unperturbed Hamiltonian, i.e., the unperturbed atomic energy levels, which are calculated from quantum defect theory [21–24]. Note that all formulas in this

*jens.grimmel@uni-tuebingen.de
†markus.stecker@uni-tuebingen.de
‡fortagh@uni-tuebingen.de

section are given in atomic units. The Stark-shifted energy levels corresponding to this Hamiltonian are routinely calculated by choosing a subset of the basis given by $\hat{H}_0$, representing $\hat{H}$ as a matrix in this basis and computing the eigenvalues of this matrix [11]. For the high-field region considered in this work, it is crucial to include all total angular momentum quantum numbers j in the subset of the basis. However, as we use a two-photon excitation scheme in the experiment, we can limit our calculations to $|m_j| \in \{1/2,3/2,5/2\}$. The subset of the basis is then chosen symmetrically in energy above and below the desired energy region. The convergence of this method can be assured by increasing the subset of the basis until changes of the resulting eigenvalues are well below the experimental resolution. In our previous work, we have extended the calculations of [11] and determined a measure D for the transition strength in the three-level ladder scheme by calculating the dipole matrix elements between the states [10]. Here, we further extend these calculations by introducing a complex absorbing potential (CAP) to the model, which allows for an estimate of the ionization rates of Stark-shifted states in the regime of high electric fields beyond the classical ionization threshold.

The CAP is added to the Hamiltonian $\hat{H}$, resulting in a new non-Hermitian Hamiltonian,

$$\hat{H}_{\mathrm{CAP}} = \hat{H} - i\eta W(\hat{r}, F_{\mathrm{E}}). \tag{2}$$

In general, the free parameter $\eta \in \mathbb{R}^+$ should be adjusted for each resonance that is studied at each value of the electric field. However, in the approach we present in this work, we also adjust the function $W(\hat{r}, F_{\mathrm{E}})$ depending on the electric field, which in effect allows us to choose the parameter η only once for a whole region of the spectrum.

We have chosen a CAP combining $\hat{r}^6$ as in Ref. [8] with the Heaviside function Θ as in Ref. [7], similar to the rectangular-box CAP in Ref. [25]:

$$W(\hat{r}, F_{\mathrm{E}}) = \Theta[\hat{r} - r_{\mathrm{c}}(F_{\mathrm{E}})][\hat{r} - r_{\mathrm{c}}(F_{\mathrm{E}})]^6. \tag{3}$$

This results in a spherical potential scaling as $\hat{r}^6$, but radially shifted to a radius r_{c}. The matrix representation of this CAP is calculated using the same radial wave functions as for the $\hat{z}$ operator, which are obtained by integrating a parametric model potential [26]. It is worth noting that due to its spherical symmetry, this choice for the CAP does not introduce any coupling between different states and therefore results in a purely diagonal matrix representation. Furthermore, the Hamiltonian can still be treated separately for different values of $|m_j|$ and the basis for the matrix representation is chosen as in previous works by including enough states nearby in energy for the results to converge [10,11].

The potential $W(\hat{r}, F_{\mathrm{E}})$ is changed along with the external electric field F_{E} via the radius r_{c}. To determine r_{c}, we use a Coulomb potential to approximate the atomic potential with an external electric field,

$$V_{\mathrm{C,E}} = -\frac{1}{r} - F_{\mathrm{E}} z. \tag{4}$$

This potential is also used for the definition of the classical ionization threshold, which is given by

$$E_{\mathrm{ion}} = -2\sqrt{F_{\mathrm{E}}}, \tag{5}$$

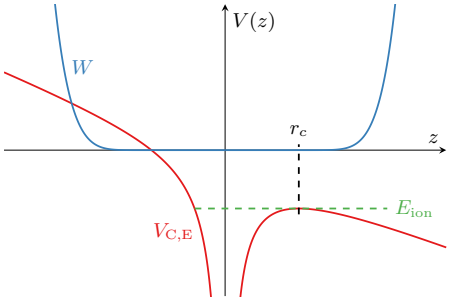

FIG. 1. Illustration of the complex absorbing potential (CAP). The parameter r_{c} is determined according to Eq. (6) which places it at the radius of the saddle point of the potential $V_{\mathrm{C,E}}$ [see Eq. (4)]. Note that in this 1D graph along the z axis, the saddle point appears as a local maximum. This choice of r_{c} creates a potential W that resembles the shape of r^6 but is spherically shifted by r_{c}.

and marks the saddle point where the potential opens towards the continuum. The location of the saddle point, which is a local maximum along the z axis, is then given by

$$r_{\mathrm{c}}(F_{\mathrm{E}}) = \frac{1}{\sqrt{F_{\mathrm{E}}}}, \tag{6}$$

and we use this radius to place the onset of r^6 in the potential $W(\hat{r}, F_{\mathrm{E}})$, as illustrated in Fig. 1. Graphically speaking, this allows us to distinguish between an inside and an outside region of the atom and to ensure that the CAP only absorbs the parts of the wave functions that protrude to the outside region.

The Hamiltonian $\hat{H}_{\mathrm{CAP}}$ may yield complex eigenvalues which can be written as

$$E_{\mathrm{c}} = E_r - i\frac{\Gamma}{2}, \tag{7}$$

where the real part determines the energy level E_r of the resonance and the imaginary part determines its ionization rate Γ. In the calculations, the free parameter η from Eq. (2) is varied for exemplary values of the electric field. The first of these exemplary points is conveniently chosen near the classical ionization threshold to determine a first estimate for η because, assuming no other previous knowledge about the spectrum, this region generally features a large number of resonances with different ionization rates. Subsequently, further points are chosen at higher electric fields to continue the variation of η following the initial estimate. The parameter η is then fixed to a value in the center of a region which leaves the resulting eigenvalues E_c mostly unchanged. For all spectra investigated here, this region spans multiple orders of magnitude of η, which is a direct consequence of our field-dependent choice for the CAP. It is also worth noting that within this region, changes of η affect the broadest resonances, i.e., broader than the frequency range in the experiment, more than narrow resonances. Therefore, the resulting changes do not visibly alter the spectrum.

In order to create a diagram of the spectrum from the calculated eigenvalues in terms of intensity I with respect to the transition energy E, we sum up Lorentzian peaks for

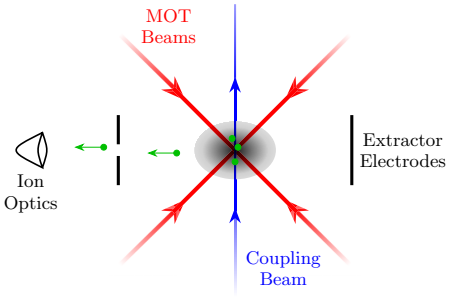

FIG. 2. Schematic diagram of the experimental setup. Rubidium atoms are trapped at the intersection of the MOT beams (red). Atoms from the MOT are continuously excited to Rydberg states by the coupling laser (blue) at various electric fields, which are applied via the extractor electrodes. The field is also used to guide the ions (green) to the ion optics.

each resonance at a given electric field,

$$I(E) = \frac{D}{\pi}\frac{\Gamma}{\Gamma^2 + (E - E_r)^2}. \tag{8}$$

For the resulting resonances which would have linewidths smaller than 25 MHz, we set the linewidth to 25 MHz, which is approximately the linewidth of resonances in the region that is not dominated by ionization and also the resolution of our experimental data. Please note that ionization is the only decay channel that we consider in these calculations. All other decay channels as well as redistribution by blackbody radiation are negligible for strongly ionizing states.

III. EXPERIMENTAL SETUP

We excite Rydberg atoms in a cloud of ^{87}Rb atoms confined to a standard six-beam magneto-optical trap (MOT). The cooling light is provided by a diode laser running at ≈780 nm, which is frequency stabilized to the cooling transition $5S_{1/2}(F = 2) \rightarrow 5P_{3/2}(F = 3)$ with a red detuning of 10 MHz. The MOT is positioned in between two electrodes which are used both to generate the desired electric field at the position of the MOT and to extract ions out of the MOT (see Fig. 2). An ion optics consisting of a set of electrostatic lenses guides the ions to a microchannel plate detector (MCP) where they can be detected with single-particle sensitivity [12].

The excitation of rubidium atoms from the ground state to a Rydberg level is done in a two-step process. The lower transition $5S_{1/2} \rightarrow 5P_{3/2}$ is driven by the MOT beams themselves. The upper transition from the intermediate state $5P_{3/2}$ to a Rydberg level is done by a frequency-doubled, grating stabilized diode laser (Toptica DL-SHG pro) with a tuneable wavelength around 480 nm (hereafter referred to as "coupling laser"). The frequency of the coupling laser is stabilized by a HighFinesse WSU-30 Wavemeter. The ionization rate of the excited Rydberg atoms is determined by counting the emerging ions with the MCP detector.

In order to measure the ionization spectra of highly Stark-shifted Rydberg states, we fix the coupling laser to a certain frequency and ramp the voltage at the extractor electrodes to probe the desired field region and simultaneously detect the generated ions. This ramp is repeated for different coupling laser frequencies. The MOT beams and the coupling beam remain switched on during the whole measurement and the MOT is continuously loaded from rubidium dispensers. With this scheme, we were able to scan a large field region in a reasonably small measurement time, while still getting a good signal-to-noise ratio.

We measured Stark spectra near the unperturbed $43S_{1/2}$ and $70S_{1/2}$ state in a wide electric-field range, mostly around and above the classical ionization limit. In these measurements, we used voltage ramps with a ramping speed of 1 V/s and 25 MHz steps for the frequency of the coupling laser.

IV. MEASUREMENTS AND COMPARISON TO CAP-THEORY RESULTS

We present experimental results in comparison to results from our numerical calculations near the unperturbed state $43S_{1/2}$ in Fig. 3. The experimental resolution of the voltage was 100 mV, equivalent to 30.6 mV/cm, and the step size of the electric field in the numerical calculations was 40 mV/cm. The classical ionization threshold for this state is at ≈127 V/cm, so it is located just within the lower limit of the electric-field range of this figure. The variation of the free parameter η described in Sec. II led to a value of $\eta = 1\times10^6$ in the depicted region and we used ≈4000 states for the matrix representation of $\hat{H}_{\mathrm{CAP}}$. The results from the experiment and numerical calculations are in very good agreement. Both data sets clearly show a general broadening of the lines with increasing electric field as one would naively expect above the classical ionization threshold. However, we also find some resonances which are still narrow even at high electric fields as well as overlapping narrow and broad resonances, for example at ≈143 V/cm in Figs. 3(a) and 3(b).

The results near the unperturbed state $70S_{1/2}$ are depicted in Figs. 4–7. The experimental results were recorded with a resolution of 50 mV, equivalent to 15.4 mV/cm, and the numerical calculation was performed using steps of 10 mV/cm. The ionization threshold near this state is within the range of Fig. 4 at ≈16.1 V/cm. In this region, the variation of the free parameter η resulted in a value of $\eta = 2\times10^5$ and the matrix for $\hat{H}_{\mathrm{CAP}}$ is represented using ≈10 000 states. Again, we find a general broadening of the resonances beyond the classical ionization threshold. This broadening increases as the electric field gets stronger, but even in the high-field range of Fig. 6 we still find some narrow resonances with linewidths on the order of magnitude of our experimental resolution of 25 MHz.

In the highest-field range (see Figs. 6 and 7), the larger ionization rates result in overlapping resonances with different linewidths. In some parts of these spectra, the results from the numerical calculations deviate from the experimental results showing antiresonancelike features instead of resonances, e.g., in Fig. 7(a), where such a feature starts at 30.5 V/cm near −1 GHz and crosses the whole frequency range of the recorded spectrum up to 31 V/cm and 2 GHz. These parts of the spectra, where we find deviations from Lorentzian line shapes, may be interpreted as Fano resonances [27]. A Fano-type resonance arises due to interference between different excitation paths to an ionized continuum state. Such Fano resonances have

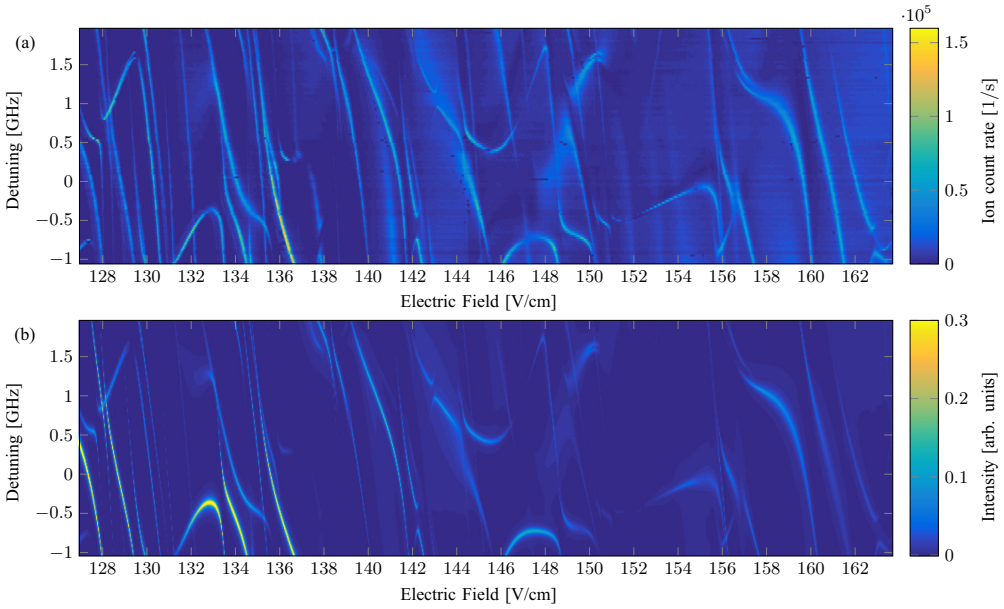

FIG. 3. Ionization Stark spectrum near $43S_{1/2}$. (a) Detected ion signal from the experiment. (b) Results from the numerical calculations for $\eta = 1\times10^6$. The detuning is given relative to the unperturbed state. We have applied a linear scaling to match the electric field from the experiment to the theoretical results. The classical ionization threshold is located at $\approx$127 V/cm.

been observed previously in similar systems [28–30]. In the present case, besides the discrete Rydberg state that decays to a continuum state by autoionization, there is also the possibility of direct photoionization. Furthermore, several overlapping Rydberg resonances with possibly different ionization rates may lead to more complicated interference effects and thereby

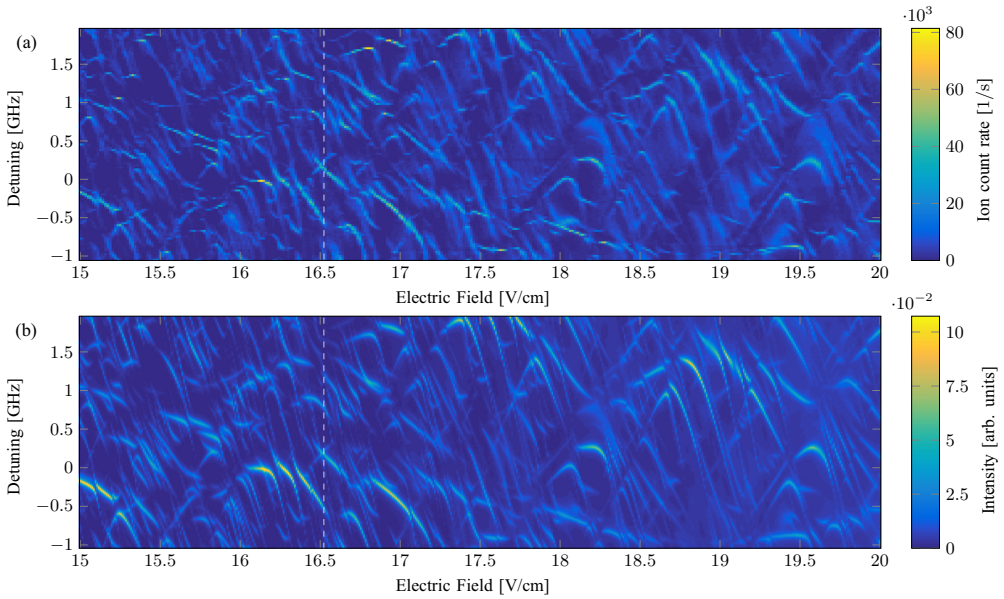

FIG. 4. Ionization Stark spectrum near $70S_{1/2}$. (a) Detected ion signal from the experiment. (b) Results from the numerical calculations for $\eta = 2\times10^5$. The detuning is given relative to the unperturbed state. We have applied a linear scaling to match the electric field from the experiment to the theoretical results. The classical ionization threshold is located at $\approx$16.1 V/cm. The white dashed lines mark the cut that is shown in more detail in Fig. 8(a).

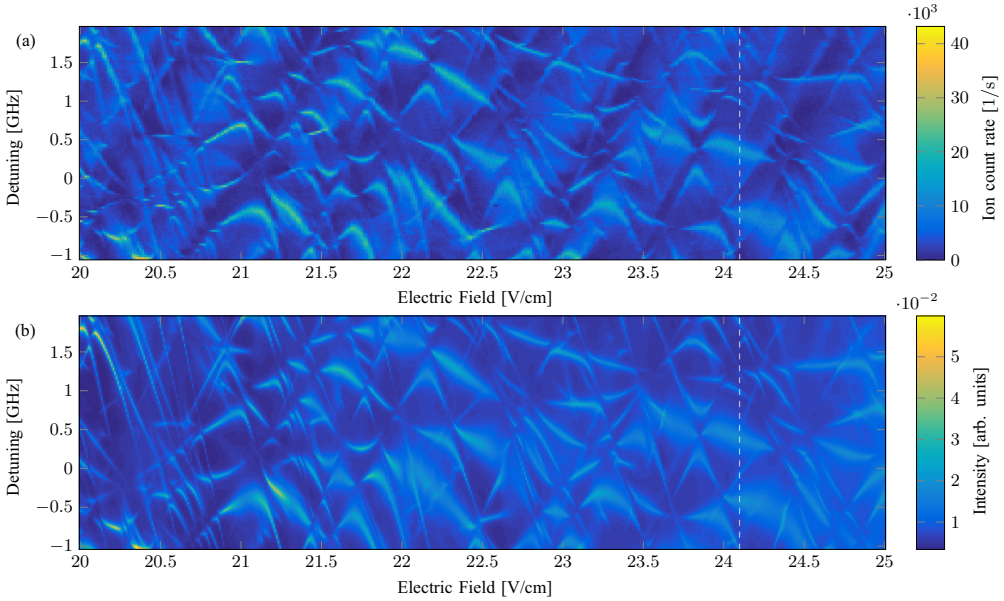

FIG. 5. Ionization Stark spectrum near $70S_{1/2}$. Continuation from Fig. 4. The white dashed lines mark the cut that is shown in more detail in Fig. 8(b).

more convoluted spectral features. A complete study of these possible Fano resonances may yield a more accurate prediction of the spectrum, but is beyond the scope of this work.

The numbers of states that were used for the matrix representations of the Hamiltonians were determined in order to calculate a dataset which is bigger than what is shown in this work. We estimate that ≈3000 and ≈6000 states should be enough to reproduce our results near $43S_{1/2}$ and $70S_{1/2}$, respectively. Therefore, all results from the numerical calculations are well converged in the regions depicted in Figs. 3–7. Some discrepancies between the results may arise from slow drifts of the voltage source that was used in the experiment. Since the measurement was performed for one

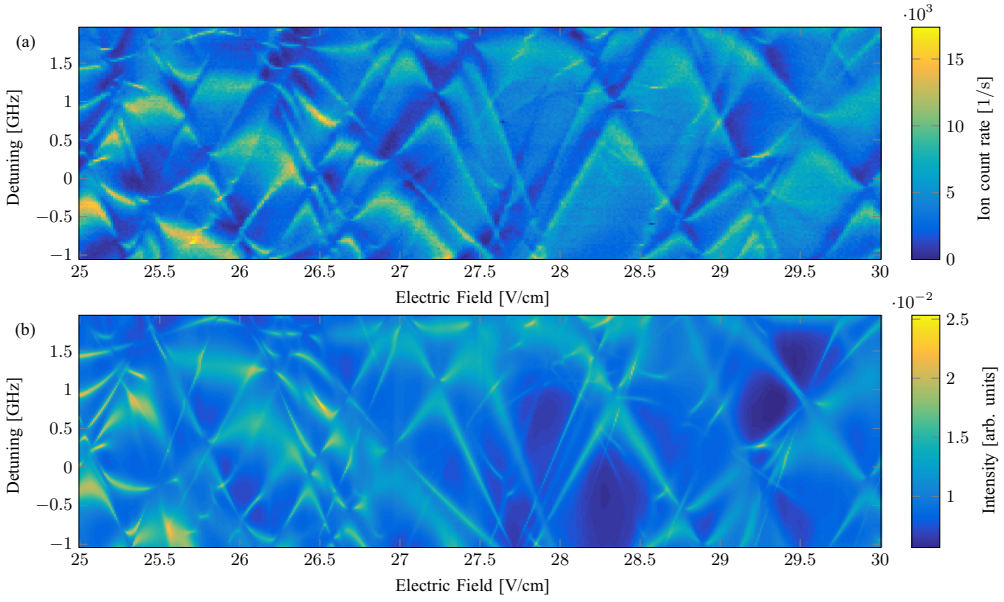

FIG. 6. Ionization Stark spectrum near $70S_{1/2}$. Continuation from Fig. 5.

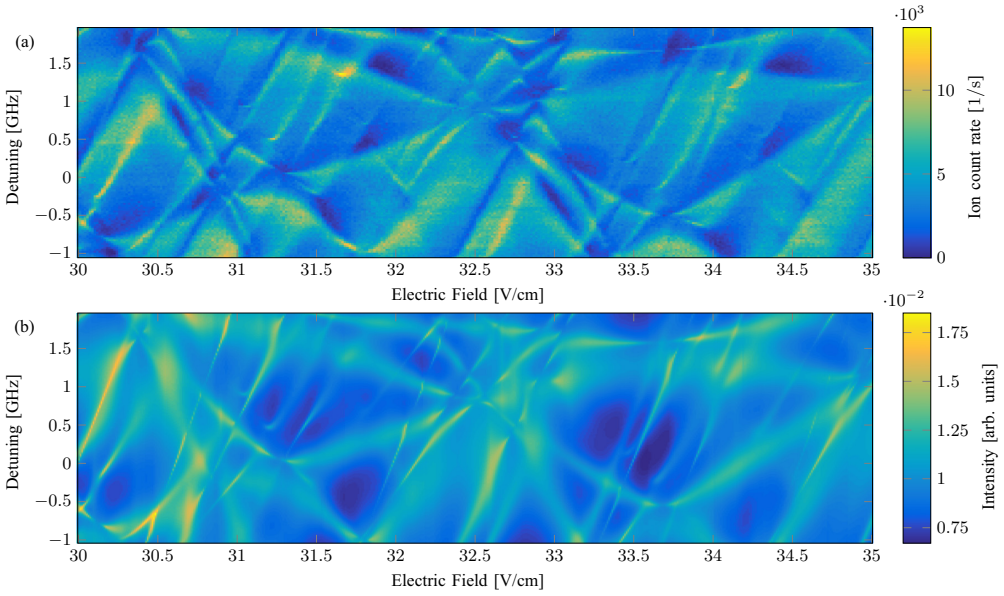

FIG. 7. Ionization Stark spectrum near $70S_{1/2}$. Continuation from Fig. 6.

horizontal line in the data after the other, this results in a horizontal mismatch of the experimental data of up to ± 0.05 V/cm in comparison to the numerically calculated results. Another minor source of deviations between the results may arise since the detection efficiency in the experiment changes as the extractor voltage is increased. Therefore, the ion counts we obtain from the experiment do not scale directly to the results for the intensity from the numerical simulations on the whole range simultaneously. However, this effect is small for the figures presented here since the color maps have been rescaled for each electric-field range separately.

For a more detailed analysis of the results from the experiment and the numerical calculations, we present cuts of the spectra at two different values of the electric field from Figs. 4 and 5 in Fig. 8. The data shown in Fig. 8(a) corresponds to an external electric field of 16.53 V/cm, i.e., just above the classical ionization threshold. In this region, the peak positions and widths of the experimentally detected and numerically calculated ionization spectra agree within our experimental frequency resolution of 25 MHz. For the higher electric field of 24.10 V/cm shown in Fig. 8(b), we find that the shapes of the two resonances with the highest intensities deviate slightly, namely, by an asymmetry of the experimentally obtained signals. We see these asymmetries as another possible manifestation of Fano resonances in this system. Further deviations in the region between 1.3 and 2 GHz can be mapped to an electric-field region of ± 0.05 V/cm and are caused by drifts of the voltage source, as discussed before, in combination with the high sensitivity of these particular resonances to the external electric field (see Fig. 5).

V. CONCLUSION

In this work, we have implemented an extension of the CAP method, in which we alter the shape of the complex

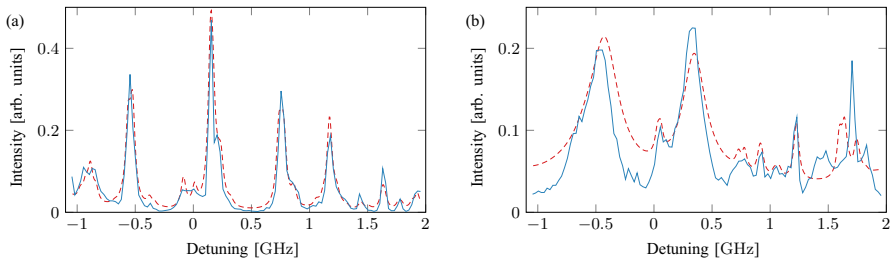

FIG. 8. Ionization Stark spectra from the experiment (blue solid lines) and the numerical calculations (red dashed lines) near $70S_{1/2}$ at (a) 16.53 V/cm (see Fig. 4) and (b) 24.10 V/cm (see Fig. 5). While we find agreement within our experimental resolution of 25 MHz in (a), some small deviations can be seen in (b). The two highest peaks from the experimental data in (b) have a slightly asymmetric line shape, which may indicate possible Fano resonances. Furthermore, we find discrepancies around 1.3–2 GHz, which we attribute to drifts of the voltage source that was used in the experiment and the high sensitivity of these resonances to the electric field.

absorbing potential according to the change of the external electric field. Furthermore, we have presented experimental results from a setup in which rubidium atoms are continuously ionized through Rydberg states in the presence of an external electric field. Our experimental data show the existence of rich ionization spectra with sharp resonances even far beyond the classical ionization threshold. The presented numerical calculations are capable of predicting the measured spectra of highly Stark-shifted Rydberg states, including the sharp resonances. Thus it is suitable for improving control over the excitation to such states and the subsequent ionization process. An in-depth theoretical study of the possible Fano resonances that we have observed in the experimental data may improve this control even further.

ACKNOWLEDGMENTS

This work was financially supported by the EU FET-Open Xtrack Project HAIRS and by Deutsche Forschungsgemeinschaft through SFB TRR21 and SPP 1929 (GiRyd). M.S. acknowledges financial support from Landesgraduiertenförderung Baden-Württemberg. We thank P. Schmelcher for advice on complex rotation methods. We thank N. Schopohl and N. Sándor for helpful discussions.

[1] T. F. Gallagher, *Rydberg Atoms*, 1st ed. (Cambridge University Press, Cambridge, 1994).
[2] R. J. Damburg and V. V. Kolosov, J. Phys. B **12**, 2637 (1979).
[3] W. P. Reinhardt, Int. J. Quantum Chem. **10**, 359 (1976).
[4] W. P. Reinhardt, Annu. Rev. Phys. Chem. **33**, 223 (1982).
[5] G. D. Stevens, C.-H. Iu, T. Bergeman, H. J. Metcalf, I. Seipp, K. T. Taylor, and D. Delande, Phys. Rev. A **53**, 1349 (1996).
[6] R. Kosloff and D. Kosloff, J. Comput. Phys. **63**, 363 (1986).
[7] U. V. Riss and H. D. Meyer, J. Phys. B **26**, 4503 (1993).
[8] S. Sahoo and Y. K. Ho, J. Phys. B **33**, 2195 (2000).
[9] Y. K. Ho, Few-Body Syst. **54**, 31 (2013).
[10] J. Grimmel, M. Mack, F. Karlewski, F. Jessen, M. Reinschmidt, N. Sándor, and J. Fortágh, New J. Phys. **17**, 053005 (2015).
[11] M. L. Zimmerman, M. G. Littman, M. M. Kash, and D. Kleppner, Phys. Rev. A **20**, 2251 (1979).
[12] M. Stecker, H. Schefzyk, J. Fortágh, and A. Günther, New J. Phys. **19**, 043020 (2017).
[13] L. Kime, A. Fioretti, Y. Bruneau, N. Porfido, F. Fuso, M. Viteau, G. Khalili, N. Šantić, A. Gloter, B. Rasser, P. Sudraud, P. Pillet, and D. Comparat, Phys. Rev. A **88**, 033424 (2013).
[14] D. Murphy, R. E. Scholten, and B. M. Sparkes, Phys. Rev. Lett. **115**, 214802 (2015).
[15] D. J. Thompson, D. Murphy, R. W. Speirs, R. M. W. van Bijnen, A. J. McCulloch, R. E. Scholten, and B. M. Sparkes, Phys. Rev. Lett. **117**, 193202 (2016).
[16] E. Moufarej, M. Vielle-Grosjean, G. Khalili, A. J. McCulloch, F. Robicheaux, Y. J. Picard, and D. Comparat, Phys. Rev. A **95**, 043409 (2017).
[17] A. Tauschinsky, R. M. T. Thijssen, S. Whitlock, H. B. van L. van den Heuvell, and R. J. C. Spreeuw, Phys. Rev. A **81**, 063411 (2010).
[18] R. P. Abel, C. Carr, U. Krohn, and C. S. Adams, Phys. Rev. A **84**, 023408 (2011).
[19] H. Hattermann, M. Mack, F. Karlewski, F. Jessen, D. Cano, and J. Fortágh, Phys. Rev. A **86**, 022511 (2012).
[20] K. S. Chan, M. Siercke, C. Hufnagel, and R. Dumke, Phys. Rev. Lett. **112**, 026101 (2014).
[21] W. Li, I. Mourachko, M. W. Noel, and T. F. Gallagher, Phys. Rev. A **67**, 052502 (2003).
[22] M. Mack, F. Karlewski, H. Hattermann, S. Höckh, F. Jessen, D. Cano, and J. Fortágh, Phys. Rev. A **83**, 052515 (2011).
[23] J. Han, Y. Jamil, D. V. L. Norum, P. J. Tanner, and T. F. Gallagher, Phys. Rev. A **74**, 054502 (2006).
[24] K. Afrousheh, P. Bohlouli-Zanjani, J. A. Petrus, and J. D. D. Martin, Phys. Rev. A **74**, 062712 (2006).
[25] R. Santra and L. S. Cederbaum, J. Chem. Phys. **115**, 6853 (2001).
[26] M. Marinescu, H. R. Sadeghpour, and A. Dalgarno, Phys. Rev. A **49**, 982 (1994).
[27] U. Fano, Phys. Rev. **124**, 1866 (1961).
[28] S. Feneuille, S. Liberman, J. Pinard, and A. Taleb, Phys. Rev. Lett. **42**, 1404 (1979).
[29] T. S. Luk, L. DiMauro, T. Bergeman, and H. Metcalf, Phys. Rev. Lett. **47**, 83 (1981).
[30] D. A. Harmin, Phys. Rev. A **26**, 2656 (1982).

C. Manuscript [3]

Controlling the dipole blockade of highly Stark-shifted rubidium Rydberg states

Markus Stecker,[1,*] Jens Grimmel,[1] Raphael Nold,[1] Malte Reinschmidt,[1] József Fortágh,[1] and Andreas Günther[1,†]

[1] *Center for Quantum Science, Physikalisches Institut, Eberhard Karls Universität Tübingen, Auf der Morgenstelle 14, D-72076 Tübingen, Germany*

(Dated: February 26, 2018)

We report on a novel technique for tuning the dipole-dipole interaction of Rydberg atoms. Therefore, we make use of highly Stark-shifted states in electric fields above the classical ionization limit. We show the existence of states with low ionization rates in this field regime and observe excitation blockade with different blockade radii depending on the electric dipole moment of the state. We have developed a detection scheme for controlled ionization and magnified imaging of those states with high spatial and temporal resolution by adiabatic transfer to a state with a suitable ionization rate.

Rydberg systems exhibit strong correlations due to electrostatic interactions between the highly excited atoms. This property makes them a promising candidate for quantum information processing [1, 2] and quantum simulation [3]. The interaction can be of van der Waals or dipole-dipole type [4] and manifests itself in the so called Rydberg blockade, where, in the presence of a first excitation, a second excitation is suppressed. The efficiency of the blockade and thus the fidelity of a blockade-based quantum gate depends on the strength of the Rydberg-Rydberg interaction [5, 6]. For quantum simulators, a tunable interaction potential is highly desirable. Consequently, following the first measurement of the Rydberg blockade [7, 8], efforts have been undergone to enhance and tune the interaction for example by tuning a state with a small electric field to a Förster resonance [9–11], using a state with a near resonant dipole-dipole interaction at zero field [12], the AC Stark shift [13], Rotary echo [14] or a small DC electric field [15–17]. Coherent collective Rydberg excitation in the strong blockade regime has been achieved [18] as well as blockade between two individiual atoms [19, 20]. A two-qubit CNOT gate and entanglement between pairs of atoms via the blockade interaction has been demonstrated [21–23] and a quantum Ising model out of single Rydberg atoms has been realized [24]. Spatially resolved measurement of the Rydberg blockade has been studied with separate excitation areas [25, 26], quantum gas microscopes [27, 28], interaction enhanced imaging [29, 30] and direct spatially resolved imaging by field ionization [31–34].

In this work, we investigate Rydberg-Rydberg interactions in an electric field region close to the classical ionization limit, which is typically not considered adequate for this kind of experiment. We identify states at high electric fields with high transition dipole moments and low ionization rates suitable for observing blockade effects. We show that we can tune the interaction strength by small changes in the external electric field and observe Rydberg blockade of different blockade radii. Therefore, our work substantially advances the possibilities to control the interaction strength of Rydberg atoms and can prove to be useful for realizing interaction potentials for quantum simulators that vary in space and time. Furthermore, we implement a detection scheme in which the excited Rydberg atoms are ionized by adiabatic transfer to a state with a defined ionization rate. Spatially resolved detection is achieved by imaging the ions with a high resolution ion microscope for cold atoms [35].

The energy landscape of highly Stark-shifted Rydberg atoms exhibits an intricate form [36] and is governed by strongly varying line broadening due to ionization. Nevertheless, as predicted by numerical calculations [37], we find states, which are mostly unaffected by ionization and have a varying dipole-dipole interaction strength. In order to choose a suitable state for spatially resolved detection of Rydberg atoms, we aim for states which undergo a rapid change in their ionization rate, changing from a few kilohertz to about 1 MHz within around 1 V/cm. This way, we can transfer the excited state with a small change of the electric field to an ionizing state with a defined ionization rate. Typically, Rydberg atoms are ionized by simply switching the electric field to a much higher value. In contrast, our approach realizes a very controlled way of ionization. We can choose a state with an ionization rate that is on the one hand high enough that the atoms do not move or decay significantly before they get ionized, but on the other hand low enough that saturation of the ion detector is avoided. Besides this technical advantage, our ionization method also allows for a reversal of this transfer, bringing the ionizing state back to the original state. This is virtually impossible when switching to a much higher field, because during the time evolution through the Stark map, the state gets redistributed over many Stark-shifted states [38].

Our experimental setup consists of a vacuum setup with a standard magneto-optical trap (MOT) for ^{87}Rb with 10^7 atoms at a temperature of 150 µK. The spatially resolved detection of ions out of the MOT is done with an ion microscope composed of four consecutive electrostatic lenses and an MCP in conjunction with a delay line detector for electronic readout of the individual ion positions and time stamps. The MOT is positioned between two extractor electrodes which can be used to generate the desired electric field at the position of the atoms. For

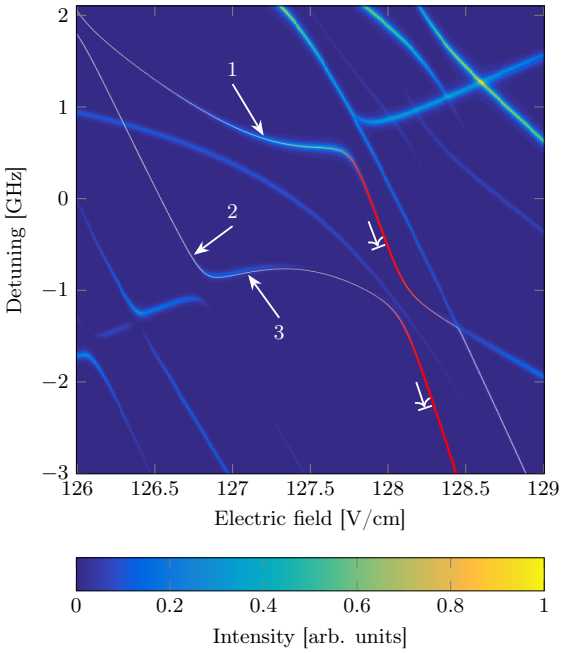

FIG. 1. Numerically calculated Stark spectrum of ^{87}Rb [37]. The detuning is given relative to the unperturbed $43S_{1/2}$ state (classical ionization limit of 127.2 V/cm). The colorplot shows transition strength and linewidth of the resonances. The solid lines depict the ionization rates of the two states that were used in the experiment from nonionizing (white) to strongly ionizing (red). The arrowheads with delimiters mark the ionizing state that the Rydberg state is transferred to for detection.

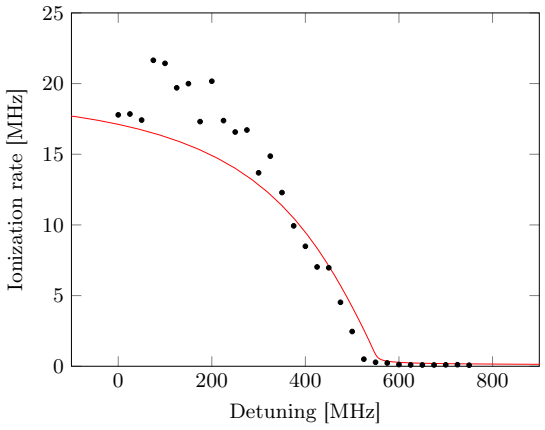

FIG. 2. Measured (black dots) and calculated (solid red line) ionization rates following the line containing resonance 1 (see Fig. 1). Deviations between theory and experiment arise from the fact that the free parameter of the CAP potential was optimized for a broad spectral range and not for a single resonance.

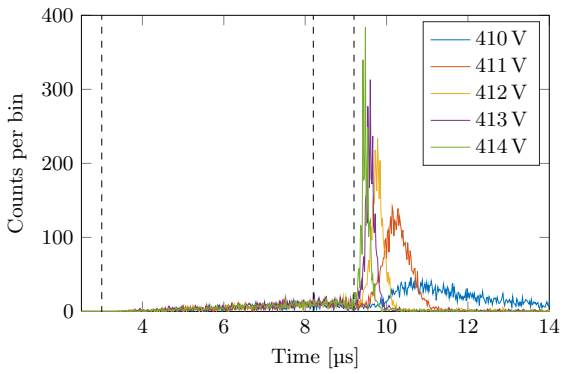

FIG. 3. Histogram of ion arrival times for different final values of the extractor voltage (bin size of 20 ns, sum over 500 excitation pulses for each curve). The first two dashed vertical lines depict the Rydberg excitation pulse (duration of 5 µs), the third line shows the start of the electric-field ramp (transition time ≈ 1 µs). With increasing voltage, the ionization occurs earlier and faster.

details about the experimental setup see [35]. Typically, the magnification of the ion microscope is around 1000, resulting in an imaging area of 40 µm diameter. Rydberg atoms are excited via a two-photon transition from the $5S_{1/2}$ state via the intermediate $5P_{3/2}$ state to a Rydberg state. The lower transition at around 780 nm is provided by the cooling lasers of the MOT. The beam for the upper transition at about 480 nm is directed perpendicular to the optical axis of the ion imaging. The laser is frequency stabilized by a HighFinesse Wavelength Meter WS-U2. The blue beam going into the vacuum chamber is focused to a light sheet with beam waists of 9 µm and 80 µm, respectively, in order to limit the excitation depth in the direction of the ion-optical axis while still having high light intensity in the imaging area.

In order to demonstrate the applicability of our excitation and detection scheme, we first validate the predictions of our numerical calculation [37] experimentally. The calculations make use of a complex absorbing potential [39–41] to predict ionization spectra of highly Stark-shifted Rydberg states. The results for a small energy region corresponding to the unperturbed $43S_{1/2}$ state and an electric field of 126-129 V/cm can be seen in Fig. 1 (the corresponding classical ionization limit is 127.2 V/cm). We picked this region because there are two resonance lines present that undergo a strong change in ionization rate from non-ionizing to strongly ionizing. To measure the ionization rates, we excite Rydberg atoms at different points along the resonance line with a blue laser pulse of 1 - 5 µs duration (depending on the transition strength) and simultaneously detect the arrival time of the ions reaching the detector. The lower transition is provided by the MOT-lasers which are con-

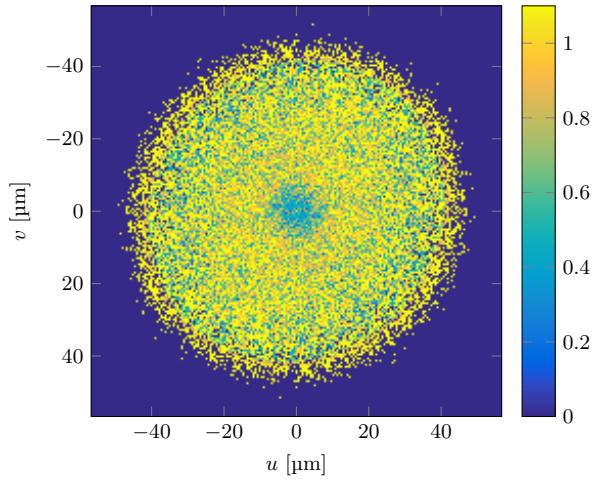

FIG. 4. Spatial correlation function $g^{(2)}(u, v)$ when exciting resonance 1 of Fig. 1. The Rydberg blockade effect manifests itself by a decrease of $g^{(2)}$ to values smaller than 1 for interatomic separations smaller than the blockade radius.

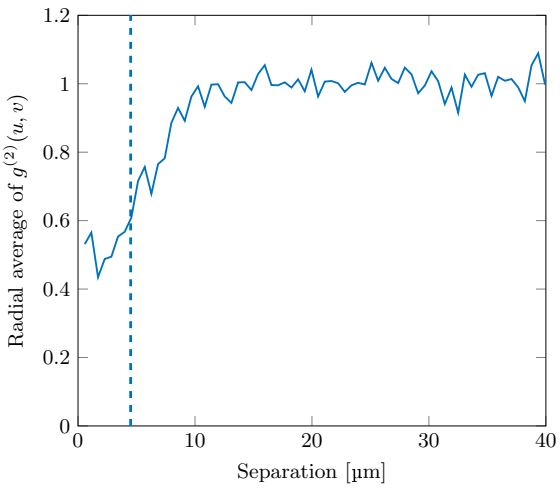

FIG. 5. Radial average of $g^{(2)}(u, v)$ for excitation of resonance 1. The dashed line depicts the blockade radius calculated following Eq. 3.

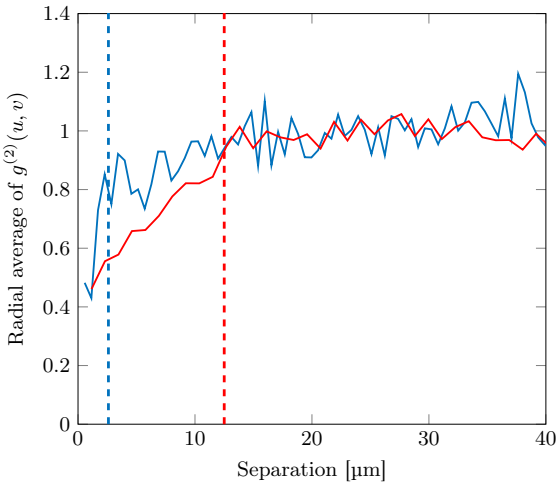

FIG. 6. Radial average of $g^{(2)}(u, v)$ for excitation of resonances 2 (red, large blockade radius) and 3 (blue, small blockade radius). The dashed lines depict the blockade radii calculated following Eq. 3.

tinuously on during the experiment. With one excitation pulse typically yielding 1-30 ions depending on the transition strength of the resonance, the excitation pulse is repeated several thousand times. A histogram of the arrival times is derived and the ionization rate of the state can be determined by the decay of the ion signal after the end of the excitation pulse assuming other decay and ionization channels to be negligible. Radiative decay to lower states and redistribution to higher and lower states by black body radiation can alter the ionization rate to both higher and lower values. Since the lifetimes of Rydberg atoms are in general tens of microseconds [42] and the redistribution by black body radiation is in the kHz regime [43], we do not expect a major influence of these mechanisms on our measurements. However, it has to be pointed out that in the strongly Stark-shifted regime, the redistribution could differ from the zero-field case. Nevertheless, the experimental data shows good agreement with the results from the numerical calculation (see Fig. 2).

For the spatially resolved detection of Rydberg atoms we now set electric field and laser frequency to a slowly ionizing state and pulse the blue laser. After the excitation, the voltage at the extractor electrodes is ramped up by around 1 V/cm in order to transfer the Rydberg atoms to an ionizing state. A high voltage switch is used to change the electric field with a transition time of $\approx 1\,\mu s$. Time of flight and position of the ions hitting the detector are recorded. The excitation-detection-cycle is repeated up to several thousand times. Each pulse typically yields 2-8 ions. In Fig. 3, the effect of different end values for the extractor voltages is shown (the transition times remain unchanged). The ionization takes place faster for atoms transferred to a state with higher ionization rate. Furthermore, the onset of ionization shifts to earlier values since the atoms start ionizing before the end value is reached. We excite the three resonances depicted with arrows and numbers in Fig. 1 and choose the end value of the extractor voltage such that the Rydberg population gets ionized within 1 µs. For resonance 1, the excitation is done at an electric field of 127.2 V/cm and a laser detuning of 686 MHz (with respect to the unperturbed

43S state). For ionization, the field is then switched to $\approx 128\,\mathrm{V/cm}$. For exciting resonance 2, the electric field is set to $126.7\,\mathrm{V/cm}$ and the laser detuning to $-614\,\mathrm{MHz}$. For resonance 3, the electric field is $127.1\,\mathrm{V/cm}$ and the detuning $-794\,\mathrm{MHz}$. The ionization of these two states is done by switching the field to $\approx 128.3\,\mathrm{V/cm}$. The magnification of the ion-optical system was set to 1129.

For each pulse, the two-dimensional spatial second order correlation function

$$g^{(2)}(u,v) = \frac{\langle\langle f(x+u,y+v)f(x,y)\rangle\rangle_{x,y}}{\langle\langle f(x+u,y+v)\rangle\rangle_{x,y}\langle\langle f(x,y)\rangle\rangle_{x,y}}, \quad (1)$$

is calculated with the detector function $f(x,y)$, displacements u,v and the average over x and y position $\langle\langle\cdot\rangle\rangle_{x,y}$. The detector function can be written as

$$f(x,y) = \sum_{i=1}^{N} \delta(x-x_i)\delta(y-y_i), \quad (2)$$

with the coordinates x_i, y_i of the N incoming ions on the detector after one excitation pulse. The correlation results for the individual pulses are summed up. In order to account for the spatially inhomogeneous excitation efficiency (due to inhomogeneous laser power) and the influence of the finite detector size, the result is normalized to the correlation function calculated from all events of the different pulses at once. In the resulting signal (Figs. 4, 5 and 6), an excitation blockade manifests itself in a decreased (< 1) correlation function in a certain region around the origin. In order to characterize the blockade by a blockade radius, the radial mean of $g^{(2)}$ is calculated by radial binning and averaging of the results from $g^{(2)}(u,v)$.

For resonance 1, the blockade effect starts at an interatomic distance of 9 µm, for resonance 2 at 12 µm and for resonance 3 at 2 µm. For $r \to 0$, the value of $g^{(2)}$ does not reach zero because our excitation area is not perfectly two dimensional. The strong blockade effect of resonances 1 and 2 show that even in this high electric-field regime, which is normally governed by ionization, we can observe Rydberg-Rydberg interaction. When we compare the results for resonances 2 and 3 which are both part of the same resonance line, we see that we can drastically alter the interaction strength by a small change of the electric field.

As a theoretical value for the blockade radius, we define the distance r_b at which the energy shift ΔW due to the interatomic interaction equals the excitation laser linewidth $\delta\nu_L$:

$$2\pi\hbar\delta\nu_L = \Delta W(r_b). \quad (3)$$

We estimate $\delta\nu_L \approx 5\,\mathrm{MHz}$ for our experiment. The energy shift due to dipole-dipole interactions is

$$\Delta W = \frac{1}{4\pi\epsilon_0}\frac{p_z^2}{R^3}\left(1-3\cos^2\Theta\right), \quad (4)$$

with the permanent electric dipole moment p_z (electric field in z-direction), the interatomic distance R and the angle between R and z-axis Θ. The light sheet is oriented perpendicular to the optical axis of the ion imaging system and the electric field of the extractor electrodes points along the optical axis, so we assume $\Theta = \pi/2$. The dipole moment p_z of a Stark-shifted state in an electric field F with energy $E(F)$ can be determined by evaluating the slope of the resonance line $-dE(F)/dF$.

We find $r_b = 4.5\,\mu\mathrm{m}$ for resonance 1, $12.5\,\mu\mathrm{m}$ for resonance 2 and $2.6\,\mu\mathrm{m}$ for resonance 3, as depicted in Figs. 5 and 6 via the dashed vertical lines. We see that the decrease of the $g^{(2)}$ correlation function for resonances 2 and 3 in Fig. 6 fit nicely to the calculated blockade radii resulting from dipole-dipole interaction. The slope at resonance 2 in the Stark map is big (see Fig. 1), the resulting dipole moment is $1.90 \cdot 10^{-26}\,\mathrm{Cm}$. This high value leads to a strong dipole-dipole interaction resulting in a large blockade radius. In contrast to that, we have a small slope at resonance 3 with a small dipole moment of $1.76 \cdot 10^{-27}\,\mathrm{Cm}$ leading to a weak excitation blockade. For resonance 1, the calculated blockade radius of $4.5\,\mu\mathrm{m}$ ($p_z = 4.19 \cdot 10^{-27}\,\mathrm{Cm}$) does not match the measured value. The decrease of the radial average of the correlation function in Fig. 5 starts at $\approx 9\,\mu\mathrm{m}$. Besides the dipole-dipole interaction there is also a second-order van der Waals interaction which could lead to the observed blockade. Furthermore, the interaction could be enhanced by resonant energy transfer [4].

In summary, we have shown that the Rydberg blockade can be observed at highly Stark-shifted states and is tunable by small changes in the electric field. In many experiments, residual electric fields are present, especially when atoms are brought close ($< 100\,\mu\mathrm{m}$) to surfaces where adsorbates play a crucial role [44–47]. These small distances are often necessary, for example to reach the strong coupling regime of atoms coupled to a coplanar superconducting resonator [48, 49]. Typically, the fields have to be compensated by a set of electrodes to account for all directions which can be challenging and cumbersome. Instead of trying to reach a zero field condition, we have shown in our work that the complicated "spaghetti region" of the Stark spectrum with its diversity of states can be seen as an advantage instead of an annoyance and represents the opportunity for tailoring excitation, interaction and ionization of Rydberg states.

This work was financially supported by Deutsche Forschungsgemeinschaft through SPP 1929 (GiRyd). M.S. acknowledges financial support from Landesgraduiertenförderung Baden-Württemberg.

* markus.stecker@uni-tuebingen.de
† a.guenther@uni-tuebingen.de

[1] D. Jaksch, J. I. Cirac, P. Zoller, S. L. Rolston, R. Côté, and M. D. Lukin, Phys. Rev. Lett. **85**, 2208 (2000).
[2] M. D. Lukin, M. Fleischhauer, R. Cote, L. M. Duan, D. Jaksch, J. I. Cirac, and P. Zoller, Phys. Rev. Lett. **87**, 037901 (2001).
[3] H. Weimer, M. Müller, I. Lesanovsky, P. Zoller, and H. P. Büchler, Nature Physics **6**, 382 (2010).
[4] A. Reinhard, T. C. Liebisch, B. Knuffman, and G. Raithel, Phys. Rev. A **75**, 032712 (2007).
[5] M. Saffman and T. G. Walker, Phys. Rev. A **72**, 022347 (2005).
[6] X. L. Zhang, A. T. Gill, L. Isenhower, T. G. Walker, and M. Saffman, Phys. Rev. A **85**, 042310 (2012).
[7] D. Tong, S. M. Farooqi, J. Stanojevic, S. Krishnan, Y. P. Zhang, R. Côté, E. E. Eyler, and P. L. Gould, Phys. Rev. Lett. **93**, 063001 (2004).
[8] K. Singer, M. Reetz-Lamour, T. Amthor, L. G. Marcassa, and M. Weidemüller, Phys. Rev. Lett. **93**, 163001 (2004).
[9] T. Vogt, M. Viteau, J. Zhao, A. Chotia, D. Comparat, and P. Pillet, Phys. Rev. Lett. **97**, 083003 (2006).
[10] A. Reinhard, K. C. Younge, T. C. Liebisch, B. Knuffman, P. R. Berman, and G. Raithel, Phys. Rev. Lett. **100**, 233201 (2008).
[11] S. Ravets, H. Labuhn, D. Barredo, L. Béguin, T. Lahaye, and A. Browaeys, Nat. Phys. **10**, 914 (2014).
[12] A. Reinhard, K. C. Younge, and G. Raithel, Phys. Rev. A **78**, 060702 (2008).
[13] P. Bohlouli-Zanjani, J. A. Petrus, and J. D. D. Martin, Phys. Rev. Lett. **98**, 203005 (2007).
[14] N. Thaicharoen, A. Schwarzkopf, and G. Raithel, Phys. Rev. Lett. **118**, 133401 (2017).
[15] T. Vogt, M. Viteau, A. Chotia, J. Zhao, D. Comparat, and P. Pillet, Phys. Rev. Lett. **99**, 073002 (2007).
[16] N. Thaicharoen, L. F. Gonçalves, and G. Raithel, Phys. Rev. Lett. **116**, 213002 (2016).
[17] L. F. Gonçalves and L. G. Marcassa, Phys. Rev. A **94**, 043424 (2016).
[18] R. Heidemann, U. Raitzsch, V. Bendkowsky, B. Butscher, R. Löw, L. Santos, and T. Pfau, Phys. Rev. Lett. **99**, 163601 (2007).
[19] E. Urban, T. A. Johnson, T. Henage, L. Isenhower, D. D. Yavuz, T. G. Walker, and M. Saffman, Nat. Phys. **5**, 110 (2009).
[20] A. Gaëtan, Y. Miroshnychenko, T. Wilk, A. Chotia, M. Viteau, D. Comparat, P. Pillet, A. Browaeys, and P. Grangier, Nat. Phys. **5**, 115 (2008).
[21] L. Isenhower, E. Urban, X. L. Zhang, A. T. Gill, T. Henage, T. A. Johnson, T. G. Walker, and M. Saffman, Phys. Rev. Lett. **104**, 010503 (2010).
[22] T. Wilk, A. Gaëtan, C. Evellin, J. Wolters, Y. Miroshnychenko, P. Grangier, and A. Browaeys, Phys. Rev. Lett. **104**, 010502 (2010).
[23] K. M. Maller, M. T. Lichtman, T. Xia, Y. Sun, M. J. Piotrowicz, A. W. Carr, L. Isenhower, and M. Saffman, Phys. Rev. A **92**, 022336 (2015).
[24] H. Labuhn, D. Barredo, S. Ravets, S. de Léséleuc, T. Macrì, T. Lahaye, and A. Browaeys, Nature **534**, 667 (2016).
[25] C. S. E. van Ditzhuijzen, A. F. Koenderink, J. V. Hernández, F. Robicheaux, L. D. Noordam, and H. B. van Linden van den Heuvell, Phys. Rev. Lett. **100**, 243201 (2008).
[26] T. J. Carroll, K. Claringbould, A. Goodsell, M. J. Lim, and M. W. Noel, Phys. Rev. Lett. **93**, 153001 (2004).
[27] P. Schauß, M. Cheneau, M. Endres, T. Fukuhara, S. Hild, A. Omran, T. Pohl, C. Gross, S. Kuhr, and I. Bloch, Nature **491**, 87 (2012).
[28] P. Schauss, J. Zeiher, T. Fukuhara, S. Hild, M. Cheneau, T. Macri, T. Pohl, I. Bloch, and C. Gross, Science **347**, 1455 (2015).
[29] G. Günter, M. Robert-de-Saint-Vincent, H. Schempp, C. S. Hofmann, S. Whitlock, and M. Weidemüller, Phys. Rev. Lett. **108**, 013002 (2012).
[30] G. Gunter, H. Schempp, M. Robert-de Saint-Vincent, V. Gavryusev, S. Helmrich, C. S. Hofmann, S. Whitlock, and M. Weidemuller, Science **342**, 954 (2013).
[31] A. Schwarzkopf, R. E. Sapiro, and G. Raithel, Phys. Rev. Lett. **107**, 103001 (2011).
[32] A. Schwarzkopf, D. A. Anderson, N. Thaicharoen, and G. Raithel, Phys. Rev. A **88**, 061406 (2013).
[33] N. Thaicharoen, A. Schwarzkopf, and G. Raithel, Phys. Rev. A **92**, 040701 (2015).
[34] D. P. Fahey, T. J. Carroll, and M. W. Noel, Phys. Rev. A **91**, 062702 (2015).
[35] M. Stecker, H. Schefzyk, J. Fortágh, and A. Günther, New J. Phys. **19**, 043020 (2017).
[36] J. Grimmel, M. Mack, F. Karlewski, F. Jessen, M. Reinschmidt, N. Sandor, and J. Fortagh, New J. Phys. **17**, 53005 (2015).
[37] J. Grimmel, M. Stecker, M. Kaiser, F. Karlewski, L. Torralbo-Campo, A. Günther, and J. Fortágh, Phys. Rev. A **96**, 013427 (2017).
[38] R. Feynman, J. Hollingsworth, M. Vennettilli, T. Budner, R. Zmiewski, D. P. Fahey, T. J. Carroll, and M. W. Noel, Phys. Rev. A **92**, 043412 (2015).
[39] R. Kosloff and D. Kosloff, J. Comput. Phys. **63**, 363 (1986).
[40] U. V. Riss and H. D. Meyer, J. Phys. B **26**, 4503 (1993).
[41] S. Sahoo and Y. K. Ho, J. Phys. B **33**, 2195 (2000).
[42] T. F. Gallagher, *Rydberg atoms* (Cambridge University Press, 1994).
[43] I. I. Beterov, I. I. Ryabtsev, D. B. Tretyakov, and V. M. Entin, Phys. Rev. A **79**, 052504 (2009).
[44] J. M. McGuirk, D. M. Harber, J. M. Obrecht, and E. A. Cornell, Phys. Rev. A **69**, 062905 (2004).
[45] J. M. Obrecht, R. J. Wild, and E. A. Cornell, Phys. Rev. A **75**, 062903 (2007).
[46] A. Tauschinsky, R. M. T. Thijssen, S. Whitlock, H. B. van Linden van den Heuvell, and R. J. C. Spreeuw, Phys. Rev. A **81**, 063411 (2010).
[47] H. Hattermann, M. Mack, F. Karlewski, F. Jessen, D. Cano, and J. Fortágh, Phys. Rev. A **86**, 022511 (2012).
[48] S. Bernon, H. Hattermann, D. Bothner, M. Knufinke, P. Weiss, F. Jessen, D. Cano, M. Kemmler, R. Kleiner, D. Koelle, and J. Fortágh, Nat. Commun. **4**, 2380 (2013).
[49] H. Hattermann, D. Bothner, L. Y. Ley, B. Ferdinand, D. Wiedmaier, L. Sárkány, R. Kleiner, D. Koelle, and J. Fortágh, Nature Communications **8**, 2254 (2017).